

UNIVERSITÀ DI PISA

Scuola di Ingegneria



Corso di Laurea Magistrale in

INGEGNERIA CHIMICA

Dipartimento di Ingegneria Civile e Industriale (DICI)

Tesi di Laurea Magistrale

**“Modeling the behaviour of pressurized vessels exposed
to fires through Computational Fluid Dynamics”**

Relatore

Dott. Ing. Gabriele Landucci

Candidato

Andrea Rum

Controrelatore

Dott. Ing. Chiara Galletti

Anno Accademico 2014/2015

UNIVERSITÀ DI PISA

Scuola di Ingegneria



Corso di Laurea Magistrale in

INGEGNERIA CHIMICA

Dipartimento di Ingegneria Civile e Industriale (DICI)

Tesi di Laurea Magistrale

**“Modeling the behaviour of pressurized vessels exposed
to fires through Computational Fluid Dynamics”**

Autore:

Andrea Rum

Firma: _____

Relatore:

Dott. Ing. Gabriele Landucci

Firma: _____

Controrelatore:

Dott. Ing. Chiara Galletti

Firma: _____

Anno Accademico 2014/2015

To my family: Dad, Mum

Ale, Checca and Marta

ABSTRACT

Accidental events in the process industry can lead to the release of hazardous substances by inducing the catastrophic rupture of equipment, resulting in possible accident escalation. This type of event, in which a primary event is propagated to other units, is usually indicated as a “Domino Effect” and is typically associated to an amplification in the consequences. This type of accident may severely affect also tankers for the shipment by road or rail of hazardous substances leading to high levels of individual and social risk in highly populated areas.

In the case of fires affecting tankers containing flammable pressurized liquefied gases (e.g., propane, butane, propylene, etc.), the effects of this event may lead to BLEVE (“Boiling Liquid Expanding Vapor Explosion”) and the associated fireball, with extremely severe consequences. This chain of events has actually occurred several times over the years, both in chemical and process plants, but also in the framework of dangerous goods road and rail. For this reason, since the 1970, this accident scenario was investigated through large scale experiment and pilot tests, in order to test the response capabilities of the PRV (“Pressure Relief Valve”) and the effectiveness of the thermal protection such as fireproofing, installed on storage and transport equipment. In addition, starting from the same period, researchers began to develop numerical models, which are currently increasing in complexity and capabilities due to more advanced computational resources.

The aim of the present work is to demonstrate the capabilities of commercially available CFD (“Computational Fluid Dynamics”) codes for modeling thermo–fluid dynamics of tank containing pressurized liquefied gases. ANSYS® FLUENT® v.14.5 software was used to set up the simulations. The CFD code allows to carry out a complete analysis of the heat transfer and the fluid motion which is generated in the stored substance due to the buoyancy forces. The heating of the vessel, due to the external fire, induces a temperature increase in the fluid, that laps the walls internally: the liquid, having higher temperature and less density, due to the gravitational field, rise again up to reach the interface with the vapour. This is the cause that leads to the establishment of the “liquid thermal stratification” in the vessel. In addition to the stratification, it is important to evaluate and predict the dynamics evolution of the liquid–vapour interface in space and time, or rather, the computation of the swelling of the liquid phase during the thermal stratification process, in order to estimate correctly the PRV opening time. These issues were addressed in the ANSYS® FLUENT® v.14.5 software through specific multiphase modelling tools, such as the Volume of Fluid model (VOF).

In order to test the reliability of CFD predictions, the fluid dynamic model was validated by comparison with a large scale experimental test carried out in New Mexico (U.S.A.) in 1974.

Once the CFD model has been validated, the focus of this work has shifted to the analysis of the peculiar aspect of “liquid thermal stratification” that occurs during the fire exposure, since it plays an essential role during the heat up of the tank. This phenomenon has relevant effects on the increase of pressure inside the vessel and on the energy accumulated in the liquid phase: this energy will be released at the time of catastrophic failure.

The vertical temperature gradient affects the pressure build up in the vessel since the hotter liquid layer, that is placed at the liquid–vapour interface, determines the pressure reached from the tank: the above vapour is thermally overheated while the underlying liquid is subcooled. For this evaluation a sensitivity was carried out by varying the liquid filling level in the tank, the incident heat flux on the unprotected walls and geometrical parameters (thickness and diameter of the tank). The sensitivity analysis allowed extrapolating a correlation for assessing the thickness of thermally altered layer in function of the parameters mentioned above and by the pressure in the vessel. The evaluation of the thickness of this altered layer is important to improve the predictive capabilities of a lumped Model, so as not to neglect the stratification effects.

Finally, the work discussed the implementation of “advanced boundary conditions” for the incident heat flux, function of the time and space. In particular, it was analysed an accidental scenario that can occur in a storage park of an industrial site: a pool fire resulting from the loss of containment of an atmospheric tank affecting a pressurized vessel. The boundary conditions, obtained using a simplified fires model for the calculation of incident heat flux for each point of the wall, were subsequently implemented on the CFD code through the construction of a dedicated User Defined Function (UDF).

The results of this work demonstrated the capabilities of CFD models in supporting the analysis of complex accidental scenarios in order to supported advanced risk assessment studies.

SOMMARIO

Gli eventi accidentali nell'industria di processo possono portare al rilascio di sostanze pericolose inducendo la rottura catastrofica di apparecchiature, con conseguente possibile escalation di un incidente. Questo tipo di evento, in cui un evento primario è propagato ad altre unità, è generalmente conosciuto come "Effetto Domino" ed è tipicamente associato ad un'amplificazione nelle conseguenze. Questo tipo di incidente può colpire anche serbatoi per il trasporto su strada o ferrovia di sostanze pericolose portando ad alti livelli di rischio individuale e sociale nelle zone ad elevata densità di popolazione.

Nel caso di incendi che interessano serbatoi contenenti gas liquefatti in pressione (propane, butane, propylene, etc.), gli effetti di questo evento possono portare al BLEVE ("Boiling Liquid Expanding Vapor Explosion") e alla Fireball associata, con conseguenze estremamente gravi. Questa catena di eventi si è realmente verificata varie volte nel corso degli anni, sia in impianti chimici e di processo, sia nel trasporto ferroviario e stradale di tali sostanze. Per questo motivo, fin dagli anni '70 questo scenario incidentale è stato investigato attraverso test su larga scala e prove pilota, in modo da testare la capacità di risposta della PRV (Valvola di Rilascio della Pressione) e l'efficacia delle protezioni termiche associate all'apparecchiatura. Inoltre, nello stesso periodo, i ricercatori iniziarono a sviluppare i primi modelli numerici, che sono in continuo incremento in complessità e capacità a causa dell'aumento delle potenze computazionali.

L'obiettivo del presente lavoro è dimostrare la capacità dei codici CFD (Fluidodinamica Computazionale) disponibili in commercio per la modellazione termo-fluidodinamica di serbatoio contenenti gas liquefatto in pressione. Per effettuare le simulazioni è stato utilizzato il software commerciale Ansys®Fluent® v. 14.5. Il codice CFD permette di effettuare una completa analisi fluidodinamica dello scambio termico e del profilo di moto che è generato nel fluido stoccato a causa delle forze gravitazionali. Il riscaldamento del serbatoio, dovuto all'incendio esterno, induce un incremento di temperatura nel fluido che ne lambisce internamente le pareti: il liquido avente maggiore temperatura e minor denso, per effetto del campo gravitazionale, risale fino a raggiungere l'interfaccia con il vapore. Questa è la causa che porta all'istituzione della stratificazione termica del liquido stoccato nel serbatoio. Oltre alla stratificazione, è importante valutare e predire l'evoluzione dinamica dell'interfaccia liquido-vapore nello spazio e nel tempo, o meglio, la computazione della dilatazione della fase liquida durante il processo di stratificazione termica, al fine di stimare correttamente il tempo di apertura della PRV. Il software Ansys®Fluent® v. 14.5

dispone di un modello multifase specifico per il monitoraggio in stato stazionario e transitorio, di qualsiasi interfaccia gas-liquido: il Volume of Fluid Model (VOF).

Per dimostrare la veridicità del codice CFD, il modello fluidodinamico è stato validato attraverso il confronto con un test sperimentale su larga scala effettuato nel 1974 in New Mexico (U.S.A.).

Una volta che il modello CFD è stato validato, il focus del presente lavoro si è spostato sugli aspetti peculiari della “stratificazione termica” della fase liquida durante l’esposizione al fuoco, in quanto questa riveste un ruolo essenziale nella risposta del serbatoio. Questo fenomeno ha effetti sull’aumento di pressione all’interno del serbatoio e sull’energia immagazzinata dalla fase liquida: questa energia sarà poi rilasciata al momento della rottura catastrofica.

Il gradiente di temperatura verticale regola la pressione nel vessel poichè lo strato di liquido più caldo, che si colloca presso l’interfaccia liquido-vapore, determina la pressione raggiunta dal serbatoio: il vapore sovrastante è termicamente surriscaldato mentre il liquido sottostante è sottoraffreddato. Per questa valutazione è stato necessario effettuare un’analisi di sensitività andando a variare il livello di riempimento di liquido nel serbatoio, il flusso termico incidente sulle pareti non protette e i parametri geometrici (spessore e diametro del serbatoio). L’analisi di sensitività ha permesso di estrapolare una correlazione per la valutazione dello spessore della strato termicamente alterato in funzione dei parametri precedentemente citati e della pressione nel serbatoio. La valutazione di questo strato è importante per migliorare le capacità predittive di un modello a parametri concentrati, in modo da non trascurare l’effetto della stratificazione.

L’ultima parte del lavoro mira all’implementazione di “advanced boundary conditions” per il flusso termico incidente sulle pareti del serbatoio, variabili nel tempo e nello spazio. In particolare, è stato analizzato uno scenario incidentale che può verificarsi in un parco stoccaggi di un sito industriale: un pool fire derivante dalla perdita di contenimento di un serbatoio atmosferico può propagarsi e recare danni ai serbatoi pressurizzati presenti nelle vicinanze. Le condizioni al contorno, ottenute usando modelli semplificati di incendio per il calcolo del flusso termico incidente in ogni punto della parete, sono stati successivamente implementate sul codice CFD attraverso la costruzione di una dedicata User Defined Function (UDF).

I risultati di questo lavoro hanno dimostrato le capacità dei modelli CFD nel sostenere l’analisi di complessi scenari incidentali per studi di valutazione del rischio con strumenti avanzati.

Table of Contents

List of Figures	4
List of Tables.....	8
1. Introduction.....	10
2. Safety in the transportation of Pressurized Liquefied Gas	13
2.1. Safety issues in Hazardous Materials Transportation	13
2.2. Critical accidental scenarios in LPG transportation.....	15
2.2.1. BLEVE analysis and relevant case hystories	16
2.2.2. Mechanism of BLEVE.....	19
2.2.3. Fireball associated to BLEVE.....	24
3. Theoretical analysis of transport and storage vessels exposed to fire.....	27
3.1. Dynamics of the Wall Temperature of tank involved in fire.....	28
3.2. Dynamics behaviour of the Stored Fluid Temperature in the vessel involved in fire	33
3.3. The effect of liquid thermal stratification phenomenon.....	35
4. Experimental and numerical studies of pressurized vessel exposed to fire: state of the art.....	41
4.1. Experimental studies	41
4.1.1. Introduction.....	41
4.1.2. Description and results of the Townsend test.....	43
4.2. Numerical studies.....	48
4.2.1. Lumped Parameters Modeling Approaches	48
4.2.2. Simplified Correlations for Vessel Failure Prediction	54

4.2.3. Distributed Parameters Modeling Approaches.....	54
5. Aims of the work.....	56
6. Description of the CFD model	58
6.1. Theoretical aspects of the CFD model	58
6.1.1. CFD Modeling Overview.....	58
6.1.2. CFD implementation of the relevant physical phenomena	60
6.2. Numerical implementation of the CFD Model.....	78
6.3. Development of advanced computational mesh.....	84
7. CFD model validation	86
7.1. Simulation set up for the validation case.....	86
7.2. Validation results	87
7.2.1. Lading Temperature Distribution.....	88
7.2.2. Tank Pressure vs Time	91
7.2.3. PRV Opening Time	92
7.2.4. Tank Filling Level vs time	92
7.3. Mesh independence.....	93
8. Model application and definition of case studies	100
8.1. Sensitivity analysis.....	100
8.2. Case studies for advanced accidents simulation.....	103
8.2.1. Characterization of the industrial scenario.....	103
8.2.2. Fire calculations for evaporating confined pools	105

8.2.3. Heat flux at a distance from the fire: atmospheric transmissivity and view factor	108
8.2.4 Pool fire results and “Advanced Boundary Condition”	112
8.2.5. CFD model simulations to reproduce the industrial accident	115
9. Results and discussion.....	117
9.1. Sensitivity analysis and simplified stratification model.....	117
9.1.1. CFD simulation results.....	117
9.1.3. Parametric correlation	125
9.2. Results and discussion of industrial accidents simulation.....	129
9.2.1 Results	129
9.2.2 Discussion	131
10. Conclusions and further developments	134
Reference.....	136
Appendix	142
Appendix 1: Subroutine for Evaporation -Condensation Phenomena	142
Appendix 2: subroutine for Boundary Conditions in the Validation Case.....	144
Appendix 3: subroutine for “Advanced Boundary Conditions”.....	145
List of symbols.....	147
List of Greek Symbols	149
List of acronyms.....	150
List of subscript and superscript.....	151
Acknowledgements	152

List of Figures

Figure 2.1: General Procedure for QRA [4].....	14
Figure 2.2: The incident at Mexico City, 1984 [1].....	17
Figure 2.3: An illustrative list of some of the major BLEVEs from 1926 to 2004 [9].	19
Figure 2.4: Accidental chain during the lifecycle of a storage tank [10].	20
Figure 2.5: Liquid-Vapour equilibrium under depressurization at a constant temperature [15]. ...	21
Figure 2.6: RK–EOS form [16].....	22
Figure 2.7: Liquid spinodal curve and tangent line to the saturation curva at critical point [15].....	23
Figure 2.8: Development of the typical fireball from a source at ground level [4].....	25
Figure 2.9: Shape of fireball as a function of time:0) ignition, 1) growth, 2) steady brning and lift off, 3) burnout [4].....	26
Figure 3.1: Trend as a function of time of equivalent and admissible stress [2].....	29
Figure 3.2: Stress and Strain Curve for Steel [20].	29
Figure 3.3: The sequence events required for the BLEVE outcome [26].	32
Figure 3.4: Physical model for thermohydraulic behaviour [42]	34
Figure 3.5: Physical phenomena involved in vessel heat–up [42].	35
Figure 3.6: Trend of the liquid temperature (K) for two successive time, respectively 150s and 450s (adopted by source [42]).	36
Figure 4.1: Summary of Relevant Literature Experiments on Unprotected Pressurized Vessels exposed to fire [6].	42
Figure 4.2: Summary of Relevant Literature Experiments un Pressurized Vessels exposed to fire in presence of Thermal Protection [6].	43

Figure 4.3: DOT 112A340W tank car: a) real image b) sketch to show the geometrical features and the positioning of instrumentation used during the test [22]..... 44

Figure 4.4: Cross-Sectional View of Thermocouple Position and their respective Item: a) Front Cross-Section; b) Rear Cross-Section [22]. 45

Figure 4.5: Liquid Level vs time in the Townsend’ report [22]. 45

Figure 4.5: Liquid Level vs time in the Townsend’ report [22]. 47

Figure 4.6: Pressure vs time in the Townsend’ report [22]. 47

Figure 4.7: Incident flux heat on the wall of tank vs time in the Townsend’ report [22]..... 48

Figure 4.8: Schematization of thermal nodes for lumped parameters analysis of pressurized vessels [60]. 50

Figure 4.9: Schematization of the simplified stratification model proposed by Birk, adapted from [60–61]. 51

Figure 4.10: Schematization of the stratification model proposed by Yu et al., adapted from [30], [60]. 52

Figure 4.11: Schematization of the stratification model proposed by Bazzocchi et al., adapted from [60]. 53

Figure 5.1: Flow chart describing the methodology used in the present work..... 57

Figure 6.1: Integral form of conservation law for a general property ϕ (adapted from Ref [43]).... 60

Figure 6.2: Graphic explanation of the main transport phenomena involved (adapted by [44])..... 61

Figure 6.3: Subdivision of the near wall region [44]. 72

Figure 6.4: Geometrical domain a) real system b) simulated system..... 79

Figure 6.5: Items of Solution Setup in ANSYS® FLUENT® software [56]. 80

Figure 6.6: Items of Solution in CFD software [56]. 82

Figure 6.7: SIMPLE algorithm [58]. 83

Figure 7.1: Experimental vs CFD Model temperature for the Rear cross-section at two different time values.	89
Figure 7.2: Experimental vs CFD Model temperature for the Front cross-section at two different time values.	90
Figure 7.3: Experimental vs CFD Model pressure in function of the time.	91
Figure 7.4: Experimental vs CFD Model filling level in function of the time.	93
Figure 7.5: Coarse vs Fine Mesh temperature for the Rear cross-section at two different time values.....	95
Figure 7.6: Coarse vs Fine Mesh temperature for the Front cross-section at two different time values.....	96
Figure 7.7: Experimental vs CFD Model (for Coarse and Fine mesh) pressure in function of the time.....	97
Figure 7.8: Experimental vs CFD Model (for Coarse and Fine mesh) filling level in function of the time.....	98
Figure 8.1: Calculation mesh adoptd in the case studies for sensitivity analysis and detail of a portion of the domain representing boundary layer and liquid–vapour interface.	101
Figure 8.2: Storage park in a industrial site (adopted by source [67]).	104
Figure 8.3: Step procedure for SEP evaluation [4].	106
Figure 8.4: Schematization of a tilted pool fire (adopted from [4]).	107
Figure 8.5:Schematization for view factor calculation (adopted from [4]).....	110
Figure 8.6: Sketch illustrating the relative positions of the fire, tank and the radiation receiving element on the tank surface and the various angles.	110
Figure 8.7: Radiation intensity for pool fire obtained through DNV® Phast® 6.4 software.....	114
Figure 8.8: Schematization of flux heat incident on the wall of the tank.....	115

Figure 9.1: Results for case study “16”: temperature profile (K) at 30 s (a) and 120 s (c); axial velocity profile (m/s) at 30 s (b) and 120 s (d). PRV opening time is 131.7 s. 118

Figure 9.2: Results for case study “10”: temperature profile (K) at 60 s (a) and 180 s (c); axial velocity profile (m/s) at 60 s (b) and 180 s (d). PRV opening time is 184.5 s. 119

Figure 9.3: Results for case study “17”: temperature profile (K) at 15 s (a) and 45 s (c); axial velocity profile (m/s) at 15 s (b) and 45 s (d). PRV opening time is 51.5 s. 121

Figure 9.4: Results for case study “7”: temperature profile (K) at 20 s (a) and 80 s (c); axial velocity profile (m/s) at 20 s (b) and 80 s (d). PRV opening time is 90.0 s. 122

Figure 9.5: Average liquid temperature ($T_{L,av}$), pressure (P) and dynamic stratification index (Π) for: (a) reference case; (b) case–study “10”; (c) case–study “17”; (d) case–study “7” 124

Figure 9.6: Trend of the parameter $h1/D$ as a function of Filling Level. 127

Figure 9.7: Trend of the parameter $h1/D$ as a function of the Flux Heat. 127

Figure 9.8: Comparison between the values of $h1/D$ predicted by the CFD Model and calculated with the parametric correlation. 128

Figure 9.9: Results for case–study “a”: temperature profile (K) at 20 s (a), 100 s (c) and 200 s (e); axial velocity profile (m/s) at 20 s (b), 100 s (d) and 200 s (f). PRV opening time is 229.5 s. 129

Figure 9.10: Results for case–study “b”: temperature profile (K) at 30 s (a), 150 s (c) and 300 s (e); axial velocity profile (m/s) at 30 s (b), 150 s (d) and 300 s (f). PRV opening time is 336.5 s. 130

Figure 9.11: Pressure profile and liquid Temperature profile (1. near to bottom vessel, 2. in the liquid bulk, 3. near to liquid–vapour interface) for: a) case–study “a”; b) case–study “b” 132

Figure 9.12: Comparison between the liquid thermal expansion predicted in case–studies, in terms of liquid level displacement (m). 133

List of Tables

Table 2.1: Critical constant for propane pure [25].	24
Table 2.2: SLT value prediction for propane pure with several criterion	24
Table 3.1: Frequency of BLEVEs initiating events[9].....	27
Table 3.2: Typical parameters for the main Fires [24].....	31
Table 4.1: Features of DOT 112A340W tank-car.	44
Table 4.2: Temperature Experimental Data used for the CFD Model Validation [22].....	46
Table 4.3: Lumped Parameter Models for the prediction of the behavior of pressure vessels exposed to fire.	49
Table 4.4: Description for each nodes of thermal nodes schematization [6].	50
Table 6.1: Constant Values for K-ε Model [53].....	71
Table 6.2: Correlations Adopted for the evaluation of Propane Physical Properties (Interpolation of data reported by [22] and [55]).	77
Table 6.3: Properties of pure propane necessary to solve the PR-EOS [55].	78
Table 6.4: Summary of the Models, Materials and Phases in the present study.	81
Table 6.5: Summary of the Solution Methods used in the present work.	83
Table 6.6: Main features of the mesh used for industrial accidents simulation.	85
Table 7.1: Time discretization of incident flux heat on the wall of the tank.....	87
Table 7.2: Initial conditions set for validation of the CFD Model.	87
Table 7.3: Experimental vs CFD Model Pressure for some time values.....	91
Table 7.4: Experimental vs CFD Model PRV opening time.....	92
Table 7.5: Experimental vs CFD Model filling level for some time values.....	93

Table 7.6: Coarse vs fine mesh features.....	94
Table 7.7: Coarse vs Fine Mesh Pressure for some time values.	96
Table 7.8: Coarse vs Fine Mesh Filling Level for some time values.	98
Table 7.9: Coarse vs Fine Mesh Pressure for some time values.	98
Table 8.1: Main features of the several meshes used for the sensitivity analysis.	101
Table 8.2: Summary of case studies implemented in CFD Model for the sensitivity analysis.	102
Table 8.3: general features of the atmospheric vessel.	104
Table 8.4: Physical properties of stored fluid in the atmospheric vessel.	105
Table 8.5: Geometric features of pressurized vessel [68].	105
Table 8.6: Pool fire results obtained with simplified correlations and DNV® Phast® 6.4.	113
Table 8.7: Effects of primary pool fire on the target equipment.	114
Table 9.1: Summary of the case studies results for the liquid stratification analysis.	126
Table 9.2: Coefficient values obtained through the linear regression.	128

1. Introduction

Transportation of flammable pressurized liquefied substances (such as LPG, propylene, butadiene, etc..) has a strategic importance for the economy of industrialized countries: these products are typically transported as pressurized liquified gases at ambient temperature by rail and/or road tank-cars [42].

The occurrence of critical incidents related to LPG transportation has made public this problem, raising social concern on the safety of such activities. In recent years, two serious accidents occurred respectively in Italy and Canada: the first accident affected the densely high populated area of Viareggio: the 29th of June, 2009, a freight train carrying 14 tank-cars containing LPG derailed. A tank-car overturned and released its entire inventory (about 46 ton of LPG). LPG vapourized very quickly and formed a cloud that spread over the railway area and that extended over a residential zone near to the railway. The delayed cloud ignition, caused extended damages and 31 fatalities. This event is the more recent and the more severe of a chain of accidents caused by transportation of hazardous material in highly populated areas [2]. The second one occurred the 6th of July, 2013: a train of 74 rail tank-cars carrying “crude oil” derailed in Lac-Megantic, Canada. Approximately 5,7 million liters of the substance were released into the soil, water and air after the incident. It took two days to extinguish the consequent fire.

One of the critical accidents that may occur during LPG transportation is the BLEVE (“Boiling Liquid Expanding Vapour Explosion”). This consist in a catastrophic failure of vessel containing LPG: this substance, due of the sudden depressurization from storage pressure to atmospheric pressure, vaporizes and expands instantly. The main dangerous consequences related to BLEVE are:

- Blast wave originating by violent fluid depressurization;
- Projection of fragments resulting by the collapse of the equipment;
- Fireball due of easy LPG ignitions: energy generated by fireball is released as radiative flux.

BLEVE is typically induced when rail and/or road tank-cars are exposed to prolonged external fires, which may occur as a result of other transportation accidents [7]. The heat load associated to external fire causes a marked change of the physical conditions for the stored fluid, due to increase

of internal pressure and liquid temperature, resulting in establishment of the thermal stratification phenomenon [13]. Furthermore, the increase of walls temperature reduces the mechanical strength of steel, with possible tear of the equipment and consequent loss of containment.

BLEVE and its prevention have been subjects of research for more than 40 years [7], [11], [12], [14],[18],[19],[26]. To better understand the mechanism that leads to BLEVE were carried out various experimental tests, reported in literature, to investigate on this dangerous scenario. The most important large-scale experiment was carried out by Townsend et al. in 1974 in New Mexico: the aim of this test was also analyzed the ability of passive protection (insulating layer) avoiding the explosion [22].

Since large scale testing is hazardous as well extremely expensive, numerical model and specific calculation codes (ENGULF [36],[37], TANKCAR [23], TAC7 [38] among the more relevant) were developed starting from the 70s in order to simulate this final scenario.

In recent years, due to the lower cost of computational performance, it has increased the interest of using distributed parameters codes (CFD and FEM), to study the effect of fire exposure on LPG tanks [42]. However, the detailed assessment of the behavior of stored fluid in tank during the exposure with advanced tools, to investigate the liquid thermal stratification and liquid thermal expansion, is still lacking.

In the present work, a CFD Model was developed with the aim to simulate the horizontal tank-cars behaviour during the fire exposure. CFD code solves the governing equations in a domain consisting of two continuous phases. Both to improve the predictions of models present in FLUENT® and to provide specific boundary conditions, several UDF (“User Defined Functions”) were implemented.

The simulations were aimed at the evaluation of the increase pressure and temperature of fluid, tracing in detail a peculiar and critical phenomenon, such as the liquid thermal stratification. The presence of stratified temperature in liquid domain was extensively investigated by Birk [13] and Venart [19]. The ability of the CFD model to account thermal stratification leads to overcome the restriction of the simplified numerical modelling approaches, such as thermal nodes lumped parameters models, that neglect the thermal stratification of the liquid phase [33] or that do not adopt a rigorous models [30], [60], [61].

Experimental results available on large scale were adopted in order to provide CFD model validation. Then, the model was applied in order to perform a sensitivity analysis and the assessment of an industrial case study.

The sensitivity analysis was aimed at evaluating the thickness of the thermally modified layer associated to the stratification. Liquid filling level in the tank, incident heat flux on the unprotected walls, geometrical parameters (thickness and diameter of the tank) were modified in order to obtain a simplified parametric correlation to estimate the extension of the thermally stratified zone in the vessel. This activity was developed with the final aim to support simplified lumped parameter codes [33], in which stratification is not systematically addressed.

Finally the CFD model was applied in order to simulate an industrial case study in order to test the potentialities of the method in the framework of advanced risk assessment studies.

2. Safety in the transportation of Pressurized Liquefied Gas

2.1. Safety issues in Hazardous Materials Transportation

The transportation of “chemicals” is necessary for the manufacturing and distribution of products within and across regional and international borders. Many of these shipments are regulated for transportation and are typically referred to as “dangerous goods” or “hazardous materials”. Particularly in industrialized countries, these daily shipments are critical to economies across the globe, but these activities may also pose a potential risk to public safety and the environment if an accidental release were to occur during transportation. Several studies [63–65] have shown that the risks arising from this transportation have the same quantitative importance of that one due to fixed installations, hence those risks need for a dedicated quantitative assessment.

Before introducing the “Quantitative Risk Assessment” concept, it is useful to introduce Hazard and Risk. “Hazard” can be defined as a physical condition that has the potential to cause damage to people, property or environment. This definition includes damage to people in the short time, caused by a fire or an explosion, and damage that have a long term effect on a person’s health, due to the release of toxic substance [3]. “Risk” can be defined as a combination (typically the product) of the frequency of the event and its magnitude, since in its evaluation are taken into consideration both the aspects related to the probability of occurrence of an accident and aspects related to its severity.

From 40 years, the safety aspects in the process industry and transportation of hazardous materials have become more relevant over time. Following the serious incidents that took place in the chemical industry in early 70s (in particular the explosion of Flixborough, 1974, in England that caused 28 dead and many injured and the Seveso disaster, 1976, Italia), the European legislative framework was a first developed for the design, installation and management of highly dangerous plants. On 24 of June, 1982, the Council of European union issued a Directive on “risks of major accident of certain industrial activities”, known as “Seveso Directive (82/501/EEC)”. The purpose of the Directive, which takes into account the concept of “Probability Risk Assessment”, is to limit the possibility of accidents occurring to a significant severity.

QRA (Quantitative Risk Assessment) is a valuable tool for determining the risk of the use, handling, transport and storage of dangerous substances. These quantitative risk assessment are

carried out if significant quantities of hazardous materials are present or in industrial site or even in transportation routes.

A QRA is used in a “Safety report” to demonstrate the risk related to the establishment and to provide the competent authorities with all the information needed to make a decision on the acceptability of such risk and to prepare emergency plan [3].

To make a QRA it is basically necessary to answer to three questions:

- What can go wrong?
- What is the probability that it will go wrong?
- What are the consequences?

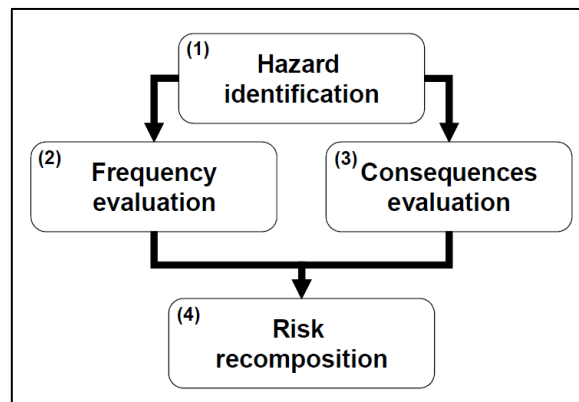


Figure 2.1: General Procedure for QRA [4].

To answer the first question a hazard identification study has to be performed, in which unwanted events and their mechanisms are identified [4]. The reliability theory, based on statistical analysis, is used to estimate the probability and frequency of occurrence of dangerous Scenarios. To assess the consequences, depending on the type of scenario, there are several methods available: these models provide information about flux heat (fire), concentration of toxic substance (dispersion) and peak overpressure (explosion). This information may be used to assess the effects on the target (usually a person or the environment), in order to estimate the percentage of death (or other damage) [5].

Accidental releases of flammable and/or toxic substances may also be associated to the rupture of road tankers or tank wagons, triggering accidents with multiple fatalities [6].

The development and evaluation of preventive and protective measures for risk reduction in the transportation of dangerous goods is a key issue, confirmed by the results of some QRA studies

where hazardous materials are present. These studies pointed out that the transport activities of such substances give a significant contribution to the overall risk and therefore it is necessary to reduce this risk. For flammable substances, the most hazardous condition of transportation is the state of pressurized liquified gas. In case of subcooled liquids or high pressurized gas the consequences are not as much severe [6].

In the present work, we focused on a particular class of substances, e.g. flammable pressurized liquified gases such as LPG (liquefied Petroleum Gas), propylene, butadiene etc., whose transportation in Europe is very intense. LPG is a mixture of saturated hydrocarbons, mainly propane and butane, which are gaseous under atmospheric conditions: consequently, this substance is transported as pressurized liquefied gas. Due to this peculiarity, an accident may lead to serious consequence also on off road population.

Past accident data analysis [62] shows that about 33% of accident occurred during the LPG transportation induced by exposure to fire led to BLEVE and associated Fireball: for this reason, the BLEVE's scenario, is often associated to the typical accidents involving road and/or rail tank-cars. In this section, the main aspects related to these final outcomes will be analysed.

2.2. Critical accidental scenarios in LPG transportation

According to the conditions of fluid, in case of catastrophic release (caused by BLEVE) a certain amount of liquid and vapour can be formed. Depending on the liquid–vapour ratio, the first one can go to form a boiling pool to the ground (rain–out) or, as in most cases, it can be almost completely entrained by vapour, forming a very dense cloud of aerosols [9],[13]. Since the external fire is the main primary event leading to BLEVE, if this happens, there is no way to avoid the triggering of such cloud resulting in a fireball. In a statistical analysis prepared by Paltrinieri et al. [7], on 44 incidents involving the LPG transportation in which BLEVE occurred, 38 had fire as initiating event for escalation (Hot–BLEVE). Only in 6 cases the BLEVE occurred for an impact on the tank which resulted in a first release of the substance and a subsequent catastrophic failure: it was caused by the depressurization and following uncontrolled evaporation of the substance inside the tank (Cold–BLEVE).

Hot-BLEVE can be avoided or at least delayed through the use of thermal insulation to protect the transport and storage vessels (passive fire protection) [7]. A device ever present on tank to avoid BLEVE is the Relief Valve (PRV): if it is designed following the reference standards (standard API 520 and 527) it should be able to vent the overpressure before the catastrophic rupture of tank.

In the literature, several studies and experiments documented the behaviour of LPG tanks exposed to external fire [6]. Usually, the tested equipment are pressurized horizontal cylindrical vessels, equipped with of PRV and insulating layer, so as to evaluate the ability of such protections. Furthermore, the tank is engulfed in a diesel pool fire or a Jet–Fuel Jet fire.

Since these tests, it was possible to obtain information on some key parameters [6] like:

1. Wall temperature distribution vs time
2. Lading temperature distribution vs time
3. Tank fill level vs time
4. Tank pressure vs time
5. PRV behaviour (if one is present)
6. Time to failure (tff) and condition at failure, or time to empty (tte)
7. Modes of failure
8. Hazard due to blast, projectiles and resulting fire or explosion.

These data are critical to support the theoretical analysis and modeling of tanks behaviour. For this reason, some on these parameters will be analyzed in more detail in this Section.

2.2.1. BLEVE analysis and relevant case histories

The acronym BLEVE was coined in 1957 by three Factory Mutual Research Corporation workers J.B. Smith, W.S. Marsh and W.L. Walls [8], who analyzed the likely way of failure tanks containing an overheated mixture of formalin and phenol, and had believed that the vessel had suffered a “Boiling Liquid Expanding Vapour Explosion” [X]. Afterwards, the Center for Chemical Process Safety (CCPS) [8] has defined BLEVE as “a sudden release of a large mass of pressurized superheated liquid to the atmosphere”. The sudden release can occur due to containment failure caused by fire engulfment, a missile hit, corrosion, manufacturing defects, internal overheating, etc [9]. In most of the cases that have occurred, BLEVE have had a external fire as primary event: for this reason, the recent studies to prevent and/or to delay the escalation have focused on the development of passive fire protection for tanks.

BLEVE is one of the most dangerous scenarios that can occur in the process industry and during the transport of hazardous substances. The main consequences related to this scenario are:

- Splashing of some of the liquid to form short–lived pools; the pools would be on fire if the liquid is flammable.

- Blast wave.
- Flying fragments (missiles).
- Fire or toxic gas release. If the pressurized liquefied gas is flammable, as is often the case, the BLEVE leads to a fireball. When the material undergoing to BLEVE is toxic, as in the case of ammonia or chloride, adverse impacts include toxic gas dispersion.

BLEVE needs to be prevented because, once occurred, the probability of propagation on other units or on population and environment is high, if accidents respectively occurred in an industrial site or during the transport of pressurized liquefied gas.

A lesson learnt about BLEVE triggering other BLEVEs is the accident of San Juan Ixhuatepec, Mexico City, 1984, that involved the PEMEX LPG terminal during which 13 BLEVEs followed one another. On 19th of November, a 2m high cloud of LPG covering an area of about 30000 m², spread over the City. After the initial release, caused by a leak in a pipeline, the first BLEVE occurred. For the next 90 minutes, there followed a series of 12 BLEVEs, which led to the destruction of the entire PEMEX LPG terminal. The violent explosion was recorded by seismographs at the University of Mexico. The damage due to the explosions and the resulting fire were estimated at about \$31 million, 650 deaths and about 6400 injuries [1].

Figure 2.2 shows an image taken as soon as after the accident. The following table (fig. 2.3) shows a list of the most significant BLEVEs that occurred between 1926 and 2004 [9]. From the table it is possible to see the locations of the accidents, the substance involved in the accidents and their quantities, the causes of the BLEVE and the number of fatalities and injuries.



Figure 2.2: The incident at Mexico City, 1984 [1].

Date	Location	Cause	Material	Quantity (tonnes)	Death (d), injured (i)
13 December 1926	St. Auban, France	Overfilling	Chlorine	25	19d
28 May 1928	Hamburg, Germany	Runaway	Phosgene	10	11d, 17i
10 May 1929	Syracuse, NY, USA	Explosion (H ₂)	Chlorine	25	1d
24 December 1939	Zamesti, Romania	Overfilling	Chlorine	10	60d
29 July 1943	Ludwigshafen, Germany	Overfilling	Butadiene	16	57d
5 November 1947	Rauma, Finland	Overfilling	Chlorine	30	19d
28 July 1948	Ludwigshafen, Germany	Overfilling	Ethyl ether	33	209d
7 July 1951	Port Newark, NJ, USA	Fire	Propane (70)	2600	14i
4 April 1952	Walsum, W. Germany	Overfilling	Chlorine	15	7d
4 June 1954	Institute, WV, USA	Runaway	Acrolein	20	–
1955	Ludwigshafen, FRG	Railroad accident	LPG	^	2i
1955	Cottage Grove, OR, USA	Storage vessel failure	LPG	^	12d, 13i
8 January 1957	Montreal, Canada	Fire	Butane	5100	1d
1958	Michigan, USA	Overfilling	Butane	55	1d
28 June 1959	Meldrin, GA, USA	Damage (Derail)	Propane	55	23d
18 August 1959	Kansas City, MO, USA	Fire	Gasoline	70	5d
1959	McKittrick, CA, USA	LPG	Storage cylinder (six on site)	^	2i
17 April 1962	Doe Run, KY, USA	Runaway	Ethylene oxide	25	1d
4 January 1966	Feyzin, France	Fire	Propane	1000	18d, 83i
1 January 1968	Dunreith, IN, USA	Fire (Derail)	Ethylene oxide	NA	5i
21 August 1968	Lieven, France	Mechanical	Ammonia	20	5d
2 January 1969	Repcelak, Hungary	Overfilling	Carbon dioxide	35	9d
25 January 1969	Laurel, MS, USA	Fire (Derail)	Propane	65	2d, 976i
18 February 1969	Crete, NB, USA	Damage (Derail)	Ammonia	65	8d
1969	Cumming, IA, USA	Damage (Derail)	Ammonia	^	^
11 September 1969	Glendora, MS, USA	Fire	Vinyl chloride	55	–
21 June 1970	Crescent City, IL, USA	Fire (Derail)	Propane (5)	275	66i
19 January 1971	Baton Rouge, LA, USA	Overpressure	Ethylene	4	–
19 October 1971	Houston, TX, USA	Fire (Derail)	Vinyl chloride	50	1d, 50i
9 February 1972	Tewksbury, MA, USA	Collision	Propane	28	NA
30 March 1972	Rio de Janeiro, Brazil	Fire	Propane	1000	37d
21 September 1972	NJ Turnpike, NJ, USA	Collision	Propylene	18	2d
27 November 1972	San Antonio, TX, USA	Corrosion	Carbon dioxide	0.01	–
1972	Lynchburg, VA, USA	Propane	Road tanker	9	2d, 5i
1972	Rio de Janeiro, Brazil	LPG	Storage spheres (five on site) and cylinders	^	37d, 53i
5 July 1973	Kingman, AZ, USA	Fire	Propane	100	13d, 95i
11 January 1974	W. St. Paul, MN, USA	Fire	Propane	27	4d
12 February 1974	Oneonta, NY, USA	Fire (Derail)	Propane (4)	288	25i
29 July 1974	Pueblo, CO, USA	Fire (test)	Propane	80	–
29 April 1975	Eagle Pass, TX, USA	Collision	Propane	18	16d
14 December 1975	Niagara Falls, NY, USA	Runaway	Chlorine	20	4d
1975	Des Moines, IA, USA	LPG	Rail tank car	^	3i
11 May 1976	Houston, TX, USA	Collision	Ammonia	20	6d
31 August 1976	Gadsden, AL, USA	Fire	Gasoline	4	3d
1976	Belt, MN, USA	LPG	Rail tank car	80	22i
1977	Cartegna, Columbia	Overpressure	Ammonia	^	30d
1977	Dallas, TX, USA	Isobutene	Rail tank car	^	1i
1977	Goldona, VA, USA	LPG	Rail tank car	70	2d, 9i
22 February 1978	Waverly, TX, USA	Damage (Derail)	Propane	45	16d, 43i
11 July 1978	San Carlos, Spain	Overfilling	Propylene	25	211d
30 May 1978	Texas City, TX, USA	Fire	Butanes (6)	1500	7d, 10i
1978	Donnellson, IA, USA	LPG	Pipeline	435	2d, 2i
30 August 1979	Good Hope, LA, USA	Ship collision	Butane	120	12d
1979	Pazton, TX, USA	Chemicals	Rail tank car	^	8i
1979	Los Angeles, CA, USA	Gasoline	Road tanker	^	2d, 2i
1 August 1981	Montanas, Mexico	Damage (Derail)	Chlorine (2)	110	29d
19 January 1982	Spencer, OK, USA	Overheating	Water	0.3	7d
11 December 1982	Taft, LA, USA	Runaway	Acrolein	250	–
12 July 1983	Reserve, LA, USA	Runaway	Chlorobutadiene	1	3d

Date	Location	Cause	Material	Quantity (tonnes)	Death (d), injured (i)
4 October 1983	Houston, TX, USA	Overfilling	Methyl bromide	28	2d
19 November 1984	Mexico City, Mexico	Fire	Propane (20)	3000	650d, 6400i
1984	Romeoville, IL, USA	Propane	Process vessel	^a	15d, 22i
28 January 1986	Kennedy Space Center, FL, USA	Fire	Hydrogen	115	7d
1 April 1990	Boral LPG distribution depot, Sydney, Australia	Fire	LPG	>240	35,000 affected
1 April 1990	Cairns gas terminal, Queensland, Australia	Fire	LPG	^a	1d
28 August 1992	Japan	Damage	Nitrogen	^a	\$5 million loss
August 1993	Panipat, India	Pressure build-up	Ammonia	^a	6d, 25i
19 April 1993	Waco, TX, USA	Fire	LPG	^a	–
27 June 1993	Quebec, Canada	Fire	Propane	2.3	4d, 7i
4 March 1996	Weyauwega, WI, USA	Derailment	Propane, LPG	^a	–
18 March 1996	Palermo, Italy	Collision in a highway tunnel	Propane	^a	5d, 25i
2 October 1997	Burnside, IL, USA	Fire	LPG	3.8	2d, 2i
9 April 1998	Alberta City, IA, USA	Fire	Propane	40	2d, 7i
30 April 1999	Between Athens and Lamia, Greece	Traffic accident	LPG	^a	4d, 13i
23 September 1999	Toronto, Canada	Derailment	LPG	>60	–
30 December 1999	Quebec, Canada	Derailment, collision	Hydrocarbons	2700	2i, 350 evac.
27 May 2000	Eunice, LA, USA	Derailment	Flammable PLGs	^a	2000 evac.
19 July 2000	Ohio, USA	Overfilling	Propane	66	3i
7 January 2001	Kanpur, India	Highway accident	LPG	^a	12d, 6i
20 October 2000	Downey, CA, USA	Leak	Propane	2	2d
22 October 2000	Texas, USA	Improper unloading	Propane	17	2d
1 July 2001	Jamnagar, India	Damage	LPG	^a	12d
20 February 2002	Cairo, Egypt	Fire caused in a passenger train by a butane tank BLEVE	Butane	^a	373d, 7500i
22 June 2002	Tivissa, Spain	Overtumed	LNG	48 m ³	1d, 2i
25 June 2002	Gronton, CT, USA	Overheating	Borane-tetrahydrofuran	0.1	2i
11 April 2003	Louisville, USA	Overheating	Maltodextrin and other chemicals	^a	1d
13 January 2004	Baltimore, Washington Highway, USA	Traffic accident	Propane	^a	10d
19 January 2004	Skikida, Algeria	Explosion	LNG	^a	13d, 74i
9 August 2004	Mihama, Japan	Steam pipe depressurization	Steam	^a	4d, 7i

^a Information not available.

Figure 2.3: An illustrative list of some of the major BLEVEs from 1926 to 2004 [9].

2.2.2. Mechanism of BLEVE

In figure 2.4 it is shown the typical accidental chain of hazard events that can happen during the life cycle of a storage tank containing pressurized liquefied gas. It is composed by three phases:

1. Accidental phase;
2. Release phase;
3. Hazard phase.

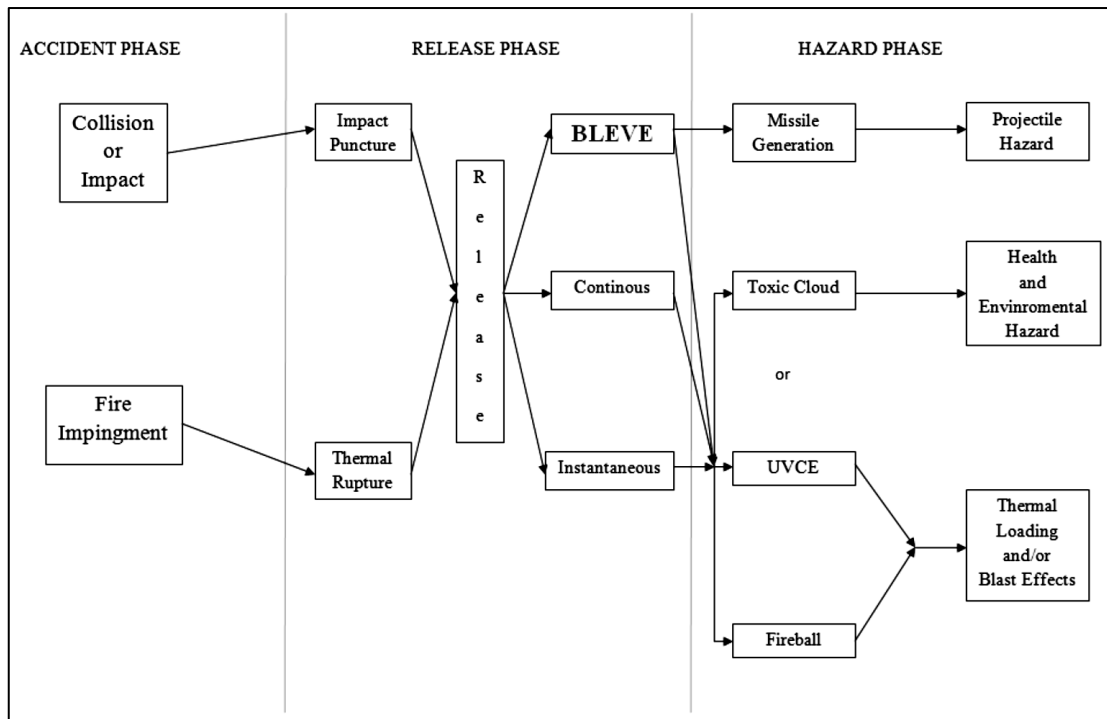


Figure 2.4: Accidental chain during the lifecycle of a storage tank [10].

To qualify a final outcome as a BLEVE, the following two features must occur simultaneously:

- Instantaneous depressurization:* the sudden and complete failure (TLOC: Total Loss of Containment), of the tank causes the expansion of the fluid from storage to atmospheric pressure, at which the liquid has a superheated thermal condition. Consequently the released liquid can flash and, if the superheat amount is significant, the flashing may be explosive.
- Significant superheating of the liquid:* once at the atmospheric pressure, the released fluid fulfills the condition of superheated liquid because its temperature is superior than the normal boiling point.

Over the years, researchers tried to explain the mechanism of BLEVE through the formulation of several theories. The first conclusions were proposed by Reid in the early '80 through the "Superheat Limit Theory" [11]. In this explanation, the value of superheat of the liquid interested in BLEVEs is quantified considering the "atmospheric superheat limit temperature (SLT)" of the fluid.

For several years, only the explosion during which the fluid reached the SLT value were considered BLEVEs. Actually the experimental research carried out by McDevitt et al. [12] shows that

BLEVEs can occur without reaching the atmospheric superheat limit, although according to Birk et al. [13], BLEVEs are most powerful if involving fluids at the SLT. For this reason, in a successive work, Birk et al. [14] divided BLEVEs in two categories:

- *Hot BLEVE (or Fire BLEVE)*: in this case, the liquid temperature is greater than Superheat Limit Temperature (SLT). The stored fluid, during its expansion, causes a “violent explosion” resulting in a fireball.
- *Cold BLEVE*: in this case, the liquid temperature is lower than the SLT. The explosion originates a pressure wave much weaker. Since the initiating event of BLEVE can be different by a external fire, it is possible that there is not ignition of the aerosols cloud and therefore the fireball does not develop.

Several methods were proposed for the calculation of the atmospheric superheat limit temperature. The first procedure was developed by Reid, who used a “thermodynamic stability approach”.

The explanation for this approach is based on the Amagat-Andrews diagram: it is shown in figure 2.5.

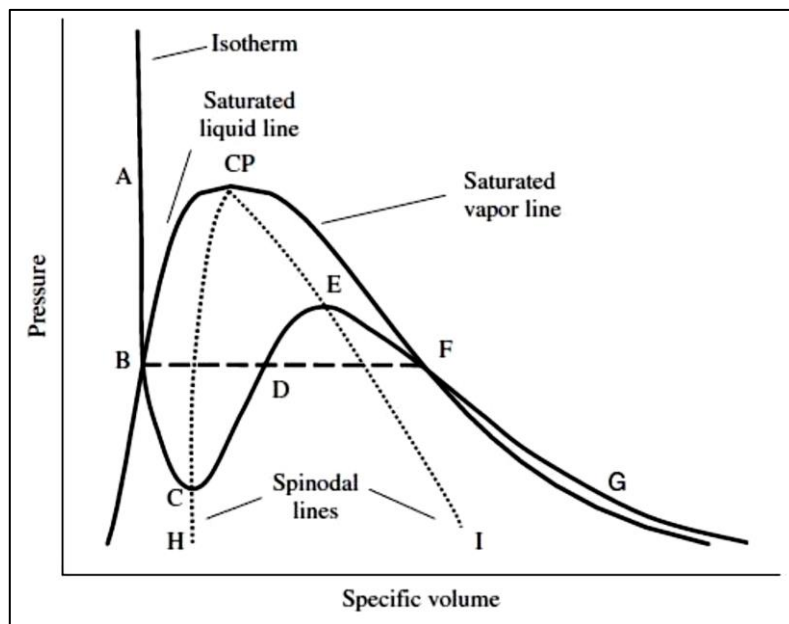


Figure 2.5: Liquid-Vapour equilibrium under depressurization at a constant temperature [15].

The “Saturated Line” delimitates the region of liquid and vapour coexistence: for a fluid in saturated conditions, saturated temperature is not independent from its pressure. The “Saturated Liquid Line” and “Saturated Vapor Line” join themselves in the Critical Point (CP), univocally determined by the Critical Temperature and Pressure (respectively T_C and P_C). The “BF Line” is

the tie–line and it represent all the possible liquid–vapour equilibrium combinations at a given temperature. The “ABCDEFGH Line” is an isotherm line, obtained using Redlich–Kwong Equation of State (RK–EOS). It is reported in figure 2.6:

$$\begin{aligned}
 P &= \frac{RT}{V-b} - \frac{a}{\sqrt{T}V(V-b)} \\
 a &= \frac{\Omega_a R^2 T_c^{2.5}}{P_c} \\
 b &= \frac{\Omega_b RT_c}{P_c} \\
 \Omega_a &= \left[9 \left(2^{1/3} - 1 \right) \right]^{-1} \\
 \Omega_b &= \frac{2^{1/3} - 1}{3}
 \end{aligned}$$

Figure 2.6: RK–EOS form [16].

At the moment of sudden failure of the storage tank, the fluid is in physical condition of pressurized liquid (A). Due to the depressurization, the fluid evolves from state A to state B at constant temperature, where it is not longer stable as mono–phase liquid. On the tie–line (BF), liquid and vapour phase can coexist at constant pressure and temperature. Actually, the transition from one phase (liquid phase) to two phase coexistence is more complex. Considering the “mechanical stability criterion”, which states that the pressure monotonically decreases with volume at constant temperature, it results:

$$\left(\frac{\partial P}{\partial V} \right)_T < 0 \quad (1)$$

This mathematical constraint means that the liquid phase can exist till to point C, for pressures lower then the saturation pressure, while the vapour phase till to point E, for pressures higher then the saturation pressure. For this reason, the transition from the liquid to the vapour state is not immediate: it can be possible for all the physical states between point C and E, or rather, for all completely unstable states corresponding to bi–phase liquid–vapour systems. BC stroke and EF stroke represent the metastable states of superheated liquid and supercooled vapour. Any perturbations make the fluid to evolve towards a two–phase configuration. Furthermore C point stands for the minimum pressure at which a metastable liquid can be found, for that specific temperature. The line H–C–CP is the locus of the minimum isotherms: it is called “*liquid spinodal curve*”. Instead, E point symbolizes the maximum pressure at which a metastable vapour can be found, for that specific temperature. The line I–E–CP is the locus of the maximum isotherms: it is called “*vapour spinodal curve*”.

From a physical point of view, the SLT has a double meaning [11]:

- a. At a constant pressure, the SLT is the maximum temperature which a fluid can sustain without undergoing a phase transition;
- b. At a constant pressure and at the SLT, the fluid is interested by spontaneous homogeneous nucleation.

There are two ways for a fluid to reaching the SLT: at a constant pressure or at a constant temperature. This last condition occurs during the sudden depressurization of a Pressure Liquefied Gas vessel: at the new final pressure (Atmospheric pressure), the released Pressurized Liquefied Gas is at a major temperature than its normal boiling point. Actually this is a metastable condition, so instantaneous flash follows the sudden depressurization of the released Pressurized Liquefied Gas, spreading a biphasic liquid/vapour mixture. This flash phenomenon takes place in a few milliseconds.

According to the early work by Katz [17] and Reid [11], using thermodynamic stability approach, is possible to find the SLT value using the analytic expression of an EOS to estimate the liquid spinodal curve. The necessary data to perform this evaluation are critical temperature (T_C), critical pressure (P_C) and acentric factor (ω) of the fluid.

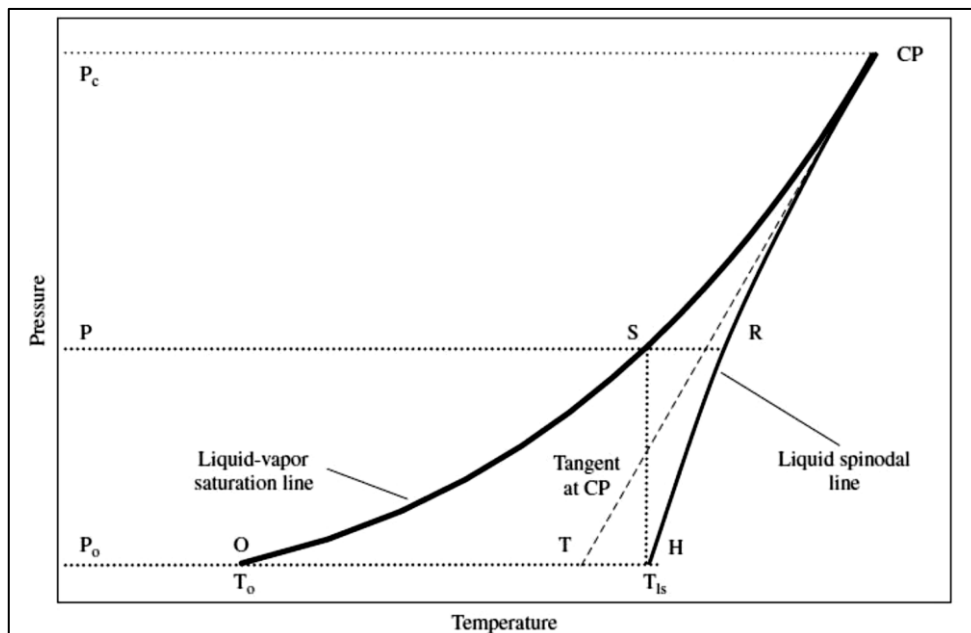


Figure 2.7: Liquid spinodal curve and tangent line to the saturation curva at critical point [15].

Depending on the analytical form of EOS, can be found in the value of SLT predicted difference of about 30K. For this reason some authors have purposed simplified equation to estimate the SLT value:

1. Reid (1983):
$$T_{ls} = 0.895 T_C \quad (2)$$

2. Sigalès and Trujillo [S&T] (1990):
$$T_{ls} = 0.822 T_C + 0.105 T_{atm} \quad (3)$$

3. CCPS (1994):
$$T_{ls} = T_0 \left[0.11 \left(\frac{P_{atm}}{P_C} \right) + 0.89 \right] \quad (4)$$

Another similar but simplified model to assess the SLT value, consist in the use of the tangential line of the equilibrium curve at the critical point. Both Clausius–Clapeyron or Antoine equations as analytical expressions of pressure dependence on temperature, can be used to draw the tangent line. Actually this approach is conservative because it predicts lower SLT values than the thermodynamics stability approach: all tangent line fall between saturation curve and liquid spinodal line. This type of approach is reported in figure 2.7.

In a recent study by J.M. Salla et al. [15], used the energy balance to the released fluid mass to obtain the SLT. They demonstrated that the SLT is the value of temperature at which the partial vaporization of the flashing fluid leads remaining liquid to a minimum content of energy. The values of SLT are similar to those obtained with the classical methods, with the advantage that SLT is a function of the properties of the substance involved and so the influence of the EOS is lost.

In table 2.1 and 2.2, are reported respectively the critical constant of the substance considered in this thesis (propane) and the SLT value assessed with several criterion.

<i>SUBSTANCE</i>	<i>T₀ (K)</i>	<i>T_c (K)</i>	<i>P_c (MPa)</i>	<i>ω</i>
Propane	231.1	369.8	4.2	0.1523

Table 2.1: Critical constant for propane pure [25].

SLT VALUES (K)						
<i>RK-EOS</i>	<i>WdW-EOS</i>	<i>Reid Corr.</i>	<i>S&T Corr.</i>	<i>CCPS Corr.</i>	<i>T-line</i>	<i>Salla et al. [15]</i>
332.0	313.5	331.0	328.3	330.1	326.8	315.3

Table 2.2: SLT value prediction for propane pure with several criterion

2.2.3. Fireball associated to BLEVE

Fireball is a fire final outcome that occurs when a given amount of flammable vapour or gas, previously confined at relevant pressure, is suddently released into the atmosphere due to

acatastrophic rupture of the vessel, and is ignited [4]. If a pressurized liquefied gas is contained in the vessel, the liquid is entrained by the vapour in the release after the massive loss of containment, resulting in a BLEVE. This explosion leads to the formation of aerosols cloud, with high energy. If the substance is flammable and in presence of a ignition source, the cloud triggers resulting in a serious fireball.

In most cases, Fireballs are caused by BLEVE, but it is important to distinguish between two final outcomes: a BLEVE originates a fireball only if the fluid is flammable and if a ignition source is present. If the substance is flammable, but there is not a immediate trigger, the dispersion may lead to delayed final outcomes as a Flash Fire (FF) or Vapor Cloud Explosion (VCE).

Fireball is typically a transient and short–time phenomenon (about 2–3 minutes). Thus, understanding its evolution during time is crucial for the modeling of the heat flux of this type of fire. It passes through three phases [1]: (1) growth, (2) steady burning and (3) burnout. The figure 2.8 illastrates the typical development of a fireball as a function of time and the mentioned phases.

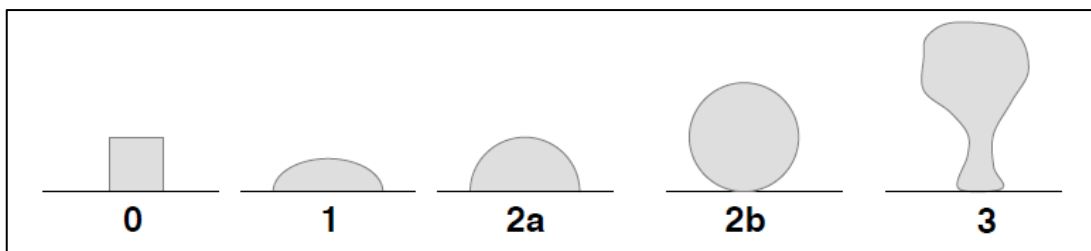


Figure 2.8: Development of the typical fireball from a source at ground level [4].

The growth phase may be divided into two intervals, each lasting about 1 second. In the first interval the flame boundary is luminous with yellowish–white flames indicating a flame temperature of about 1300°C. The fireball grows to about half its final diameter and the droplets with diameter less than 4-5 mm would vaporize, resulting in a good mixing with air. In the second interval of the growth phase, the fireball grows to its final volume, but about 10% of the surface is dark and sooty with the rest being white, yellowish–orange or light red, indicating flame temperatures in the range 900–1300 °C, with an estimated effective flame temperature of 1100–1200 °C.

In the second phase, which lasts some 10 seconds, the fireball, which is now roughly spherical, is no longer growing. At the start of this phase it begins to lift off. It rises and changes to the familiar mushroom shape. The estimated effective flame temperature is 1100–1200 °C.

In the third phase, which lasts some 5 seconds, fireball remains of the same size, but the flame becomes less sooty and more translucent.

Figure 2.9 shows the shape of fireball as a function of time.

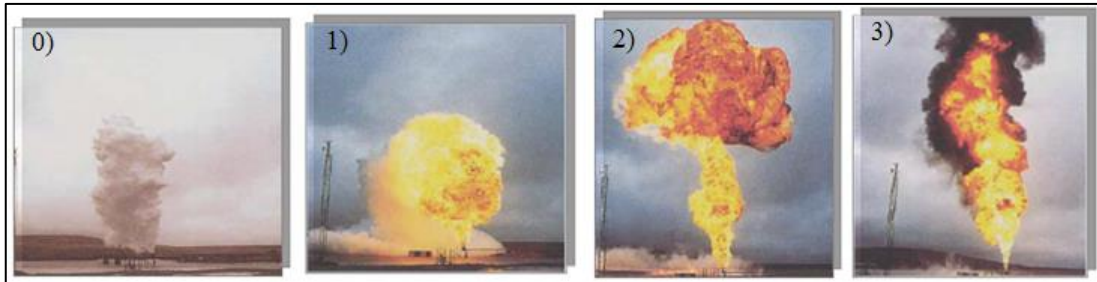


Figure 2.9: Shape of fireball as a function of time: 0) ignition, 1) growth, 2) steady burning and lift off, 3) burnout [4].

3. Theoretical analysis of transport and storage vessels exposed to fire

During the rupture of the vessel, regardless of the fact that the temperature is major or less than Superheat Limit Temperature (SLT), the sudden depressurization causes a strong blast wave. For any type of BLEVE (Hot or Cold), the blast wave has a magnitude very higher than the blast wave resulting by other explosive scenarios, such as a “Vapor Cloud Explosion” (VCE). Depending from a initiating event that leads to BLEVE, the cloud of aerosols can generate a fireball, in case the fluid is flammable, or it can spread into the atmosphere, whit extremely dangerous consequences in case the fluid is toxic. There is a possibility that a part of the liquid rain–out to a ground, forming a boiling pool. This quickly evaporates and the vapor can ignite easily (if the fluid is flammable).

The causes of BLEVEs, as already mentioned, can be different: external fires, derailments, overfilling of the tank, runaway phenomenon, collision, overpressure or other. In a work, Prugh says that the most part of BLEVEs are caused by a external fire [18]. This assertion is confirmed by a historical analysis of accident happened between 1995 and 2004, compiled by Abbasi et al. and reported in one of his paper [9]: it is summarized in table 3.1. It shows the main initiating event resulting in a BLEVE:

INITIATING EVENT	%
Fire	36
Mechanical damage	22
Overfilling	20
Runaway reactions	12
Overheating	6
Vapour space containment	2
Mechanical failure	2

Table 3.1: Frequency of BLEVEs initiating events[9].

For this reason, it is important to study the response of tanks engulfed or exposed to fire. The main parameter to assess are:

- Increase of Vessel Wall Temperature as a function of the time;
- Increase of Internal Fluid Temperature as a function of the time;

- Effect of the Liquid Thermal Stratification Phenomenon.

Knowledge of these parameters allow to assess the “tff (time to failure)” and the ways to increase it, in order to preventing the catastrophic failure and then the BLEVE.

3.1. Dynamics of the Wall Temperature of tank involved in fire

The Hot–Bleve is often referred to as a BLEVE induced by a fire: for this reason is used the term Fire–BLEVE. The fire as initiating BLEVE event can assume one of the following shape:

1. A Pool Fire: it consists in the uncontrolled combustion of the vapors generated from a pool of a flammable liquid;
2. A Jet Fire: loss of containment from a pressurized vessel containing a flammable gas or a flashing liquid may result in a jet fire, if ignition takes place.
3. A Fireball resulting from a previous BLEVE occurred on a other equipment containing flammable pressurized liquefied gas.

When the vessel is exposed to a mentioned fire, the stored LPG is subjected to a significant amount of heat, due to radiative and in some cases convective flux heat. If the fire exposure lasts for sufficient time, the vessel may fail in a relatively short time called time to failure (tff). The failure mode can be:

- a) A total loss of containment, TLOC: in this case, the vessel undergoes a catastrophic rupture with consequent release of all the stored fluid. This scenario leads a one–stage BLEVE.
- b) Partial damage with formation of small tears that suddenly stop their growth. Vapour energy is spent in the pressure drop as vapour can escape from the fracture, called “leak before break (LBB)” [19]. If the pressure drop is very rapid, the liquid may violently flash: in this circumstance, the equipment is subjected at high stress and this can restart the crack and cause the TLOC. This scenario leads at two–stage BLEVE.

In order to be able to assess the hazard posed from fire engulfment of LPG storage vessel and predict its tff, is important to understand the failure mechanism of tank. Two are the reasons that may lead to the total loss of containment of a vessel during an external fire accidental scenario:

1. Decrease of the vessel’s overpressure resistance caused by a rising tank shell temperature.
2. Increase of inner pressure caused by the LPG rising temperature and no sufficient pressure relief of the safety valve (PRV).

The evolution of these two phenomena over time brings the vessel in conditions in which the equivalent stress σ_{eq} , representing the stress to which the equipment is subjected, reaches the admissible stress σ_{adm} , which is the maximum stress that the shell can support. This is the failure point and the time at which this occurs is the ttf. The trend of equivalent stress and admissible stress during the fire exposure is reported in figure 3.1.

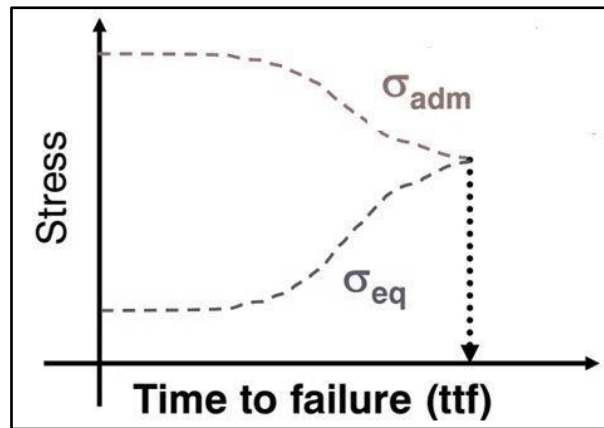


Figure 3.1: Trend as a function of time of equivalent and admissible stress [2].

Steel mechanical and structural response to applied loads can be expressed by the “stress and strain Curve”, reported in figure 3.2 [20].

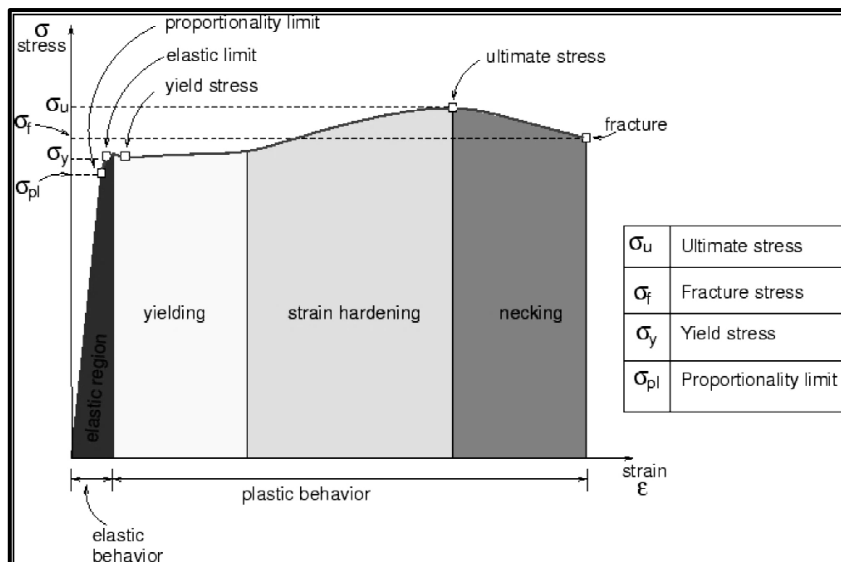


Figure 3.2: Stress and Strain Curve for Steel [20].

Thanks to the previous diagram is possible to evaluate the strain ($\tilde{\epsilon}$) resulting in a frame of steel after the application on it of a strength (F). Being A_0 and l_0 the initial cross-section and length of the steel frame, it is possible to define:

$$\sigma = \frac{F}{A_0} \quad (5a) \quad \text{and} \quad \tilde{\epsilon} = \frac{l - l_0}{l_0} \quad (5b)$$

The stress and strain plane is composed by four different regions, each one of them identifies a specific mechanical behaviour:

1. *Elastic region*: for stress minor or at most equal to the Yield Stress value, the material deformations are reversible. From an analytical point of view this means that a linear dependence exists between stress and strain: the proportionality coefficient is represented by the Young' module (E), that is an indicator of the material stiffness:

$$\sigma = \mathbf{E} \cdot \tilde{\epsilon} \quad (6)$$

The yield point represents the value of the admissible strength that a material frame of thickness s and diameter D can sustain with reversible deformations. It is used as a design value. The admissible stress is calculated dividing the yield stress for the the security coefficient φ , which value are major than 1 (typically 1.5–2). This relation is reported in the following equation:

$$\sigma_{\text{adm}} = \frac{\sigma_Y}{\varphi} \quad (7)$$

Knowing the yield stress and the geometrical parameters of tank, it is possible to assess the maximum pressure that the equipment can sustain, applying the Mariotte's law, reported in the equation (8):

$$\sigma_{\text{adm}} = \frac{P_{\text{MAX}} D}{2s} \quad (8)$$

2. *Yielding region*: the application of major strain than the elastic limit value produces plastic deformation which is irreversible.
3. *Strain hardening region*: the ensemble of plastic deformations ends with the maximum value of stress for the material called ultimate tensile strength: it is a measure of the material resistance to tensile loads. In this zone a necking of the cross section of the frame takes place.
4. *Necking region*: the necking continues till the rupture of the frame for fragile rupture.

The mechanical properties of a material frame depend intimately from the temperature at which they are recorded. For rising temperatures the value of Young' module, Yield Stress and Ultimate Tensile Strength decrease. Consequently at high temperature it results a weakening of the equipment material and then the ttf is lower yet. Typically, the temperature at which there is a net reduction of the Tensile Strength is equal to 0,3–0,5 times the melting temperature.

According to the works of Keltner et al. [21] and Townsend et al. [22], effective flame temperatures of an Hydrocarbon fuel pool fire ranges between 700 and 900°C. the torch temperature resulting by a jet fire may be even higher than from a pool fire, reaching 900–1200°C [23]. In table 3.2, the typical pool fire and jet fire temperature are reported [24].

Fire Type	Open Pool Fires	Confined Pool Fires	Open Jet Fires	Confined Jet Fires
<i>Total incident flux (kW m⁻²)</i>	50-150	100-250	100-400	150-400
<i>Radiative flux (kW m⁻²)</i>	50-150	100-230	50-250	100-300
<i>Convective flux (kW m⁻²)</i>	-	0-20	50-150	50-100
<i>Emissivity of flame</i>	0.7-0.9	0.8-0.9	0.5-0.9	0.8-0.9
<i>Temperature of flame (K)</i>	1000-1400	1200-1450	1200-1500	1200-1600
<i>Heat transfer coefficient (kW m⁻² K⁻¹)</i>	-	0-0.02	0.04-0.17	0.04-0.11

Table 3.2: Typical parameters for the main Fires [24].

In vessel containing pressurized liquefied gas, subject of this study, the wall temperature is strongly dependent from the nature of the stored fluid: if the flame temperature is applied to a vessel below the liquid level, the liquid in contact with the inside wall surface is usually capable of maintaining the wall temperature near the liquid temperature, thanks to the high heat transfer coefficients of this phase. This does not hold true if the local heat flux exceeds the critical heat flux for the liquid: in this case, the liquid is not in contact with the inner wall due to the presence of a vapour film, that acts by insulating for the heat transfer. However, with a jet fire or a pool fire, this condition is unlikely to be reached because, considering a tank containing propane at ambient temperature, the critical heat flux is about 600 kW/m². Conversely, the vapour has a low thermal conductivity: for this reason, the wall temperature in contact with this phase increases very quickly and reaches a high value in a short time.

From a qualitative point of view, a high fill liquid level tends to slow the heating up process of the vessel wall, due to its high heat transfer coefficient: the liquid provides a coolant action decreasing the temperature of the wall. So it is the vapour space wall temperature that usually define the

failure sequence: it is in the vapour space that the wall temperature is high enough to destroy the tank.

It is possible to summarize the steel tank response to fire impingement considering the thermal properties (thermal conductivity and specific heat), the mechanical properties (Yield strength, ultimate tensile strength, Young module) and the deformation properties (tertiary creep phenomena).

BLEVE depends on both tank strength and the stored energy because the heating of the vessel content results in rising of the temperature and the pressure of the fluid. A correct PSV design is very important, but the tank can fail due to wall strength degradation at high temperatures even though the vessel pressure is within design limits: in this case, before PRV opening, the Total loss of Containment (TLOC) of tank occurs. Figure 3.3 shows the sequence of events required to reach the BLEVE [26].

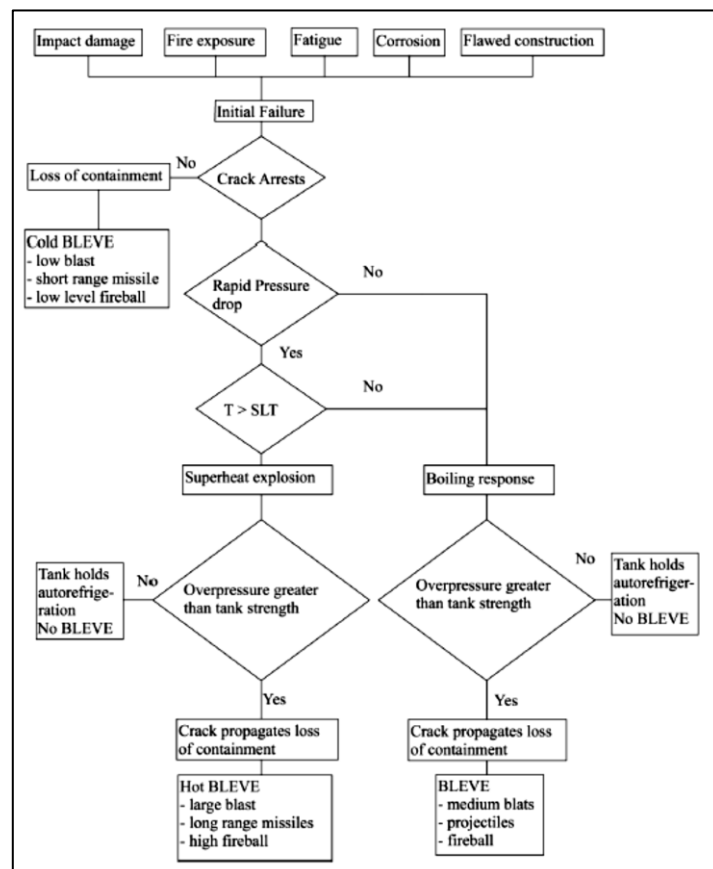


Figure 3.3: The sequence events required for the BLEVE outcome [26].

3.2. Dynamics behaviour of the Stored Fluid Temperature in the vessel involved in fire

One of the key parameters to understand the behavior of tank involved in a fire is the assessing of the internal fluid temperature. When a pressurized vessel is exposed to fire, the radiative and convective heat load of flame is transferred by conduction through the vessel wall and then it is received by the stored fluid. The heat-up of tank results in the vapour and liquid phase rising temperature.

To the initial state, or rather when the fire takes place, the liquid and vapour phase are saturated at the storage pressure and at ambient temperature. During the heating, the behavior of vapour and liquid phase is far different.

Initially, due to the low thermal conductivity and of the absence of convective motions, the vapour is thermally stable. As heating progresses the vapour portion of the lading becomes superheated and severely stratified. The main heat transfer mechanisms in the vapour space are the *natural convection* and the *radiation* (when the inner wall temperature rise thermal radiation becomes important).

In the liquid phase, the heat transfer mechanism from steel wall to lading fluid is more significant. The initial mode of heat transfer is pure *natural convection*. During the heating, the liquid particles near the wall begin rising along it until the liquid-vapor interface. Upon reaching the liquid surface these particles spread towards the centre and fall back into the bulk region of the fluid. Once lost heat, they re-enter in zone near the wall boundary layer to repeat the above process. The main effects of this gravity driven recirculation flow is the establishment of a vertical temperature gradient inside the tank: after a little time, the liquid became thermally stratified [27] (see figure 3.5). Due to this phenomenon, the liquid on the free surface has a higher temperature than the bulk liquid: the pressure in the vessel is controlled by this warmest liquid layer. It is possible to divide the lading liquid domain in three different zones: (1) the bulk liquid, in which the subcooled liquid is present; (2) the stratified liquid layer, that is the zona from bulk to liquid-vapour interface; (3) the boundary liquid layer, that is the zone near to the hot wall, in which the liquid rises up to reach the interface due to the natural convection[27].

Figure 3.4 shows the several zones and the physical model for thermohydraulic behaviour of the fluid containing in the vessel exposed to fire [42].

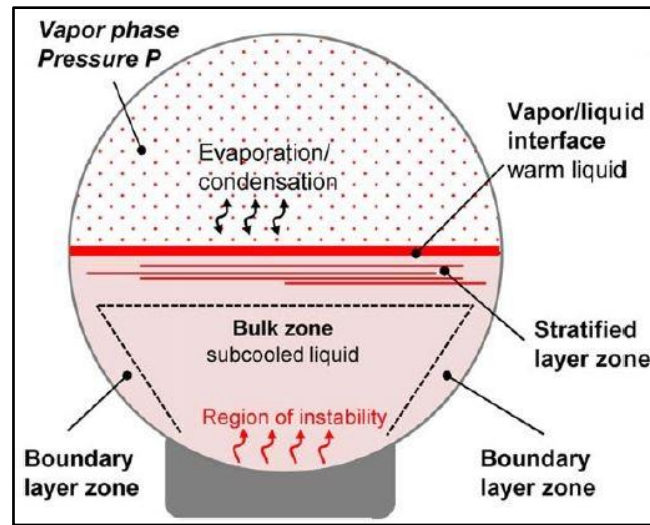


Figure 3.4: Physical model for thermohydraulic behaviour [42]

Another interesting observation emerged from the laboratory experiments is the existence of vertically-upwards fluid motion near the bottom of the horizontal cylinder. In the region of instability, the fluid particles rise directly upwards and mix with the bulk of the fluid instead of attaching to the wall to form a boundary layer. This mechanism is important since it provides direct heating to the central core regions (in which subcooled liquid is present) and also retards the initiation of the boundary layer [27].

As heating progresses, the part of the liquid in the Region of Instability and in the Boundary Layer may exceed its saturation temperature at the pressure controlled by the warmest liquid. This leads to *heterogeneous nucleation* near the wall. If the liquid superheat is not sufficient to sustain the vapour bubbles growth, they collapse while reaching the vapour-liquid interface [27]. For this reason, thanks to the difference between wall temperature and liquid saturation temperature at the storage pressure, a considerable vapour generation occurs in the near wall region. As already mentioned, it is not credible that a pool fire or a jet fire provides a heat flux higher than critical heat flux: consequently, the transition from nucleate boiling and film boiling does not occur.

Figure 3.5 summarizes the interacting processes which affect pressurized vessels storing liquefied gas during a fire attack. Although a section of a horizontal cylindrical vessel is shown in the figure, the fundamental phenomena involved are present in any type of vessel and geometry of industrial relevance [42].

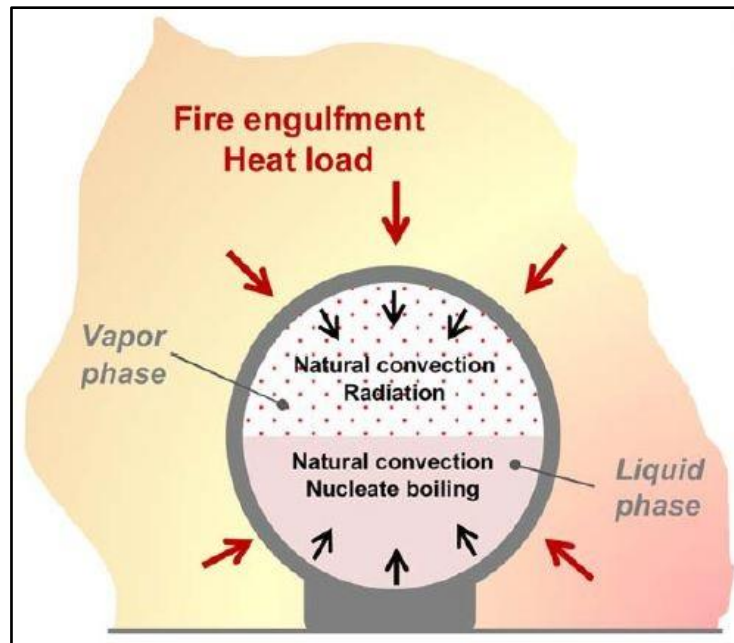


Figure 3.5: Physical phenomena involved in vessel heat-up [42].

Then, during the fire exposure of a tank containing LPG, the main transport phenomena can be summarized as:

- Heat transfer between the fire and the outer surface of the wall of the vessel due to radiative or/and convective heat load;
- Heat transfer through the tanks wall by conduction;
- Heat transfer between the inner surface of the near vapour wall and the lading vapour due to natural convection and radiation;
- Heat transfer between the inner surface of the near liquid wall and the lading liquid due to natural convection and nucleate boiling;
- Mass transfer within the liquid phase by flow of the heated fluid into the stratified hot layer lying above the bulk liquid;
- Mass transfer between the liquid and vapour phases due to evaporation.

3.3. The effect of liquid thermal stratification phenomenon

As already mentioned, in a tank exposed to fire containing a liquid phase, the stored liquid is not usually homogeneous: while heated, the near-wall liquid becomes hot and less dense so it rises reaching the interface with the vapour. The liquid temperature varies significantly from the bottom to the liquid-vapour interface, because the presence of buoyancy leads thermal stratification to

build up in the storage vessel: the warmest liquid joins the interface. Once generated the stratification continues to affect the stored liquid until other processes dissipate the temperature gradients, such as PRV opening: this means that the stratification is a stable phenomenon that becomes more evident with elapsing time. Figure 3.6 shown the evolution of the liquid thermal stratification phenomenon for two different time, before the PRV opening [42].

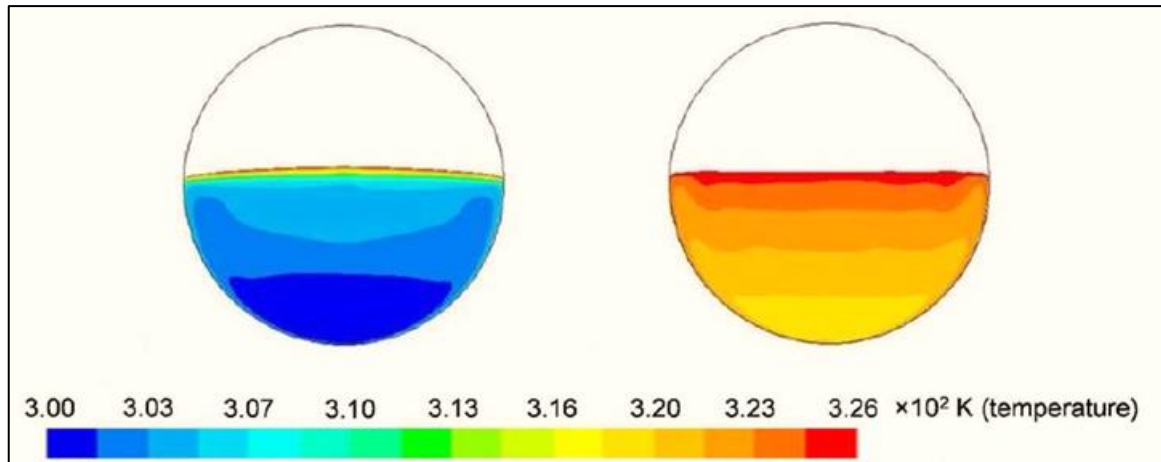


Figure 3.6: Trend of the liquid temperature (K) for two successive time, respectively 150s and 450s (adopted by source [42]).

The thermal stratification phenomenon is a function of the relative strengths of buoyancy, viscous and inertia forces coming into play. Per a given fluid, the ratio between the buoyancy force and the viscous force acting on it is expressed by the dimensionless Grashof Number (Gr), while a measure of the fluid inertia is given by the ratio between the momentum diffusivity and the thermal diffusivity, expressed through the dimensionless Prandtl Number (Pr). The product between Prandtl Number and Grashof Number identifies the Rayleigh Number, which value is related to the thickness of the stratification layer: the higher is the Rayleigh Number (Ra), the higher is the thickness of the stratification layer. In the next equations are reported the definitions for these dimensionless Numbers, where X is the horizontal axis and Y the vertical axis.:

$$Gr_Y = \frac{\rho^2 \beta g y^3 (T_{wall} - T_{bulk})}{\mu^2} \quad (9)$$

$$Pr = \frac{c_P \mu}{k} \quad (10)$$

$$Ra_Y = Gr_Y \cdot Pr \quad (11)$$

The Rayleigh Number is important to assess the regime of the natural convection. For values less than 10^8 the regime is laminar, while for values major than 10^{10} it is turbulent.

As evidenced in several experimental tests (Birk et al. [13], Gong et al. [28], Lin et al [29], Yu et al. [30]), the presence of stratified temperature in stored liquid influences significantly the behaviour of tank. A survey of their studies and experiments leads summarizing the principal features that affect the stratification of temperature in the following [13]:

- Liquid thermal and transport properties;
- Liquid filling level and the geometry of tank;
- Distribution of impinging and heat load provided;
- PRV operation (cycling or continuous).

The geometry and the fill level of tank affects the stratification phenomenon. The studies of Hadjisophocleous et al. [31] and Gong et al. [28] has shown that the liquid thermal stratification is more severe if increase the diameter of tank and decrease the fill liquid level. The stratification can be neglected in case of low filling level tanks: in this case there is not enough space to allow a temperature gradient, the convective flow basically recirculate on itself. In particular, the stratification phenomenon does not occur when the fill liquid liquid is less than 40%. Gursu et al [32] proposed exponential laws to correlate the vertical dimension with temperature, amount of stored heat and mass. These are:

$$T(y) = ay^n \quad (12)$$

$$Q(y) = by \quad (13)$$

$$m(y) = cy^{\frac{8}{7}} \quad (14)$$

The heat amount Q and the mass m of the stored liquid that flows into the stratification region are proportional to y and $y^{8/7}$, respectively, where y is the height of the liquid. Consequently, when the filling level increases, the mass in the stratification regions rises faster than the heat amount added. In this way the degree of the liquid thermal stratification, in the stratified region, decreases [32].

The warmest layer of the stratified liquid determines the pressure of the storage vessel or rather the PRV opening pressure value: so as to quantify the influence of thermal stratification on tank reached pressure it is possible to introduce the dimensionless parameter Π [13]. In presence of stratification, the Π value is always major than 1, since pressure in the vessel is controlled by the

warmest liquid layer. The saturation pressure at the average lading liquid phase temperature is greatly less than the saturation pressure at the temperature of the warmest liquid layer.

Therefore the contribution of thermal stratification regards the PRV design and the PRV opening pressure value too. In the thermally stratified liquid phase, the PRV opening pressure value is reached faster than in a thermally homogeneous liquid phase, due to the faster growth of the warmest liquid layer temperature. The PRV opening pressure controls the maximum π value: this is very important for a correct design of the PRV. Based on the experiments and on simple thermodynamics considerations, it is clear that higher PRV set pressures increase the chance of a BLEVE because high opening pressure results in increased liquid and vapour stored energy. Therefore, PRV set pressures should be set as low as practical for the application [13]. Recent studies have shown that, to prevent the BLEVE, PRV set pressures should not be near the atmospheric superheat limit as this conditions maximizes the strength of the liquid boiling response upon sudden depressurization. For propane the atmospheric superheat limit temperature (52°C) should be considered the upper limit for setting PRV pressure since it is a real indication of the severity of the liquid boiling response upon sudden depressurization. For propane then, the upper limit on set pressures should be around 1.7 MPag. If this setting is exceeded for practical reasons, the tank strength should be increased to reduce the chance of thermal failure [13].

The stored energy in lading liquid phase depends not only by the opening pressure value of the PRV but also on its operating mode. It is possible to recognize two different operating modes for a PRV: (1) cycling outflow and (2) continuous outflow. When the PRV opens and vents vapour, the depressurization leads a boiling process (flash), that consumes energy in the warmest liquid layers and the resulting bubble rise causes mixing in the warmest layer, so the combination of these effect reduces the stratification. It is clear that a cycling PRV, leads the regeneration of the stratification while it is closed.

The stratification phenomenon affects also the PRV opening time. In major part of simplified numericals models and lumped parameters models, this phenomenon is ignored and then the predictions are incorrect. These tools are able to assess the response of both the vessel and its content when engulfed in fire, but, neglecting the action of the liquid thermal stratification, it predicts an average tank pressure value lower than the pressure value that is dictated by the warmest liquid layer of the thermal stratified liquid phases, so leading to greatest PRV opening time value. In addition to control the pressure in the vessel and to affect on the PRV time opening, the stratification phenomenon influence the BLEVE and its consequences [13]. Actually the liquid stratification decreases the liquid energy, so it decreases [28]:

1. The liquid energy affecting the development of the crack during BLEVE could be described as:

$$E_L = f\left(\frac{T^0(P) - T_{SL}}{T_{SL}}, V_L\right) \quad (15)$$

where T_{SL} is the atmospheric superheat limit (K) and V_L the liquid volume fill level (m^3).

2. The energy released by the stored fluid during the BLEVE is:

$$W = 0.024 \frac{PV^*}{\gamma - 1} \left[1 - \left(\frac{P_{ATM}}{P} \right)^{\frac{\gamma-1}{\gamma}} \right] \quad (16)$$

where W is the TNT equivalent mass and V^* is the sum of the vapour contained in the tank and the liquid that can flash due to depressurization provided by the loss of containment of BLEVE.

Being the stored energy in a liquid phase a function of V_L^* , the energy of BLEVE W is lower in conditions of liquid thermal stratification. To assess V^* can be used the following correlations:

$$V^* = V_V + V_L^* \quad (17)$$

$$V_L^* = \pi R^2 \int_0^{\delta_S} \left(\frac{c_P(T - T_{BULK})}{\lambda^0} \right) \left(\frac{\rho_{L0}}{\rho_v} \right) dx + \\ + \pi R^2 (h_L - \delta_S) \left(\frac{c_P(T - T_{BULK})}{\lambda^0} \right) \left(\frac{\rho_{L0}}{\rho_v} \right) \quad (18)$$

where δ_S is the thickness of the stratification layer.

Three are the main important effects of stratification on the consequences of BLEVE:

- Burst energy: since liquid stratification reduces the average liquid temperature then the blast strenght is also reduced.
- Projectile hazard: the higher is the isentropic expansion energy and the further the projectiles can be sent. With stratification phenomenon the liquid stores less energy and so it will produce less projectile hazard.

- Fireball: at a given pressure liquid stratification will affect the way the liquid flashes and expands. Strong stratification results in a small fraction of liquid flashing to vapour, thus evolving in different fireball. Observations from the tests of 400 liters Propane tanks suggest that BLEVEs, where the liquid is significantly stratified, give large ground fires and delayed or no fireball liftoff. This then suggests that liquid stratification may increase the fire hazard to close targets because of reduced liftoff and larger ground fire [13].

Finally, it is possible to summarize the effects of liquid thermal stratification as follow [13]:

- I. For the same tank pressure, the total liquid energy is less when the liquid is stratified;
- II. If the liquid is stratified, the PRV opening time is less than in the case the liquid temperature is uniform;
- III. Upon sudden depressurization, less liquid superheat is achieved with a stratified liquid and this effects the boiling response and pressure recovery;
- IV. Reduced liquid energy reduces momentum of release which affects size and liftoff of fireball;
- V. Less energy in liquid reduces blast and projectiles;
- VI. Less liquid energy may increase ground fire hazard;
- VII. Less liquid energy reduces chance of BLEVE.

The liquid temperature stratification is affected by scale, the fire exposure type, and the PRV action. It takes longer for large scale tanks to destratify. It takes longer for tanks partially engulfed by fire to destratify due to the reduced PRV flow. Cycling PRVs appear to slow the rate of destratification.

4. Experimental and numerical studies of pressurized vessel exposed to fire: state of the art

In this chapter are reported the results of specific studies on equipment affected by fires. The previous studies are mainly divided in two categories: experimental studies and numerical studies. The first one have played an essential role to understand the mechanisms and the key parameters that lead to hazardous scenarios. The last one are developed to replace the experimental tests and nowadays they are the main tools used for these studies.

4.1. Experimental studies

4.1.1. Introduction

Experimental studies of fire effects on pressure vessels has been conducted by numerous groups. However, the experimental work published over the last four decades was mainly undertaken in order to investigate the behaviour of pressurized vessels engulfed in flames, while scarce attention has been dedicated to the experimental analysis of the behaviour of the other types of vessel, and in particular of atmospheric tanks.

Figures 4.1 and 4.2 report a concise summary of the more significant experimental studies carried out on pressurized equipment exposed to fires [6]. Figure 4.1 focuses on experiments carried out on unprotected pressurized vessels (with pressure relief valves, PRVs), which allowed obtaining sufficiently detailed data to describe the behaviour of such vessels in conditions similar to those corresponding to an involvement in an external fire event. Figure 5.2 summarizes the experimental setup used for the analysis of passive fire protection (PFP) systems and the available results.

The typical setup of a vessel fire test is characterized by two key elements: a heat source and the target equipment. The heat source is aimed at the experimental simulation of a fire affecting the process equipment. In particular, confined pool fires with diesel or jet fuels are often employed to create a full engulfment in flames, while torch or jet fires are employed for partial or total engulfment. As shown in figures 4.1 and 4.2, the typical heat load due to an engulfing pool fire is in the order of 100–400 while for large jet fires it may be as high as 200 kW·m⁻² or even higher.

Test ID	EXP1	EXP2	EXP3	EXP4	EXP5	EXP6	EXP7
Data source	Townsend et al. (1974)	Droste et al. (1999)	Moodie et al. (1988)	Droste and Schoen (1988)	Persaud et al. (2001)	Birk et al. (2006a)	Birk and Van der Steen (2006)
Tank Specifications							
Tank geometry	Hor. Cyl.	Hor. Cyl.	Hor. Cyl.	Hor. Cyl.	Hor. Cyl.	Hor. Cyl.	Hor. Cyl.
External diameter (m)	3.05	2.9	1.7	1.25	1.2	0.953	0.953
Total length (m)	18.3	7.6	4.88	4.3	4.0	3.07	3.07
Minimum wall thickness (mm)	15.9	14.9	12.1	5.9	7.1	7.4	7.1
Type of material	TC-128 LCS*	LCS*	BS1500 LCS*	STE-36 LCS*	LCS*	SA455 LCS*	SA455 LCS*
Stored substance	Propane	Propane	LPG	Propane	Propane	Propane	Propane
Tested filling level(s) (%)	96	22	22,36,38,58,72	50	20,41,60,85	78	80
Pressure Relief Device Data							
Set pressure (MPag)	1.86	2.70	1.43	1.56	1.82	2.63	1.9
Pressure relief device nominal diameter (mm)	80	–	100	25.4	90	15 [‡]	21–24 [‡]
Number	1	0	2	1	1	1	1
External Heat Source							
Type of source	JP-4 pool fire	Fuel oil pool fire	Kerosene pool fire	Fuel oil pool fire	Propane jet fire	Butane burners	Butane burners
Ambient temperature (°C)	21.1	N.D.	1 ÷ 6.4	10, 2, –3	2	17, 20	10–20
Exposure mode	Full engulfment	Full engulfment [†]	Full engulfment	Surrounding fire	Full engulfment	Partial engulfment	Partial engulfment
Flame temperature (°C)	650–990	1200	–	843	900–1100	815–927	815–927
Measured heat flux (kW/m ²)	123–138	–	100	–	180–200	–	–

*LCS = low-carbon steel.
[†]Strong wind effects did not allow the effective engulfment of the vessel surface.
[‡]Computer operated.

Figure 4.1: Summary of Relevant Literature Experiments on Unprotected Pressurized Vessels exposed to fire [6].

The target equipment usually consists of medium or small scale cylindrical or spherical vessels featuring volumes ranging from 0.5 and 5 m³ with LPG at different grades and featuring different filling levels. Only in the works of Townsend et al (1974) [22] and Droste et al. (1999) [66] large scale vessel (respectively, 128 and 45 m³) have been studied experimentally.

These vessels are representative of both bulk storage and transport units. In these experiments the target equipment is usually equipped with sensors for the measurement of inner pressure, liquid and vapour temperatures and wall temperatures in various locations. In some cases, radiometers were also provided for the evaluation of the heat flux received by the target equipment, such as in the Townsend test. For this reason, the experimental results of the Townsend test are taken as a reference data source for the CFD Model validation. In next section, a discussion about this test will be performed.

Test ID	EXP8	EXP9	EXP10	EXP11	EXP12	EXP13	EXP14
Data source	Faucher et al. (1993)	Faucher et al. (1993)	Faucher et al. (1993)	Droste and Schoen (1988)	Landucci et al. (2009c)	Townsend et al. (1974)	Birk et al. (2006b)
Tank Specifications							
Tank geometry	Spherical	Spherical	Spherical	Hor. Cyl.	Hor. Cyl.	Hor. Cyl.	Hor. Cyl.
External diameter (m)	1.7	1.7	1.7	1.25	1.25	3.05	0.953
Total length (m)	–	–	–	4.3	2.68	18.3	3.07
Minimum wall thickness (mm)	10	10	10	6.4	5.1	15.9	7.4
Type of material	LCS*	LCS*	LCS*	STE-36 LCS*	P355NH LCS*	TC-128 LCS*	SA455 LCS*
Stored substance	Propane	Propane	Propane	Propane	LPG grade A	Propane	Propane
Tested filling level (%)	20	20	20	20	50	84	71,78
Pressure Relief Device Data							
Set pressure (MPag)	1.6	1.6	1.6	1.46	1.46	1.86	2.63
Pressure relief device nominal diameter (mm)	–	–	–	32	32	80	15
Number	1	1	1	1	1	1	1
Insulating Coating Properties							
Coating type	Intumescent	Mineral cement	Mineral cement	Rock wool	Intumescent	Polyurethane	Ceramic fibers
Applied thickness (mm)	10	38	35	100 [†]	10	3.2	13 [‡]
External Heat Source							
Type of source	Butane burners	Butane burners	Butane burners	Fuel oil pool fire	Diesel pool fire	JP-4 pool fire	Butane burners
Ambient temperature (°C)	29	20	22	25	12	6	11–21
Exposure mode	Full engulfment	Full engulfment	Full engulfment	Surrounding fire	Full engulfment	Full engulfment	Partial engulfment
Flame temperature (°C)	1200	1200	1200	–	700–1300	650–990	815–927
Measured heat flux (kW/m ²)	–	–	–	–	–	123–138	–
<small>*LCS, low-carbon steel. [†]Coating was encapsulated in a watertight steel sheet coating 1 mm thick; 30 mm air gap was left between the sheet and the coating. [‡]Coating was encapsulated in a steel jacket of 3 mm thick.</small>							

Figure 4.2: Summary of Relevant Literature Experiments un Pressurized Vessels exposed to fire in presence of Thermal Protection [6].

4.1.2. Description and results of the Townsend test

This experiment was carried out in 1974 in New Mexico (USA). On the official report [22], a lot of information about the pressure, fluid temperature, incident flux heat on the wall and liquid level are reported. The test was carried out to assess the different behavior of the vessel due to insulation layer: in the following analysis, only experimental data where the thermal insulation is absence will be used.

In the test considered, a propane tank car was exposed to a complete engulfment in a hydrocarbon (JP–4) pool fire. The tank–car complied with the DOT 112A340W specifications [59], according to the US regulation for the transportation of liquefied pressurized gases and had a nominal capacity of 125 m³. Table 4.1 shows the features of the tested tank.

ITEM	SPECIFICATION
Lenght (m)	18,410
Internal Diameter (m)	3,018
Wall Thickness (m)	0,016
Liquid Volume Fraction	0,960
PRV absolute set Pressure (MPa)	1,816
Internal medium	LPG (98% propane)
External Coating	No
Wall Material	TC-128 steel

Table 4.1: Features of DOT 112A340W tank-car.

Figure 4.3 (a&b) show respectively a real image taken before the test and a sketch of the tested tank-car [22].

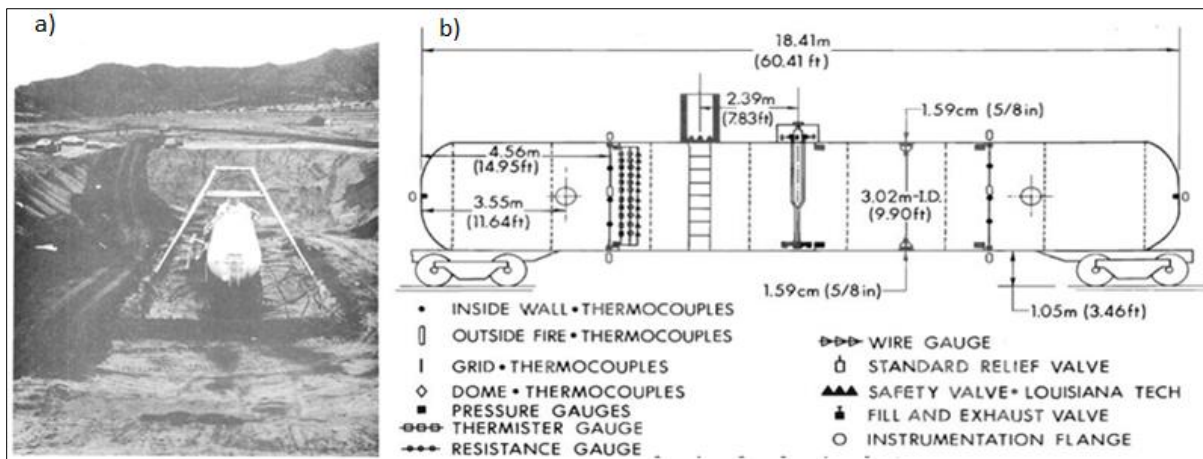


Figure 4.3: DOT 112A340W tank car: a) real image b) sketch to show the geometrica features and the positioning of instrumentation used during the test [22].

A PRV, with an opening set pressure to 1.816 MPa, was installed to protect the tanker, which was not provided with thermal insulation. In the present study, the performances of the PRV are not interesting, but an important experimental data is the first opening time: it is worth 132 seconds [22]. So as to monitor and register the tank car behaviour while heated, thermocouples, level indicator, gauges and a radiometer was equipped in order to estimate temperature, pressure, liquid level and incident flux heat on the walls.

For measuring the *temperature*, two grid of Chromel Alumel Thermocouples (precision $\pm 2.2^{\circ}\text{C}$) are placed on the interior wall of the tank shell. These grid of thermocouples were installed at 4.56 m from the hemispherical ends of the tank car in the so called *rear* and *front* cross-section, as

reported in figure 4.4 [22]. This location allows the estimation of the temperature profile of the fluid. In order to validate the CFD Model only the experimental value of temperature registered by the non questionable thermocouples are considered. Furthermore, temperature values were recorded for several point of time. They are summarized in table 4.2 [22].

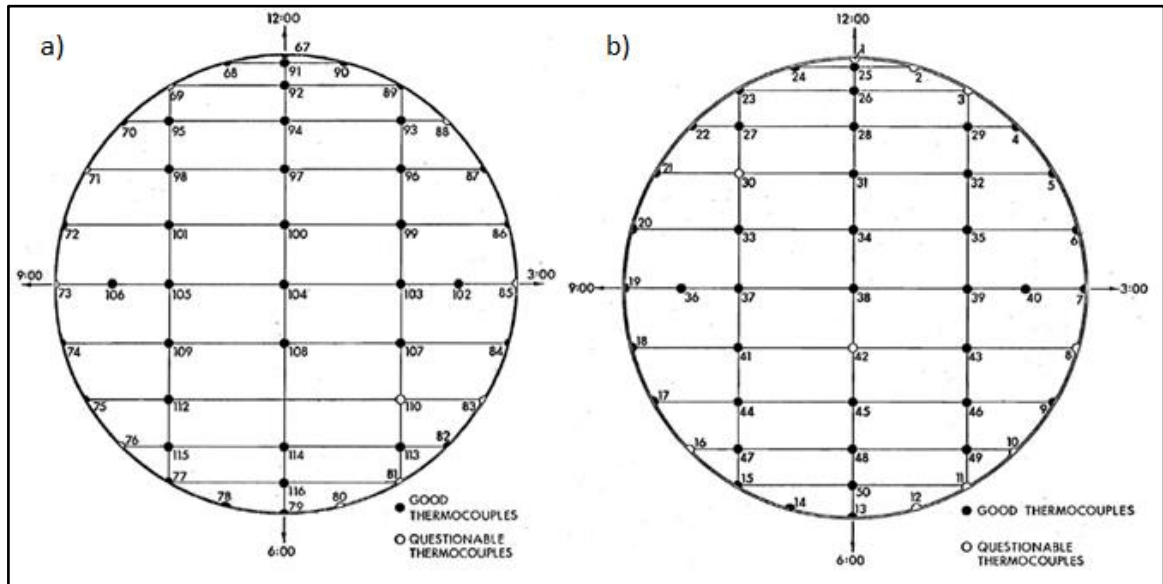


Figure 4.4: Cross-Sectional View of Thermocouple Position and their respective Item: a) Front Cross-Section; b) Rear Cross-Section [22].

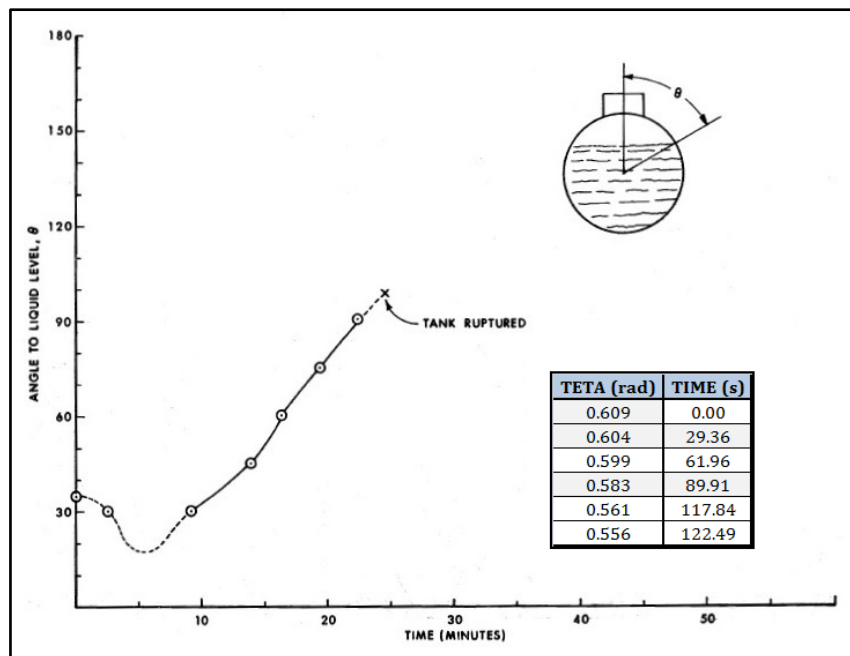


Figure 4.5: Liquid Level vs time in the Townsend' report [22].

Temperature Experimental Data vs Time					
Front Cross-Section			Rear Cross-Section		
Item	time = 71.2 sec	time = 113.5 sec	Item	time = 52.6 sec	time = 94.9 sec
92	303,93	315,76	26	295,82	308,82
93	295,37	301,82	27	294,93	300,21
94	299,15	303,37	28	295,21	301,59
95	296,04	303,87	29	294,15	299,37
96	295,43	301,82	31	294,54	299,48
97	298,59	302,65	32	294,32	300,09
98	296,15	304,04	33	294,32	298,87
99	297,43	300,59	34	294,37	298,71
100	296,37	300,43	35	294,26	297,76
101	295,82	300,2	37	293,32	296,54
103	295,59	298,37	38	294,04	297,21
104	296,98	297,7	39	294,65	296,87
105	295,98	298,7	41	293,98	297,15
107	294,43	295,26	43	294,32	296,32
108	296,76	300,03	44	294,37	296,65
109	294,32	294,04	45	294,32	295,98
112	294,59	296,7	46	294,26	295,87
113	295,76	298,26	47	294,71	295,87
114	294,54	295,65	48	294,37	294,65
115	295,42	298,32	49	294,04	295,26
116	295,32	295,54	50	294,65	296,87

Table 4.2: Temperature Experimental Data used for the CFD Model Validation [22].

For the monitoring the **liquid level** as a function of time, a thermistor gauge was constructed: it consisted of 240 thermistors positioned on a linear section. The gauge was then mounted along the vertical diameter of the tank. The principle of operation was the following: a small excitation current was applied to thermistors to cause resistive heating. Since the thermal conductivity of the liquid propane is much greater than that of gaseous propane, as each thermistor emerged from the liquid into the vapour space it would resistively heated to a significantly higher temperature. The increase of temperature is associated with the resistance change: if the resistance is known, the liquid level in time can be evaluated. Figure 4.5 shows the liquid level in function of the time [22].

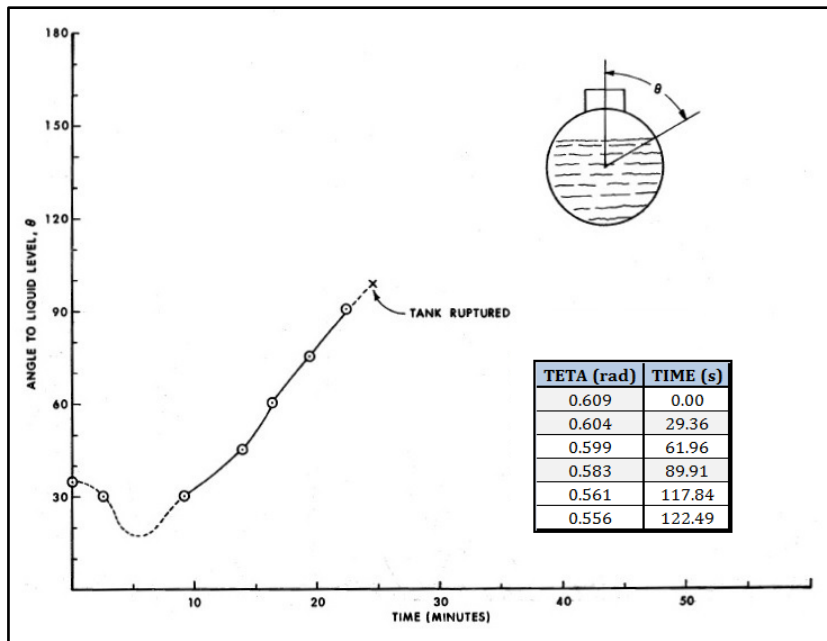


Figure 4.5: Liquid Level vs time in the Townsend' report [22].

Finally, the last important parameters to be monitored is the **fire flux heat**. For this aim, the NASA built the radiometer (range 0–1255 kW m⁻²) that monitored the incident flux heat on the walls of the tank. The results of the radiometer in function of the time is reported in figure 4.7.

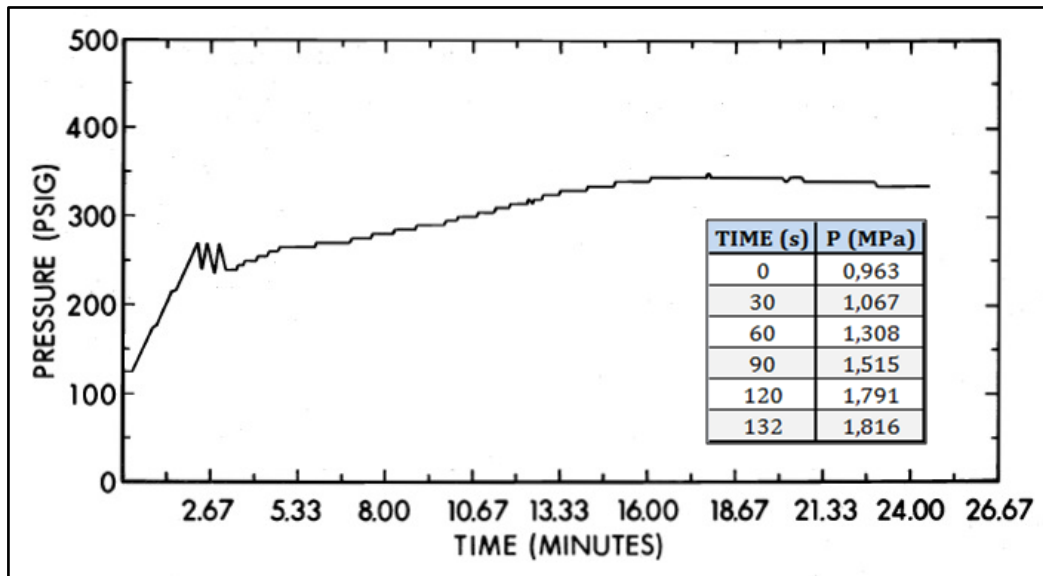


Figure 4.6: Pressure vs time in the Townsend' report [22].

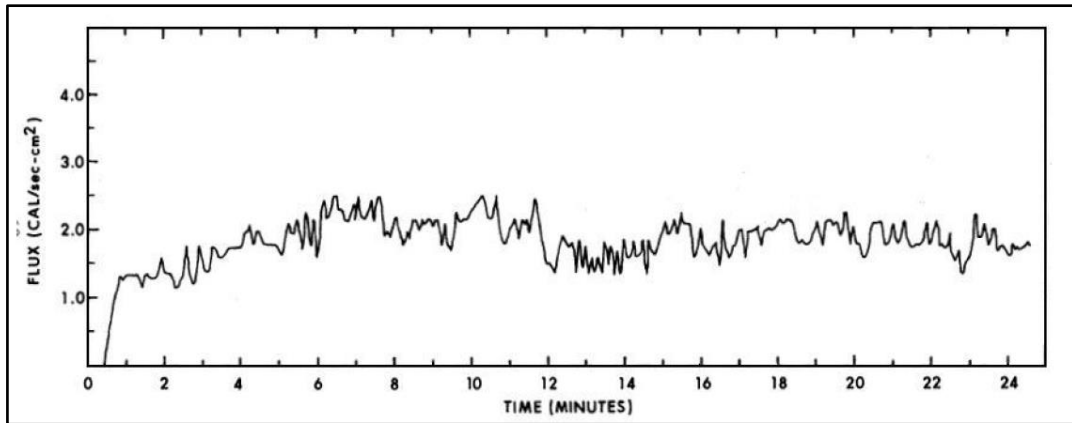


Figure 4.7: Incident flux heat on the wall of tank vs time in the Townsend' report [22].

4.2. Numerical studies

For modeling the behaviour of tank exposed to fire there are three main types of numerical approach [6]:

- Lumped Parameters Modeling Approaches;
- Simplified Correlations for Vessel Failure Prediction;
- Distributed Parameters Modeling Approaches (advanced Tools).

This section aims at the brief description of these tools.

4.2.1. Lumped Parameters Modeling Approaches

Several lumped parameter models are available in the literature for the assessment of the thermal response of both the vessel and its content when subjected to fire. In table 4.3, the main Lumped Parameter Models for the prediction of the behaviour of pressure vessels exposed to fire are reported.

These models, developed from 1970 to nowadays, are in general dedicated to the assessment of the response of horizontal cylindrical LPG vessels to engulfing fire, by predicting the wall temperature rise and internal pressure. This type of models can give reasonable predictions but it is worth noticing that for high values of wall temperature, due to the strong weakening of structural steel, advanced tools capable of more accurate predictions should be considered for more precise determination of vessel ttf [6]. Nevertheless, simplified models usually provide support to the analysis of fire protection system influence or to the PRV sizing. Only few models manage

different vessel geometries and different vessel categories (e.g. ENGULF [36]), few others are able to predict correctly the influence of the PRV action (e.g. HEAT-UP [35]).

REFERENCE	MODEL NAME	YEAR
Graves [34]		1973
Aydemir et al. [27]	PLGS-I	1988
Beynon et al.[35]	HEAT-UP	1988
Ramskill [36],[37]	ENGULF I & II	1988-1989
Birk [23]	TANKCAR	1989
Dancer et al. [38]	TAC7	1990
Shebeko et al. [39]		1995
Salzano et al. [40]		2003
Gong et al. [28]		2004
Landucci et al. [33]	RADMOD	2009
Heymes et al. [41]		2013

Table 4.3: Lumped Parameter Models for the prediction of the behavior of pressure vessels exposed to fire.

More recently, an extended model was developed in order to evaluate the ttf of insulated or unprotected vessels of any type, both atmospheric and pressurized, undergoing different modes of fire exposure, taking into account the influence of the PRV actions [33]. This model, namely **RADMOD**, is based on a thermal nodes approach that attempts to divide the equipment in several nodes with uniform properties; considering these nodes it is then possible to write a set of equations capable describe the behaviour of the relevent parameters with time (e.g pressure, temperature and conductivity average over each node). Figure 4.8 reports the schematization of tank and its division in nodes [6] for a horizontal cylindrical tank, subject of this work.

The nodes considerer, other than the liquid and the vapour ones are numbered from 1 to 8. A description of these nodes is reported in table 4.4 [30].

In order to evaluate the vessel heat-up, a series of Energy balance equations have to be implemented in the RADMOD codes. The thermal balance equations are solved in each node in order to reproduce the dynamic behaviour of the vessel. The main equations implemented in the model are discussed elsewhere [6].

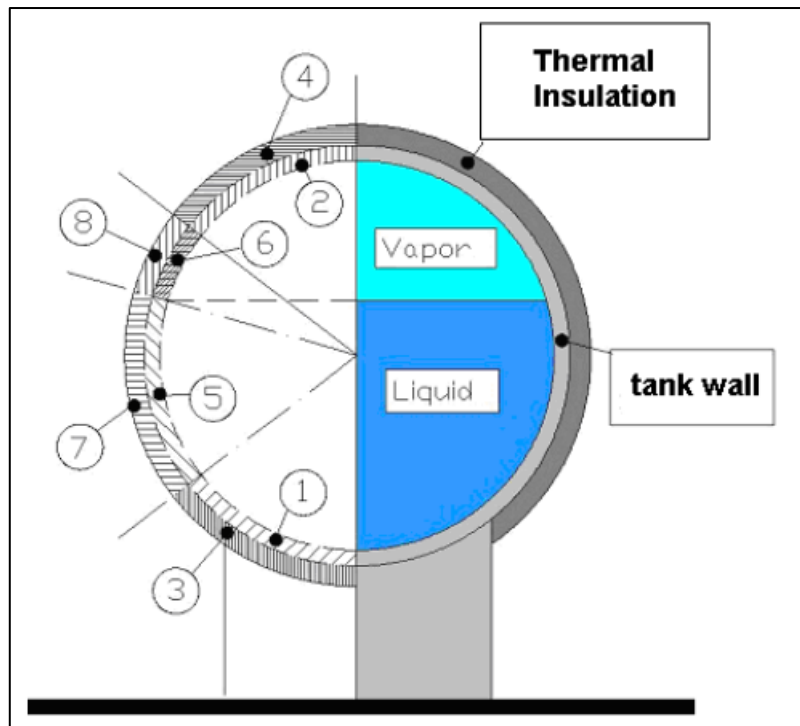


Figure 4.8: Schematization of thermal nodes for lumped parameters analysis of pressurized vessels [60].

NODE	DESCRIPTION
1	Vessel wall in contact with the liquid phase but not in the zone impinged by the flame
2	Vessel wall in contact with the vapour phase but not in the zone impinged by the flame
3	Coating at the level of the liquid phase but non in contact with the flame
4	Coating at the level of the vapour phase but non in contact with the flame
5	Vessel wall in contact with the liquid phase and in the zone impinged by the flame
6	Vessel wall in contact with the vapour phase and in the zone impinged by the flame
7	Coating at the level of the liquid phase and in contact with the flame
8	Coating at the level of the vapour phase and in contact with the flame

Table 4.4: Description for each nodes of thermal nodes schematization [6].

Boundary conditions together with global conservation laws lead to a system of equations which determines the parameters of interest, such as the temperature in each node. This allows for the calculation of temperature–time profiles as a function of the radiation mode and intensity on the vessel. The estimation of these parameters is used for the calculation of the hoop stress generated in each zone of the vessel (namely σ_{eq}) and to compare it with the maximum allowable tensile strength of the vessel materials (namely σ_{adm}).

The ttf of the vessel is the time at which the following conditions occurs at least in one of the nodes representative of the vessel wall (the nodes labelled with 1, 2, 5 and 6 in figure 4.8):

$$\sigma_{eq} = \sigma_{adm} \quad (19)$$

The main limitation of the original model is to neglect the effect of liquid thermal stratification: for this reason the model is constantly being developed. In this contest, a recent thesis work carried out by University of Bologna and TNO (Dutch Institute for the Applied Research) [60] improved the liquid temperature prediction of RADMOD model, through inserting of a stratification sub-model. Three thermal stratification sub-models were implemented: two of these are taken from literature and a third one was developed in the research work. A brief description of these sub-models is reported in the following.

Birk's stratification sub-model (2013)

Birk discussed this stratification submodel in a recent work [61]. The sub-model just splits the liquid in two nodes, one is the boundary layer and one is the bulk. In this case the boundary layer is responsible for all the heat exchange in the liquid phase so the bulk remains untouched, at constant temperature all the time. It is also considered that all the heat from the vapour phase and from the vapour side shell is heating the boundary layer only: in this way, the sub-model is more conservative. The schematization of the two nodes is shown in Figure 4.9 [60–61].

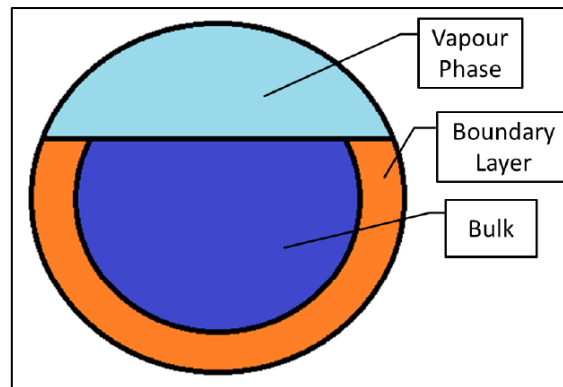


Figure 4.9: Schematization of the simplified stratification model proposed by Birk, adapted from [60–61].

The equations system is the same as in the RADMOD (without stratification sub-model) : the only difference is in the liquid mass, where instead of the whole liquid mass there is just the boundary layer part. According Birk (2013), the thickness of the boundary layer can be assumed constant and equal to 7.5% of the tank diameter. With this model, before the PRV opens it results that there is

less liquid mass to heat up; when the PRV opens it assumed the an ideal mixing of the two liquid parts occurs, hence the liquid becomes again a single zone.

Birk reports the stratification effect is relevant for a filling level higher than 50%, so that is basically a rule of thumbs if this model should be used or not. More detail on this model can be find in other source [60], [61].

Yu et al. stratification sub-model (1992)

The idea of this model is from Yu et al [30]. The liquid mass is split into three nodes with heat and mass exchange between them. There is always a boundary layer, this time by the sell wall, a stratified layer, receiving the hot liquid from the boundary layer and from the evaporation/condensation phenomenon and a bulk almost at constant temperature. The fluid nodes can be seen in figure 4.10 [30], [60].

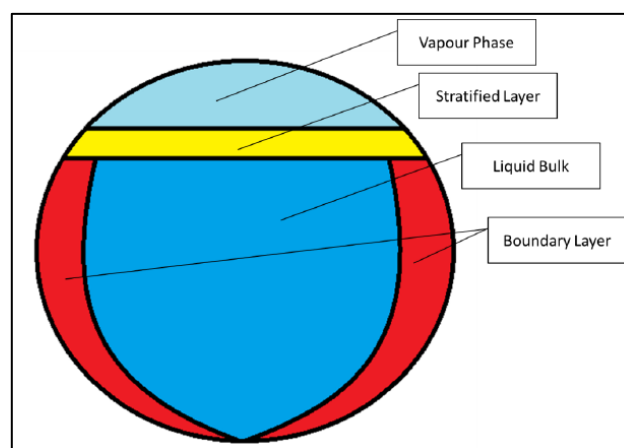


Figure 4.10: Schematization of the stratification model proposed by Yu et al., adapted from [30], [60].

At the beginning, the stratified layer is considered 0.05% of the tank diameter (it cannot be zero as with no mass the mathematical system cannot be solved). The boundary layer is considered with a uniform thickness at the start, as suggested in the previous stratification model. The bulk is evaluated as the remaining part of the liquid. The stratified layer gets bigger receiving a mass flux from the boundary layer and evaporating, it is also the liquid part interested in the heat exchange with the vapour and receiving the radiation contribute from the upper part of the shell. The boundary layer receives the big amount of heat from the shell, as its thickness changes in time there is also a small mass exchange with the bulk, slightly rising its temperature.

For this model is necessary an initial filling level higher than 30%. As with the other stratification sub-model, also this one will stop once the PRV opens, the whole liquid boiling is approximated with an instant ideal mixing of all three liquid nodes. More detail on this model can be find in other source [28], [30], [60].

Bazzocchi et al. stratification sub-model (2014)

This model was developed in a recent work by Bazzocchi, Cozzani and Landucci [60]. The approach is similar to the Birk stratification sub-Model, since it is based on simplifying assumptions that do not involve the resolution of equations of motion.

The liquid is split into two nodes: instead of considering a partial heated annulus attached to the vessel wall, an upper stratified layer, laying above the bulk phase, receives all the input heat. The schematization is reported in figure 4.11 [60].

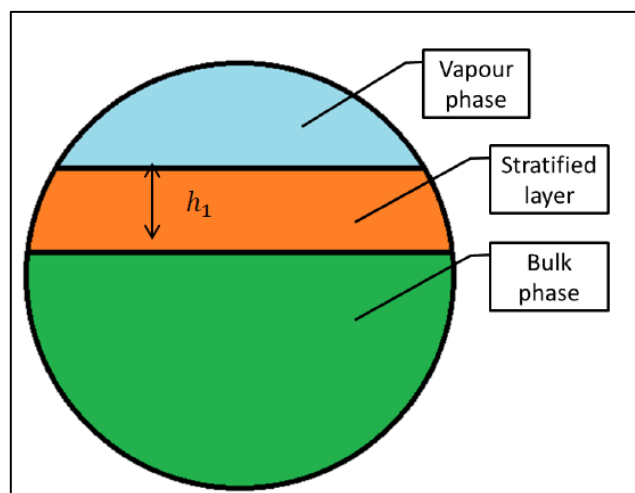


Figure 4.11: Schematization of the stratification model proposed by Bazzocchi et al., adapted from [60].

Since all the heat received by the liquid goes to the stratified layer, to solve the system of equation a novel fitting parameter has to be entered: the height of the stratified layer h_1 . This schematization of the liquid thermal stratification allows a better prediction by the RADMOD Model, since the hot liquid layer, which is positioned at the liquid-vapour interface, regulates the pressure in the tank and then the time to failure (ttf) and the PRV opening time. The correlations for the estimating of h_1 , in the previous work [60], was based on a minimum amount of experimental data available in literature. One of the objectives of the present work is to propose a simplified correlation for the assessment of height of the stratified layer h_1 as a function of the parameters in play, through

setting of several case studies on the CFD model: CFD predictions can be used as an equivalent of experimental data.

4.2.2. Simplified Correlations for Vessel Failure Prediction

Since in the risk assessment of complex industrial sites a high number of possible target of escalation triggered by fire may be identified, a very high number of simulations may be required to calculate the ttf for any exposed vessel in any possible fire outcome. Even if lumped models are characterized by a low computational time, their use may require a relevant effort in the analysis of extended industrial clusters. Moreover, the lumped parameters models, although simplified, require the definition of several input parameters for each simulation (e.g. vessel geometrical data, properties of vessel content, radiation mode, etc.).

Thus, for the risk assessment of industrial areas, a simplified approach might be preferred than the lumped approach. In particular, simplified correlations were formulated to predict the ttf (time to failure) of tank. Those correlations are expressed in the following form by Landucci et al. (2009)[33]:

$$\log_{10}(ttf) = c \cdot \log_{10}(I) + d \quad (20)$$

where I represents the radiating heat flow. The c and d constants were calculated fitting eq (20) to the results of lumped model simulations [33]. In particular c is a coefficient function of the type of vessel (atmospheric or pressurized), while d is a constant that is function of the volume and other geometrical features of the vessel (e.g., length, diameter, thickness, etc.).

This work is not focused on this aspects; the reader is referred to [6] for more details.

4.2.3. Distributed Parameters Modeling Approaches

The limits related to the lumped parameters models for assessing the response of tank exposed to external fire have growing interest in the use of distributed parameters models. These codes solve the conservation laws in a domain that can be split in many small cells, of the size and shape desired, leading to results more similar to reality than those obtained by a lumped codes: this is the main advantage. Moreover such codes are able to analyze several types of equipment (size and shape desired), also providing the input data much more detailed.

These codes are mainly of two types:

- FEM (Finite Element Modeling): these tools are used for evaluating the wall material behaviour when the tank is exposed to fire.
- CFD (Computational Fluid Dynamics): these codes model in detail the behaviour of lading fluid containing in the vessel.

Solving the governing equations, the approximations are minimal. In lumped codes some phenomena, such as liquid expansion and liquid thermal stratification, are non considered or greatly approximated.

In present work, ANSYS® FLUENT® v. 14.5 software is used for modeling the behaviour of the fluid containing in tanks exposed to fire. A detailed analysis of the developed CFD Model is shown in the chapter 6.

5. Aims of the work

In this chapter the aims of the work will be briefly described.

Once analyzed the state of the art about the modeling the behaviour of pressurized vessels exposed to fires, a CFD model was built, filling the gaps of a previously model [42]. For the validation of the CFD model, a comparison with the experimental results of a large scale test (reported in sec. 4.1.2.) was carried out.

Once validated, CFD model was applied to industrial scenarios with two different goals:

1. Performing a sensitivity analysis to get a deeper understanding of the liquid thermal stratification. This part of the work was aimed at evaluating the dependence of the altered thermally layer as a function of the main parameters, such as filling level, incident flux heat on the walls, absolute pressure and geometric parameters (mainly the diameter). This analysis serves as a support to a lumped parameters model [33], reported and explained in sec. 4.2.1. The aim is to build a parametric correlation for the estimation of the height of the stratified liquid layer to be implemented in the lumped code, in order to improve its predictions.
2. Simulating several accidental scenarios in an industrial site through the application of “advanced boundary conditions”. In particular, it is desired to simulate the effect that, a primary fire scenario (a pool fire of a hydrocarbon released from an atmospheric tank) has on a neighbouring pressurized LPG vessel. Since the LPG vessel is not engulfed in a pool fire, it is necessary to build a subroutine for the application of advanced boundary conditions in the CFD Model. This allows implementing a given amount of flux heat for each point of the tank wall, according to the exposure of the vessel to the pool fire. For the determination of incident flux heat on the tank walls containing LPG, the use of a simplified fire model is necessary. In addition, DNV® Phast® software is used to validate the integral fire model predictions.

The following flow chart (fig. 5.1) shows the methodology used for the achievement of these aims and their interaction.

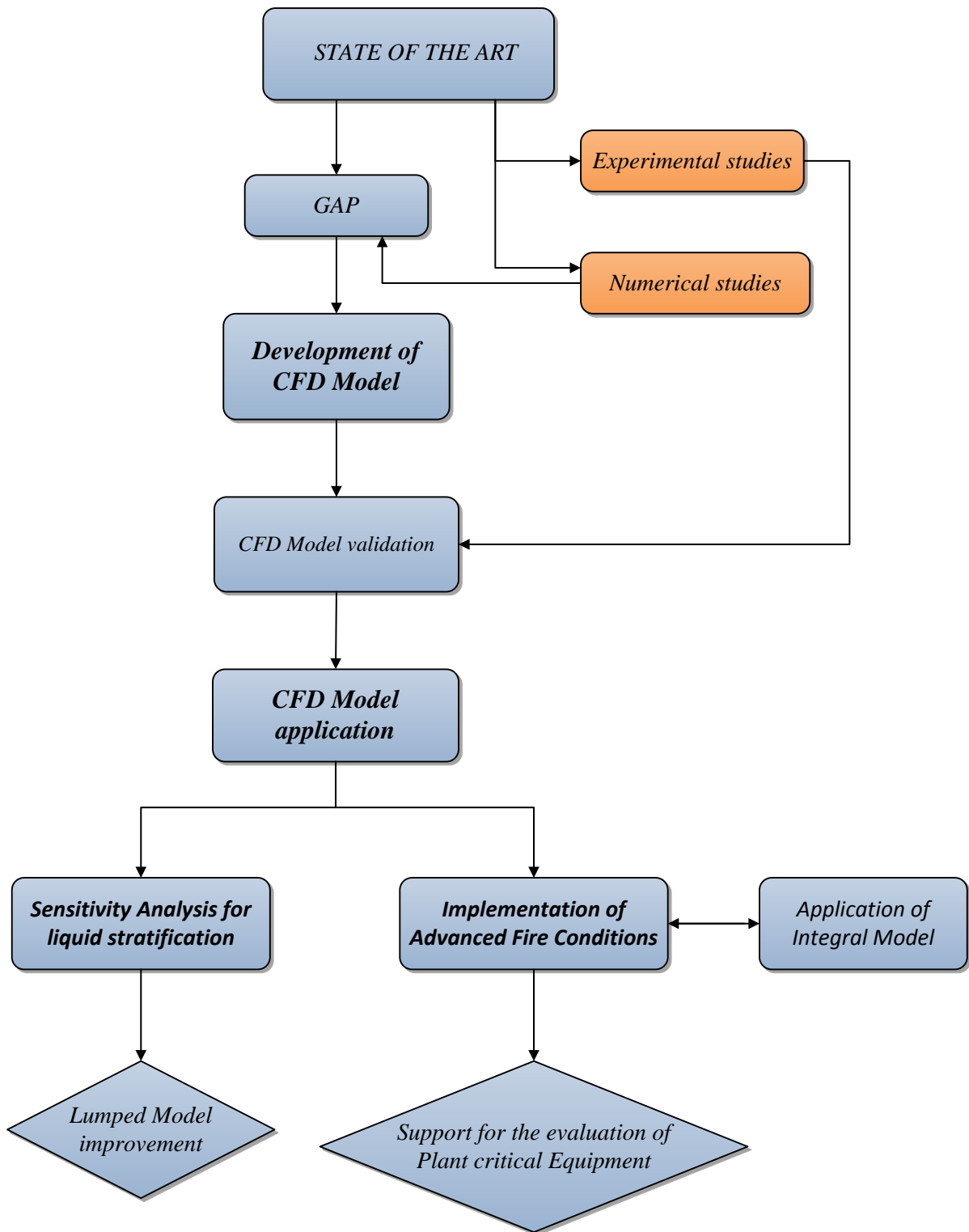


Figure 5.1: Flow chart describing the methodology used in the present work.

6. Description of the CFD model

In this chapter the CFD model developed to predict the behaviour of pressurized vessels exposed to fire will be argued. Theoretical aspects and numerical implementation will be explored.

6.1. Theoretical aspects of the CFD model

6.1.1. CFD Modeling Overview

To simulate the behaviour of the stored fluid while the vessel is heated by a fire ANSYS® FLUENT® v.14.5 software is used. As the other commercial CFD software, this code allows to simulate a wide range of fluid dynamics problems.

A CFD code solves the governing equations needed to describe the physical model. For the resolution through a computer, the discretization and solution methods are required. Flows and related phenomena can be described by partial-differential (or integro-differential) equations which cannot be solved analytically. The discretization method approximates the differential equations in a system of algebraic equation, which can then be solved on a computer. The approximations are applied to small domains in space and/or time so the numerical solution provides results at discrete locations in space and time. There are three discretization approaches that a CFD code can use [43]:

1. *Finite Difference Method (FDM)*: this is the oldest methods for numerical solution of partial differential equations, believed to have been introduced by Euler in the 18th century. It is also the easiest method to use for simple geometries. The starting point is the conservation equation in differential form. The solution domain is covered by a grid. At each grid point, the differential equation is approximated by replacing the partial derivatives by approximations in terms of the nodal values of the functions. The result is an algebraic equation per grid node, in which the variable value at that and a certain number of neighbor nodes appear as unknowns. Taylor series expansion or polynomial fitting is used to obtain approximations to the first and second derivatives of the variables with respect to the coordinates. When necessary, these methods are also used to obtain variable values at locations other than grid nodes (interpolation). This method is very simple and effective for structured grids. The disadvantage of FDM is that the conservation

is not enforced unless special care is taken. Also, the restriction to simple geometries is a significant disadvantage in complex flows [43].

2. *Finite Volume Method (FVM)*: this uses the integral form of the conservation equations as its starting point. The solution domain is subdivided into a finite number of contiguous control volumes (CVs). At the centroid of each CV lies a computational node at which the variable values are to be calculated. Interpolation method is used to express variable values at the CV surface in terms of the nodal (CV-center). Surface and volume integrals are approximated using suitable quadrature formulae. As a result, one obtains an algebraic equation for each CV, in which a number of neighbor nodal values appear.

The FVM can accommodate any type of grid, so it is suitable for complex geometries. Moreover, this method is conservative by construction, so long as surface integrals (which represent convective and diffusive fluxes) are the same for the CVs sharing the boundary. The disadvantage is that methods of order higher than second are more difficult to develop in 3D. This is due to the fact that the FVM requires three levels of approximation: interpolation, differentiation and integration (for more details, see source [43]).

3. *Finite Element Method (FEM)*: it is similar to the FVM in many ways. The domain is broken into a set of discrete volumes of finite element that are generally unstructured: in 2D, they are triangles or quadrilaterals, while in 3D tetrahedra are most often used. The distinguishing feature of FEM is that the equations are multiplied by a “weight function” before they are integrated over the entire domain. The main advantage is that it can deal any type of geometries. The disadvantage is that the algebraic matrix is not as well structured as those for regular grid, making it more difficult to find efficient solution methods.

ANSYS® FLUENT® support the Finite Volume Method (FVM), so the numerical algorithm realized by the CFD software consists in the following steps:

1. Reading of mesh, built with the software ICEM CFD® by package ANSYS® v. 14.5. The mesh represents the subdivision of the geometry of the physical model in a number of CVs.
2. Integration of the governing equations that describe the physical model over all the CVs of the domain.
3. Discretization and conversion of the resulting integral equations into a system of algebraic equations through interpolation and approximation methods. The approximation methods are used to approximate volume and surface integral (e.g. Midpoint rule, Simpson’s-rule, etc.); the interpolation methods are used to express the variable values on the face of each

CV as a function of variable values in the centre of its (Upwind Interpolation, QUICK Interpolation, etc.).

4. Implementation of boundary conditions and initial conditions.
5. Solution of the algebraic matrix by an iterative method (SIMPLE, PISO, etc.).

The conservation of a general fluid flow variable (ϕ), being scalar or vectorial, within a CV can be expressed as a balance between the various processes tending to increase or decrease it in each finite CV. The general form of conservation law that the FVM solves, considering the general property (ϕ), is reported in figure 6.1:

$\frac{\partial}{\partial t} \left(\int_{CV} \rho \phi dV \right) + \int_A \mathbf{n} \cdot (\rho \phi \mathbf{u}) dA = \int_A \mathbf{n} \cdot (\Gamma \text{grad} \phi) dA + \int_{CV} S_\phi dV$			
<div style="border: 1px solid black; padding: 5px; margin-bottom: 5px;"> Rate of change of the total amount of fluid property ϕ in the CV. </div>	<div style="border: 1px solid black; padding: 5px; margin-bottom: 5px;"> Net rate of decrease of fluid property ϕ of the fluid element due to convection. </div>	<div style="border: 1px solid black; padding: 5px; margin-bottom: 5px;"> Net rate of increase of fluid property ϕ of the fluid element due to diffusion. </div>	<div style="border: 1px solid black; padding: 5px;"> Net rate of increase of fluid property ϕ as result of sources. </div>

Figure 6.1: Integral form of conservation law for a general property ϕ (adapted from Ref [43]).

6.1.2. CFD implementation of the relevant physical phenomena

The physical phenomena related to the heating of the fluid during exposure to fire have to be predicted by the CFD code through the use of models: these are necessary to implement and solve the conservation laws. Figure 6.2 shows the main transport phenomena.

Consequently, the representative governing equations of fluid flow in the domain of interest are:

1. Continuity equation;
2. Momentum equation;
3. Energy equation;
4. Radiative heat transfer equation (RTE).

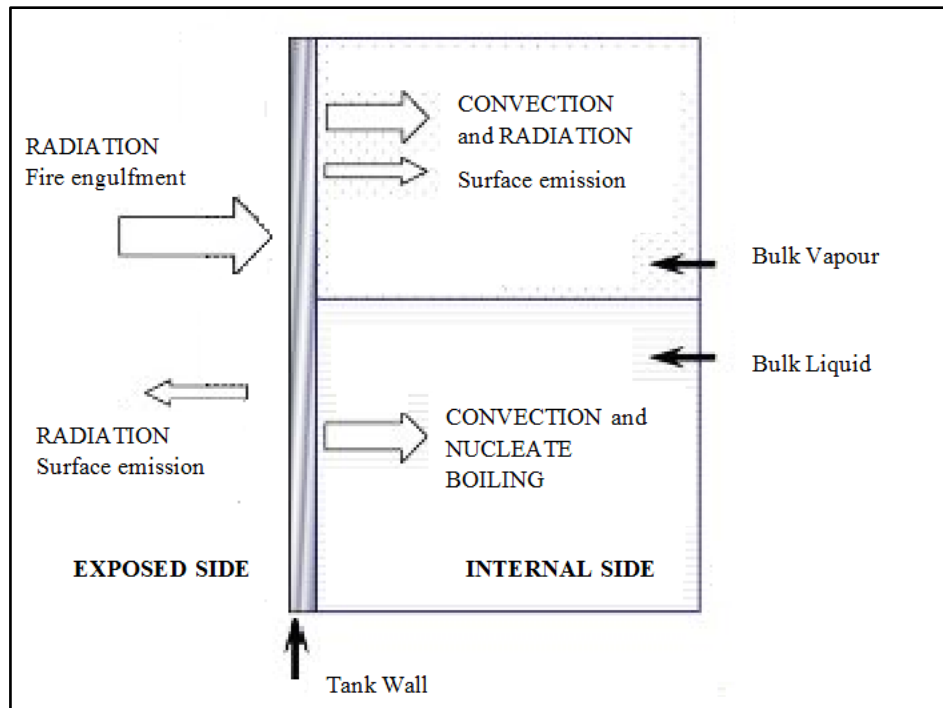


Figure 6.2: Graphic explanation of the main transport phenomena involved (adapted by [44]).

Continuity Equation and Multiphase Model

Considering that the domain is constituted by two phases, the first model to be implemented in the CFD code is a multiphase model. Due to the presence of two continuous phases separated by an interface, an Euler-Euler (E/E) approach is followed in the present work.

In the Eulerian methods, the different phases are treated mathematically as interpenetrating continua. Since the volume of a phase cannot be occupied by the other phases, the concept of phasic volume fraction (α_i) is introduced. These volume fractions are assumed to be continuous function of space and their sum is equal to one [44].

In ANSYS® FLUENT® v. 14.5, multiphase model that is capable to track in steady or in transient state any gas–liquid interface is the Volume of Fluid (VOF). Developed in 1981 by Hirt and Nichols [45], the VOF is applicable to a fixed Eulerian mesh. For each phase, in each cell of the mesh, the VOF identifies the volume fraction value. Indicating with L and V the liquid and vapour phase respectively, one of the following condition is possible for each CV [44]:

- $\alpha_L = 0$ the cell is completely full of vapour;
- $\alpha_L = 1$ the cell is completely full of liquid;
- $0 < \alpha_L < 1$ the cell contains the interface liquid–vapour.

Solving the continuity equation for VOF, in each cell is known the phasic volume fraction. The fields for all variables and properties are shared by the phases and represent averaged values. Several properties are calculated through a volume fraction–averaged while others are calculated through a mass fraction–averaged.

The volume fraction–averaged properties are [44]:

$$\rho = \alpha_L \rho_L + (1 - \alpha_L) \rho_V \quad (21)$$

$$\mu = \alpha_L \mu_L + (1 - \alpha_L) \mu_V \quad (22)$$

$$k = \alpha_L k_L + (1 - \alpha_L) k_V \quad (23)$$

$$\mathbf{v} = \alpha_L \mathbf{v}_L + (1 - \alpha_L) \mathbf{v}_V \quad (24)$$

while the mass fraction–averaged properties are:

$$T = \frac{\alpha_L \rho_L T_L + (1 - \alpha_L) \rho_V T_V}{\alpha_L \rho_L + (1 - \alpha_L) \rho_V} \quad (25)$$

$$E = \frac{\alpha_L \rho_L E_L + (1 - \alpha_L) \rho_V E_V}{\alpha_L \rho_L + (1 - \alpha_L) \rho_V} \quad (26)$$

$$c_P = \frac{\alpha_L \rho_L c_{P_L} + (1 - \alpha_L) \rho_V c_{P_V}}{\alpha_L \rho_L + (1 - \alpha_L) \rho_V} \quad (27)$$

where the energy of each phase is based on the specific heat of that phase and the shared temperature.

The tracking of the interface between the phases is accomplished by the solution of a “Volume Fraction Continuity Equation” for each phase except for the primary phase. In this case, setting the vapour phase as a primary phase, the Volume Fraction Continuity Equation is solve only for the secondary phase, or rather the liquid phase. All other equations (momentum, energy, radiation) are shared by the phases. For a correct solution, it is important that near to the interface the mesh is very fine otherwise the convergence problems can be found.

For the liquid phase, the Volume Fraction Continuity Equation solved by FLUENT® is [44]:

$$\frac{1}{\rho_L} \left[\frac{\partial}{\partial t} (\alpha_L \rho_L) + \nabla \cdot (\alpha_L \rho_L \mathbf{v}_L) \right] = S_{\alpha_L} + (\dot{m}_{VL} - \dot{m}_{LV}) \quad (28)$$

while for the vapour phase, the volume fraction in each cell is computed following the mathematical constraint:

$$\sum_{\text{on each cell mesh}} (\alpha_L + \alpha_V) = 1 \quad (29)$$

Analyzing the above equation (28), it is possible to assess the meaning of each term:

- $\frac{\partial}{\partial t}(\alpha_L \rho_L)$: rate of increase of liquid mass per unit volume;
- $\nabla \cdot (\alpha_L \rho_L \mathbf{v}_L)$: net rate of liquid mass addition per unit volume due to convection;
- S_{α_L} : rate of increase of liquid volume fraction due to external liquid mass source term;
- $\dot{m}_{VL} - \dot{m}_{LV}$: rate of increase of liquid mass due to the difference between the mass transfer from vapour to liquid phase minus the mass transfer from liquid to vapour phase.

All above terms dimensionally correspond to a mass per unit volume per unit time ($\text{kg m}^{-2} \text{s}^{-1}$).

By default the value of the mass source term is zero, but it is possible to change this value through a User Defined Function (UDF), so as to improve the standard mass transfer model available in ANSYS® FLUENT® v. 14.5. A User Define mass source term for each phase must be followed by a user define momentum and energy source term depending on the physical effects of the mass source term on the system.

In the physical model to simulate, it is necessary to focus about two phenomena, that by default the VOF model does not consider. These are:

1. *Heterogeneous nucleation*: in the region near to the hot wall, it is possible that the fluid temperature is higher than the interface temperature (saturation temperature to the storage pressure). If this situation occurs, the formation of vapour bubbles takes place.
2. *Homogeneous nucleation*: evaporation phenomenon can occur at the vapour–liquid interface.

To simulate in detail the evaporation–condensation phenomenon, which is critical for the assessment of the present two–phase system, a specific UDF, developed in a previous work [42], was implemented in a CFD Model. This subroutine is available in version of ANSYS® FLUENT® subsequent to it (v. 14.5.): it is called “Lee Model” [46].

In this work, we are not interested in studying the evaporation/condensation process inside the engulfed vessel while heated up by the fire, but in the correct representation of its thermal behaviour so it is necessary to consider the enhancement of the liquid phase heat transfer due to its heterogeneous nucleation near the wall. According with the previous work [42], it is possible to neglect the momentum exchange between surface condensation and evaporation that leads the interface between liquid and vapor to exist: it is feasible because the gravity field is much more important than the surface tension field so that it can be neglected in the momentum equation. For this reason, the subroutine contain the define mass source term for each phase and the define energy source term.

The UDF calculates the mass transfer and the related energy transfer due to evaporation/condensation process using the kinetic gas theory, the Hertz–Knudsen equation [47]:

$$J = \beta_c \sqrt{\frac{M_W}{2\pi R}} \left(\frac{P}{\sqrt{T_V}} - \frac{P^0}{\sqrt{T_L}} \right) \quad (30)$$

where J is net mass flux over the vapour–liquid interface ($\text{kg m}^{-2} \text{s}^{-1}$), T_V and T_L are respectively the vapour and liquid temperature, while β_c is the accomodation condensation coefficient, representing the ratio between the experimentally observed condensation velocity and the maximal theoretical condensation velocity. The same consideration is valid about the evaporation accomodation coefficient β_E .

Under saturation conditions, saturated pressure and temperature are linked by Clausius–Clapeyron equation [48]:

$$(P - P^0) = - \frac{\lambda^0}{T \left(\frac{1}{\rho_V} - \frac{1}{\rho_L} \right)} (T - T^0) \quad (31)$$

substitution of Eq. 31 in Eq. 30 results in:

$$J = \beta_c \sqrt{\frac{M_W}{2\pi R T^0}} \frac{\lambda^0}{\left(\frac{1}{\rho_V} - \frac{1}{\rho_L} \right)} \frac{(T^0 - T)}{T^0} \quad (32)$$

so as to obtain the mass source connected to the condensation (or evaporation) process it is necessary to multiple J for the volumetric interfacial surface area a (a_L and a_V for liquid and vapour phase). The volumetric interfacial surface area can be expressed as a function of the mean Sauter

diameter (D_{MS}) and the volume fraction (α_i) of the phase under consideration, assuming spherical bubbles [49]:

$$a_L = \frac{6\alpha_L}{D_{SM}} \quad \& \quad a_V = \frac{6\alpha_V}{D_{SM}} \quad (33)$$

Hence, the mass source terms due to condensation and evaporation, respectively X_{CL} and X_{EV} are expressed combining Eqs. 32 and 33:

$$\begin{aligned} \text{condensation} \quad X_{CL} &= \left[\beta_C \frac{6}{D_{MS}} \sqrt{\frac{M_W}{2\pi RT^0}} \frac{\lambda^0 \rho_L}{(\rho_L - \rho_V)} \right] \rho_V \alpha_V \frac{(T^0 - T)}{T^0} \\ &= \beta'_C \rho_V \alpha_V \frac{(T^0 - T)}{T^0} \end{aligned} \quad (34a)$$

$$\begin{aligned} \text{evaporation} \quad X_{EV} &= \left[\beta_E \frac{6}{D_{MS}} \sqrt{\frac{M_W}{2\pi RT^0}} \frac{\lambda^0 \rho_V}{(\rho_L - \rho_V)} \right] \rho_L \alpha_L \frac{(T^0 - T)}{T^0} \\ &= \beta'_E \rho_L \alpha_L \frac{(T^0 - T)}{T^0} \end{aligned} \quad (34b)$$

The terms β'_C e β'_E are the mass transfer time relaxation parameters and represent the rate of condensation and evaporation. According to the work of Wu et al. [50], the value of these parameters may be set equal to 0.1.

Considering that the condensation process decreases the amount of the vapor phase while the evaporation process increases it, and considering positive an incoming mass transfer rate, the mass source terms expressions in the UDF are:

1. for condensation, occuring at $T_V < T^0$

$$\text{source term increasing liquid phase mass} \quad M_{CL} = 0.1 \rho_V \alpha_V \left| \frac{T_V - T^0}{T^0} \right| \quad (35a)$$

$$\text{source term decreasing vapour phase mass} \quad M_{CV} = -M_{CL} = -0.1 \rho_V \alpha_V \left| \frac{T_V - T^0}{T^0} \right| \quad (35b)$$

2. for evaporation, occuring at $T_L > T^0$

$$\text{source term decreasing liquid phase mass} \quad M_{EL} = -0.1\rho_L\alpha_L \left| \frac{T_L - T^0}{T^0} \right| \quad (36a)$$

$$\text{source term increasing vapour phase mass} \quad M_{EV} = -M_{EL} = 0.1\rho_L\alpha_L \left| \frac{T_L - T^0}{T^0} \right| \quad (36b)$$

Therefore, implementing Eqs. 35 and 36 in the continuity equation allows quantifying the correct interphase mass source term for both the liquid and vapour phase.

Finally, the Volume Fraction Continuity Equation solved for the liquid phase has the following shape:

$$\frac{1}{\rho_L} \left[\frac{\partial}{\partial t} (\alpha_L \rho_L) + \nabla \cdot (\alpha_L \rho_L \mathbf{v}_L) \right] = (M_{CL} - M_{EL}) \quad (37)$$

Momentum Equation and Turbulence Model

A single momentum equation is solved for each spatial coordinate (x,y,z) and the resulting velocity field is dependent on the fraction of all phases through the properties ρ and μ . The momentum equation (Navier–Stokes) is [44]:

$$\frac{\partial}{\partial t} (\rho \mathbf{v}) + \nabla \cdot [(\rho \mathbf{v} \mathbf{v})] = -\nabla P + \nabla \cdot \left[\mu (\nabla \mathbf{v} + \nabla \mathbf{v}^T) - \frac{2}{3} \nabla \cdot (\mathbf{v} \bar{\mathbf{I}}) \right] + (\rho - \rho_0) \mathbf{g} + \mathbf{F} \quad (38)$$

Analyzing the above equation (38), it is possible to assess the meaning of each term:

- $\frac{\partial}{\partial t} (\rho \mathbf{v})$: rate of increase of momentum per unit volume;
- $\nabla \cdot [(\rho \mathbf{v} \mathbf{v})]$: net rate of momentum addition per unit volume due to the convection;
- $-\nabla P + \nabla \cdot \left[\mu (\nabla \mathbf{v} + \nabla \mathbf{v}^T) - \frac{2}{3} \nabla \cdot (\mathbf{v} \bar{\mathbf{I}}) \right]$: net rate of momentum addition per unit volume due to the molecular transport (viscous stresses);
- $(\rho - \rho_0) \mathbf{g}$: rate of increase of momentum due to gravity body force;
- \mathbf{F} : rate of increase of momentum due to external volumetric forces.

Actually no momentum exchange between the liquid and the vapour phase due to surface tension is considered because it is less important than the gravitational body force: last one is the promoter of the thermal stratification. To understand that the system is independent by surface tension effect it is necessary to introduce the dimensionless Eotvos number (Eo) [51]:

$$Eo = \frac{\Delta\rho \cdot \mathbf{g}(l_{scale})^2}{\bar{\sigma}} \quad (39)$$

where $\Delta\rho$ is the density difference among the two phases. Assuming, as length scale, both the global length of the interface and the length of a single cell at the interface, the Eotvos number is greatly major than 1, so surface tension can be neglected and the interface between liquid and vapour can be considered waveless.

The momentum equation above reported (38) is valid in laminar flow regime. For natural convection problem, like the one we are analyzing in the present work, the assessment of flow regime is carried out through the Rayleigh number (see section 3.3 eq. 11). The transition between laminar and turbulence flow regime occurs for values in the range 10^8 – 10^{10} .

Due to transient nature of this modeling, probably the regime transition will occur. A previous study by Hiroharu et al. [52] has shown that it occurs very quickly for vertical walls exposed to fire: for this reason in the present CFD Model is used a turbulence model.

In case of turbulent flow each variable is made up by the sum of two components: the time averaged component and the fluctuating component [43],[44]. Considering the generic property φ :

$$\varphi(t) = \bar{\varphi} + \tilde{\varphi}(t) \quad (40)$$

where

$$\bar{\varphi} = \frac{1}{\Delta t} \int_0^{\Delta t} \varphi(t) dt \quad (41)$$

By definition, the time average of the fluctuating term is 0.

$$\bar{\tilde{\varphi}} = \frac{1}{\Delta t} \int_0^{\Delta t} \tilde{\varphi}(t) dt = 0 \quad (42)$$

Substituting the Eq. (40) in the Navier–Stokes for laminar flow regime (Eq. (38)), and taking the time average, the momentum equation becomes:

$$\begin{aligned} \frac{\partial}{\partial t} [\overline{\rho(\bar{\mathbf{v}} + \tilde{\mathbf{v}})}] + \nabla \cdot [\overline{\rho(\bar{\mathbf{v}} + \tilde{\mathbf{v}})(\bar{\mathbf{v}} + \tilde{\mathbf{v}})}] \\ = -\nabla P + \nabla \cdot \left\{ \mu [\overline{\nabla(\bar{\mathbf{v}} + \tilde{\mathbf{v}}) + \nabla(\bar{\mathbf{v}} + \tilde{\mathbf{v}})^T}] - \frac{2}{3} \nabla \cdot [(\bar{\mathbf{v}} + \tilde{\mathbf{v}})\bar{\mathbf{I}}] \right\} + (\rho - \rho_0)\mathbf{g} + \mathbf{F} \end{aligned} \quad (43)$$

The velocity has three vectorial component (respectively x, y and z). it is necessary to divide each component in averaged and fluctuating term, as follows:

$$\mathbf{v} = (u, v, w) \quad (44)$$

$$u(t) = \bar{u} + \tilde{u}(t) = U + \tilde{u}(t) \quad (45)$$

$$v(t) = \bar{v} + \tilde{v}(t) = V + \tilde{v}(t) \quad (46)$$

$$w(t) = \bar{w} + \tilde{w}(t) = W + \tilde{w}(t) \quad (47)$$

Consequently it is possible to write three momentum equations for each spatial component. These are reported in the following equations:

$$\begin{aligned} x) \quad & \frac{\partial}{\partial t} \rho U + \nabla \cdot (\rho U \bar{\mathbf{v}}) \\ & = -\frac{\partial P}{\partial x} + \nabla \cdot (\mu \nabla U) + \left[\frac{\partial(-\rho \bar{u}^2)}{\partial x} + \frac{\partial(-\rho \bar{u} \bar{v})}{\partial y} + \frac{\partial(-\rho \bar{u} \bar{w})}{\partial z} \right] + \mathbf{F}_x \end{aligned} \quad (48a)$$

$$\begin{aligned} y) \quad & \frac{\partial}{\partial t} \rho V + \nabla \cdot (\rho V \bar{\mathbf{v}}) \\ & = -\frac{\partial P}{\partial y} + \nabla \cdot (\mu \nabla V) + \left[\frac{\partial(-\rho \bar{u} \bar{v})}{\partial x} + \frac{\partial(-\rho \bar{v}^2)}{\partial y} + \frac{\partial(-\rho \bar{v} \bar{w})}{\partial z} \right] + \mathbf{F}_y \end{aligned} \quad (48b)$$

$$\begin{aligned} z) \quad & \frac{\partial}{\partial t} \rho W + \nabla \cdot (\rho W \bar{\mathbf{v}}) \\ & = -\frac{\partial P}{\partial z} + \nabla \cdot (\mu \nabla W) + \left[\frac{\partial(-\rho \bar{u} \bar{w})}{\partial x} + \frac{\partial(-\rho \bar{v} \bar{w})}{\partial y} + \frac{\partial(-\rho \bar{w}^2)}{\partial z} \right] + (\rho - \rho_0)g + \mathbf{F}_z \end{aligned} \quad (48c)$$

In Eqs. 48, it is possible to see the presence of new terms due to the fluctuating component of velocity: these terms are called “Reynolds Stresses”. This equation set with the turbulent quantities is called “Reynolds–Averaged–Navier–Stokes (RANS)” equations.

The RANS introduce six new unknown terms and then the problem is not mathematically closed: for this reason is necessary to use of turbulence model for the assessment of Reynolds stresses.

The turbulence model available to predict the Reynolds stresses are divided in two categories:

- “Eddy Viscosity Models” or “Eddy Diffusivity Models”;
- Direct Models.

The “Eddy viscosity Models are widely used and they are based on the “Boussinesq Hypothesis”, or rather on the hypothesis of the isotropic turbulent. In this way, the Reynolds stresses are calculated as the viscous stresses, through a parameter called “turbulent viscosity” μ_t .

In general, the Reynolds stresses are defined as:

$$\tau_{ij} = (-\rho \overline{\tilde{u}_i \tilde{u}_j}) = \mu_t \left(\frac{\partial U_i}{\partial x_j} + \frac{\partial U_j}{\partial x_i} \right) - \frac{2}{3} \rho k \delta_{ij} \text{ with } \delta_{ij} = 1 \text{ if } i = j \text{ \& } \delta_{ij} = 0 \text{ if } i \neq j \quad (49)$$

doing some practical examples:

$$\tau_{xy} = (-\rho \overline{\tilde{u} \tilde{v}}) = \mu_t \left(\frac{\partial U}{\partial y} + \frac{\partial V}{\partial x} \right) \quad \& \quad \tau_{xx} = (-\rho \overline{\tilde{u} \tilde{u}}) = \mu_t \left(2 \frac{\partial U}{\partial x} \right) - \frac{2}{3} \rho k \quad (50)$$

consequently it is necessary to determinate the only remaining unknow variable, the turbulent viscosity μ_t .

There are three type of models that applying this solution method [43]:

- mixing Lenght Model;
- K- ϵ Model;
- K- ω Model.

In the present numerical simulation the K- ϵ Model was chosen to closed the problem: it is the turbulent model used for a wide range of turbulent flows due its robustness, economy and accuracy.

It relates the turbulent viscosity with two parameters: the turbulence kinetic energy K and its dissipation rate ϵ .

The kinetic energy (instantaneous) can be written as the sum of average kinetic energy an turbulence kinetic energy:

$$k(t)(inst. kin. ener.) = \bar{K}(aver. kin. ener.) + K(turb. kin. ener.) \quad (51)$$

$$\bar{K} = \frac{1}{2} (U^2 + V^2 + W^2) \quad (52)$$

$$K = \frac{1}{2} (\overline{\tilde{u}^2} + \overline{\tilde{v}^2} + \overline{\tilde{w}^2}) \quad (53)$$

The dissipation rate of the turbulence kinetic energy is defined so:

$$\varepsilon = \frac{K}{\tau} = \frac{K}{l_{car}/v_{car}} \quad (54)$$

The CFD Model has to solve two additional equations: these are the transport equations for the turbulence kinetic energy and its dissipation rate respectively, reported following [44]:

$$\frac{\partial}{\partial t}(\rho K) + \nabla \cdot [(\rho K \bar{\mathbf{v}})] = \nabla \cdot \left[\left(\mu + \frac{\mu_t}{\sigma_k} \right) \nabla K \right] + (G_k + G_b - Y_M) - \rho \varepsilon + S_K \quad (55)$$

$$\frac{\partial}{\partial t}(\rho \varepsilon) + \nabla \cdot [(\rho \varepsilon \bar{\mathbf{v}})] = \nabla \cdot \left[\left(\mu + \frac{\mu_t}{\sigma_\varepsilon} \right) \nabla \varepsilon \right] + C_{1\varepsilon} \frac{\varepsilon}{K} (G_k + G_b) - C_{2\varepsilon} \rho \frac{\varepsilon^2}{K} + S_\varepsilon \quad (56)$$

in words in the equation (55) and (56) the rate of change of K (or ε) plus the transport of K (or ε) by convection is equal to the sum of transport of K (or ε) by diffusion, the rate of production of K (or ε), the rate of destruction of K (or ε) and finally their source term. In these equations:

- G_k represents the generation of turbulence kinetic energy due to the mean velocity gradients; calculated as follows:

$$G_k = (-\rho \overline{\tilde{u}_i \tilde{u}_j}) \frac{\partial U_j}{\partial x_i} = 2\mu_t E_{ij} E_{ij} \quad (57)$$

- G_b is the generation of turbulence kinetic energy due to buoyancy, calculated as follows:

$$G_b = \beta \mathbf{g} \frac{\mu_t}{Pr_t} \nabla T \quad \text{with } Pr_t = \frac{c_p \mu_t}{k_t} = 0.85 (K - \varepsilon \text{ Model}) \quad \beta = -\frac{1}{\rho} \left(\frac{\partial \rho}{\partial T} \right) \quad (58)$$

- Y_M represents the contribution of the fluctuating dilatation in compressible turbulence to the overall dissipation rate, calculated as follows:

$$Y_M = 2\rho \varepsilon \frac{K}{a^2} \quad \text{where } a = \text{sound velocity} \quad (59)$$

The turbulent viscosity is computed by combining k and ε as follows:

$$\mu_t = \frac{\rho C_\mu K^2}{\varepsilon} \quad (60)$$

To close the problem it is necessary to provide several constant values. These values were determined by Launder and Spalding in their work (1972) [53]. The constant values are reported in table 6.1:

<i>Constant values for K-ε Model</i>	
C_{μ}	0.09
$C_{1\varepsilon}$	1.44
$C_{2\varepsilon}$	1.92
σ_k	1.00
σ_ε	1.30

Table 6.1: Constant Values for K-ε Model [53].

Turbulent flows are significantly affected by the presence of walls, then, to obtain correct results, it is necessary a perfect modeling of the boundary layer.

Boundary layer can be divided into two macro regions:

- *Inner region or near wall region*: it represents the 20% of all boundary layer δ ;
- *Outer region*: it represents the remaining 80% of it.

Numerous study [44] have shown that the near wall region can be largely subdivided into three layers. In the innermost layer, called “*viscous sublayer*”, the flow is almost laminar and the molecular viscosity plays a dominant role in momentum and heat or mass transfer. In the outer layer, called the “*fully-turbulent layer or log-law region*”, turbulence plays a major role. Finally, there is an interim region between the viscous sublayer and the fully-turbulent layer where the effects of molecular viscosity and turbulence are equally important: this is called “*buffer layer or blending region*”. Figure 6.3 [44] illustrates these subdivisions of the near-wall region, plotted in semi-log coordinates.

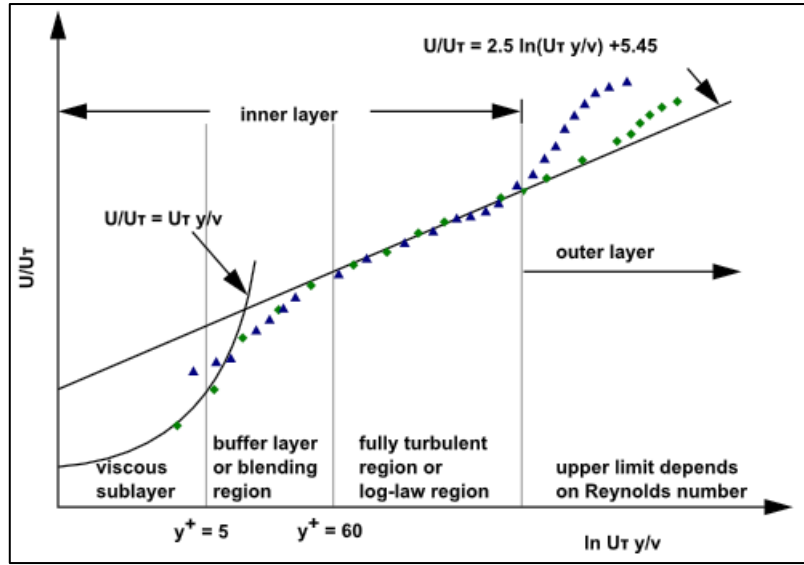


Figure 6.3: Subdivision of the near wall region [44].

Being τ_w the wall shear stress it is possible to define as a appropriate scale velocity for near wall region, the “friction velocity” v_t .

$$v_t = \sqrt{\frac{\tau_w}{\rho}} \quad (61)$$

Close to the wall the flow is induced by viscous effects and does not depend on free stream parameters: it only depends on the distanza y from the wall. Being δ the boundary layer thickness, considering that y is the orthogonal distance from the wall, it is possible to describe the fluid behaviour near the wall introducing two dimensionless parameter:

$$v^+ = \frac{v}{v_t} \quad (62a) \quad \& \quad y^+ = \frac{\rho y v_t}{\mu} \quad (62b)$$

In particular, in the three sublayer, the relationship between these two parameters are:

- *viscous sublayer* ($y^+ < 5$): $\tau(y) = \mu \frac{\partial v}{\partial x} \cong \tau_w \rightarrow y^+ = v^+ \quad (63a)$
- *blending region* ($5 < y^+ < 30$): *transition layer*
- *log-law region* ($30 < y^+ < 500$): $\tau_w = \rho \mu_t \frac{\partial \bar{v}}{\partial y} \cong \rightarrow v^+ = \frac{1}{k} \ln y^+ + C \quad (63b)$

in eq. (63b) k is the Karman constant and its value is 0.4187, while the constant C is 5.5.

Far from the inner layer there is the outer layer ($y^+ > 500$) where the fluid inertia is dominant.

To model the boundary layer, ANSYS® FLUENT® offers two types of approaches:

1. *wall function approach*: the viscous sublayer and buffer layer is not resolved, but semi-empirical formulae called “wall functions” are used to link them to the log-law layer. In this way it is not necessary to modify the turbulence model to account for the presence of the wall.
2. *Near the wall approach*: it is necessary to solve the viscous sublayer and then the turbulence model is modified.

The approach more used is the wall function approach, since there are several correlations that can be used. In the present work is used the “scalable wall function (Sc-WF). This correlation avoid the deterioration due to the presence of mesh fine elements. More details on the use of Scalable wall-function correlation are discussed elsewhere [44],[53].

Since the fluid properties are a function of the temperature through polynomial or power law, the continuity equation and the momentum equation are coupled to the energy equation: the solution of last one provides the temperature distribution throughout the domain.

Energy Equation

The third conservation governing equation to be implemented is the energy equation. A single energy equation is solved throughout the domain and it is shared among the phases, considering the averaged properties of the fluid for each cell. The equation is the following:

$$\frac{\partial}{\partial t}(E\rho) + \nabla \cdot [\mathbf{v}(\rho E + P)] = \nabla \cdot [k_{eff}\nabla T] + S_{E,evap} + S_{E,cond} \quad (64)$$

where:

$$E = \hat{H} - \frac{P}{\rho} + \frac{v^2}{2} = \int_{T_{rif}}^{T_{fin}} c_P dT - \frac{P}{\rho} + \frac{v^2}{2} \quad (65)$$

$$k_{eff} = k_{molecolare} + k_{turbolenta} = k + \frac{c_P \mu_T}{Pr_T} \quad (66)$$

In this equation it is not considered the contribute due to viscous stresses, since the flow induced by the natural convection is relatively low and then this term can be neglected. Moreover, in the energy equation, the radiative source term is not included. Actually, even is a Radiative Heat Transfer Model is enabled in CFD Model (as shown in the next pages), there will be an additional

radiation source term in the energy equation only if the fluid is absorbing/emitting and or scattering. In this model, the fluid is considered as a radiation non participating fluid.

Analyzing the above equation (64), it is possible to assess the meaning of each term:

- $\frac{\partial}{\partial t}(E\rho)$: rate of increase of energy per unit volume;
- $\nabla \cdot [\mathbf{v}(\rho E + P)]$: net rate of energy addition per unit volume due to the convection;
- $\nabla \cdot [k_{eff} \nabla T]$: net rate of energy addition per unit volume due to conduction (diffusion);
- $S_{E,evap} + S_{E,cond}$: rate of increase of energy due to external energy source term (condensation/evaporation phenomena).

For what concern the energy balance and the estimation of the heat transfer during the evaporation or condensation process, only one expression is required, in which the energy source terms related to evaporation ($S_{E,evap}$) and condensation ($S_{E,cond}$) are expressed as follows:

$$S_{E,evap} = M_{EL}\lambda_0 = -0.1\rho_L\alpha_L \left| \frac{T_L - T^0}{T^0} \right| \lambda_0 \quad (67a)$$

$$S_{E,cond} = M_{CV}\lambda_0 = 0.1\rho_V\alpha_V \left| \frac{T_V - T^0}{T^0} \right| \lambda_0 \quad (67b)$$

where λ_0 represents the latent heat of vaporization.

In the subroutine with which the energy source terms are implemented, both the saturation temperature (K) and the latent heat of vaporization (J kg^{-1}) are a function of the absolute pressure of the domain (Pa), which changes with the time. The relationships are obtained through a polynomial fitting of thermodynamic data available in literature [54],[55].

$$\lambda_0 = -0.0682P + 403262 \quad (68)$$

$$T^0 = -6.0 * 10^{-12}P^2 + 5.0 * 10^{-5}P + 253.76 \quad (69)$$

Radiative Transfer Equation (RTE) and Radiation Model

Considering that the walls, in particular the walls in contact with the vapour phase, can reach high temperatures during the engulfment of the storage vessel, it was necessary to enable a model to predict the radiative heat transfer.

The radiative heat transfer mechanism is governed by the Stefan-Boltzmann law [43]:

$$\dot{q}_{rad} = \sigma(T_{Max}^4 - T_{Min}^4) \quad (70)$$

where T_{max} is the absolute wall temperature and T_{min} is the lading absolute temperature, while σ is the Stefan–Boltzmann constant and its value is $5.637 \cdot 10^{-8} \text{ W m}^{-2} \text{ K}^{-1}$. Since explained in a previous chapter (sec. 3.2.), high wall temperature values are reached preferentially in the vapour domain, where the stored fluid is assumed to be non participating in radiation. This hypothesis, and the consideration that the radiation phenomenon takes place in an enclosure like the internal of a fire engulfed vessel, are the reasons why, among the Radiation Heat Transfer Models available in ANSYS® FLUENT®, the Surface to Surface (S2S) Model [56] is chosen.

The choice of radiation model can be improve since the fluid is not participating of the radiation, but in absence of experimental data of fluid radiative properties, it is the only possible choose to consider the wall emissivity.

According to the S2S Radiation Model the exchange of radiative energy is unaffected by the medium that separates the surfaces. Moreover, these walls are assumed to be gray and diffuse and then the Kirchoff’s law is valid: the emissivity (ϵ) of the surface equals its absorptivity (α_{bs}). Thus, according to the gray–body model, if a certain amount of radiant Energy (E) is incident on a surface, a fraction (r) is reflected, while a fraction (α_{bs}) is absorbed. Steel walls in the infrared spectrum can be considered opaque so the fraction of trasmitted energy (τ) is zero. It follows, from the conservation of energy, that:

$$\alpha_{bs} + r = 1 \quad \& \quad \alpha_{bs} = \epsilon \quad \rightarrow \quad \epsilon = 1 - r \quad (71)$$

Considering a surface k and the energy flux incidents on it, the energy flux leaving from this surface is:

$$\dot{q}_{out,k} = \epsilon_k \sigma T_k^4 + r_k \dot{q}_{in,k} \quad (72)$$

The amount of energy incident upon a surface from another surface is a function of the S2S “view factors (F_{jk})”: the fraction of energy leaving surface j that is incident on surface k. View factor between two surface is given by:

$$F_{jk} = \frac{1}{A_j} \iint \frac{\cos \vartheta_j \cos \vartheta_k}{\pi r_{jk}^2} \delta_{jk} dA_j dA_k \quad (73)$$

where δ_{jk} is determinated by the visibility of dA_j to dA_k .

So it is possible to express the incident energy flux upon the surface k:

$$A_k \dot{q}_{in,k} = \sum_{j=1}^N A_k \dot{q}_{out,j} F_{jk} \quad (74)$$

Because of among the surfaces it exists a reciprocity mathematical relation:

$$A_k F_{kj} = A_j F_{jk} \quad (75)$$

so that:

$$\dot{q}_{in,k} = \sum_{j=1}^N \dot{q}_{out,j} F_{kj} \quad (76)$$

$$\dot{q}_{out,k} = \varepsilon_k \sigma T_k^4 + r_k \sum_{j=1}^N \dot{q}_{out,j} F_{kj} \leftrightarrow J_k = E_k + r_k \sum_{j=1}^N J_j F_{kj} \quad (77)$$

The S2S radiation model is computationally very expensive when the radiation and view factors have to be calculated for a large number of surfaces. To reduce the computational time as well as the storage requirement, the number of surfaces is reduced by creating surface “cluster”. The surface clusters are made by starting from a face and adding its neighbors and their neighbors until a specified number of faces per surface cluster is collected [56]. More details on the S2S model are reported elsewhere [57].

Equation of State and Physical Properties Implemented in the Simulations

The LPG stored in the vessels exposed to the fire is a mixture of propane and butane, constituted mainly by propane for about 95–98%. For this reason, in the CFD Model the LPG is assumed as pure propane, neglecting the presence of heavier components.

To close mathematically the problem, it is necessary to define the fluid properties as a function of thermodynamic parameters. In the present work, the liquid and vapour properties are implemented as a function of temperature.

Simplified correlations were built as polynomial functions or power law, interpolating available thermodynamic data [22], [55].

In table 6.2, the interpolation results implemented in the CFD Model are summarized:

Property	Units	Correlation
Liquid density (ρ_L)	Kg/m ³	$\rho_L = -24.063 + 4.9636T - 0.0109T^2$
Vapour density (ρ_V)	Kg/m ³	Peng–Robinson EOS
Liquid heat capacity (c_{PL})	J/(kg·K)	$c_{PL} = 36309 - 230.2T + 0.3941T^2$
Vapour heat capacity (c_{PV})	J/(kg·K)	$c_{PV} = 345.58 + 4.4019T$
Liquid thermal conductivity (k_L)	W/(m·K)	$k_L = 0.26755 - 6.6 \cdot 10^{-4}T + 2.77 \cdot 10^{-7}T^2$
Vapour thermal conductivity (k_V)	W/(m·K)	$k_V = -0.0088 + 6.0 \cdot 10^{-5}T + 1.0 \cdot 10^{-7}T^2$
Liquid dynamic viscosity (μ_L)	Pa·s	$\mu_L = 709137 \cdot T^{-3.986}$
Vapour dynamic viscosity (μ_V)	Pa·s	$\mu_V = (4.9054 \cdot 10^{-8}) \cdot T^{0.90125}$

Table 6.2: Correlations Adopted for the evaluation of Propane Physical Properties (Interpolation of data reported by [22] and [55]).

Modeling the vapour density requires a major attention: it is both a function of pressure and temperature. Since the fluid in storage condition and during the exposure to fire is at considerable pressure (more than 10 bar), the Ideal Gas Law EOS (Equation of state) is unsuitable to describe the behaviour of fluid. The software ANSYS® FLUNT® v. 14.5 allows to use several types of EOS: the Peng Robinson EOS (PR–EOS) was chosen in this study, since it was considered more appropriate to predict the thermodynamic behaviour of bi–phase system.

The PR–EOS has the following form [48]:

$$P(\text{bar}) = \frac{RT}{(v_m - b_{PR})} - \frac{a_{PR}\psi(T)}{v_m^2 + 2b_{PR}v_m - b_{PR}^2} \quad (78)$$

where:

- $R \left(\frac{\text{cm}^3 \cdot \text{bar}}{\text{mol} \cdot \text{K}} \right) = 83.144$
- $a_{PR} \left(\frac{\text{cm}^6 \cdot \text{bar}}{\text{mol}^2} \right) = 0.45724 \frac{R^2 T_C^2}{P_C}$
- $b_{PR} \left(\frac{\text{cm}^3}{\text{mol}} \right) = 0.0778 \frac{RT_C}{P_C}$
- $\psi(T) = \left\{ 1 + (0.37464 + 1.54226\omega - 0.26992\omega^2) \left[1 - \left(\frac{T}{T_C} \right)^2 \right] \right\}$

By the PR–EOS is obtained the $v_m = \frac{V}{n}$ expressed in (cm³ mol⁻¹). For the calculation of vapour density is used the following relationship:

$$\rho_V \left(\frac{\text{kg}}{\text{m}^3} \right) = 1000 \frac{M_W}{v_m} \quad (79)$$

In table 6.3, the pure propane properties necessary to solve the PR–EOS are reported [55]:

Property	Units	Value
Molecular Weight (M_w)	g/mol	44.10
Critical Temperature (T_c)	K	369.9
Critical Pressure (P_c)	bar	42.051
Acentric Factor (ω)	-	0.152

Table 6.3: Properties of pure propane necessary to solve the PR-EOS [55].

6.2. Numerical implementation of the CFD Model

Once the problem has been analyzed from the theoretical point of view and the sub–models to describe the relevant phenomena have been chosen, it is necessary to set the CFD Model. The implementation of it can be subdivided in three steps:

- Mesh definition and construction;
- Set up of the CFD model;
- Solution method.

Mesh definition and construction

To ensure a good solution of a given CFD numerical model a good grid is required [56]. The mesh represents the discretization of a geometrical system into smaller simple shapes cell. In other words, the cell is the CV in which the fluid flow domain is broken–up. Both in 3D and 2D domain, the centre of the cell is the location where field data are stored in ANSYS® FLUENT® software. A satisfactory mesh to fulfill the following features:

- It has to represent the geometry and the fluid flow domain as faithfully as possible.
- It has to be capable of simulating complex geometry with a reasonable number of cells, so do not be too computationally expensive.
- It has to be able to prevent false diffusion problems.

There are two different types of meshes:

1. *Structured Meshes*: the cells are topologically rectangular, so cells volume is a quadrilateral in 2D or hexahedron in 3D. Each CV is linked only to its immediate neighbors (4 in 2D or 6 in 3D). Block–structured meshes can handle with complex

geometries and have different cells size. The number of mesh elements can be increased where it is required by the physical behaviour of the fluid flow. Using a structured mesh reduces the storage and CPU requirements.

2. *Unstructured Meshes*: the cell can be of any shape: for this reason an unstructured mesh is more flexible but the CPU requirements to solve the governing equations is high.

In the present study, a block structured mesh is adopted. For the construction of the mesh was used the ANSYS® ICEM–CFD® software: this is the best tool to build this type of mesh. Using a block–structured mesh, it is possible to refine the near wall region, while the discretization in the rest of domain is more coarse.

Once created, the mesh is processed in ANSYS® FLUENT® software. It is an unstructured solver: for this it is necessary to convert the structured mesh in an unstructured mesh before being processed in the CFD software.

In the representation of the domain is necessary to make some considerations related to the symmetry of the problem, so as to reduce as much as possible the number of cells without affecting the fidelity of the simulation results. In the present work, a 3D real system was represented and solved using a simple 2D mesh with a limited number of cells, as it is shown in figure 6.4.



Figure 6.4: Geometrical domain a) real system b) simulated system.

The approximation carried out with this geometric simplification is to not consider the incoming heat flux from the hemispherical ends of the tank car, since it is very lower than the incoming flux heat of the walls of the cylindrical shell. The typical ratio between the cylindrical shell area and dished area for horizontal cylindrical vessel is [55]:

$$\frac{A_{cyl,shell}}{2A_{hemisph,shell}} = 5 \div 15 \quad (80)$$

Semicircular representation is valid when the vessel is completely engulfed in a pool fire or jet fire and the load heat is constant over all the walls. When the applied load heat is a function of spatial position and then the engulfment is not complete, it is necessary the construction of a circular mesh. Finally, to assess the quality of the created mesh, before importing in the CFD software, it is necessary to control the value of some parameters:

1. *Skewness*: it quantifies the difference among the internal angle values of the cell. A good mesh has a skewness factor close to 0.
2. *Quality*: it is a indicator with which the user can see where the mesh has to be improved, since the cell shape is not good for the equations solution. This value has to be near to 1.
3. *Aspect Ratio*: it is the ratio between the longest and the shortest edge of each cell. A good mesh has low aspect ratio (less or equal than 50).

Set Up of the CFD Model on ANSYS® FLUENT® Software

The task pages accessed under “*Solution Setup*” allow to perform the most common problem setup tasks. This section is formed by various items, as shown in figure 6.5 [56].

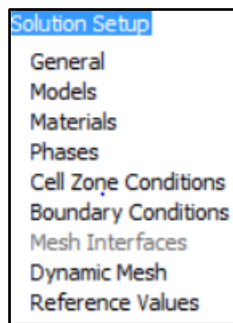


Figure 6.5: Items of Solution Setup in ANSYS® FLUENT® software [56].

General item allows to set various generic problem settings. Here the user can modify the mesh imported by ANSYS® ICEM–CFD® software, scaling and unscaling it. Moreover can be defined if the simulation is transient or steady and if the gravity force have to be considered during the simulation. If the gravity is important for the prediction, it is necessary to set the gravity acceleration value in the correct spatial direction.

In this task page is carried out the choice of the solver method for the fluid flow equations. In ANSYS® FLUENT® are available two types of approaches: “Pressure Based Solver” or “Density Based Solver”. Multiphase problems can be solved only using the Pressure Based Solver, then it is chosen as numerical method to solve the governing equations. This approach employs a correction projection procedure to solve the Navier–Stokes equations set: the pressure field is extracted by solving a pressure correction equation which is obtained by manipulating the momentum equation to satisfy continuity equation.

So as to derive with a Pressure Based Solver the pressure field, a velocity–pressure coupling relationship is necessary to enforce mass conservation: the momentum equation can be solved only if the pressure field is known. Therefore the aim of the pressure-velocity coupling is to find a way to improve the value of the guessed pressure field, so as the resultant velocity will get closer to satisfy continuity. In ANSYS® FLUENT® some algorithms to solve the velocity and pressure field are available: SIMPLE, SIMPLER, PISO, Coupled. In the next pages, the scheme chosen for the CFD Model will be explained.

Models item allows to choose the model to describe the relevant physical phenomena (see sec. 6.1.2), while in *Materials* item the substances involved in the simulation and their properties are defined (see sec. 6.1.2).

In *Phases* item is necessary to indicate what is the primary and secondary phase for the solution of the multiphase model. The VOF model requires that the secondary phase is a liquid, so in this case the choice has been obliged. Table 6.4 summarizes the models, materials and phases implemented in this work.

<i>Models</i>	<i>Materials & Phases</i>
Multiphase: Volume of Fluid (VOF)	Vapour Propane: Primary Phase
Viscous: Standard k-ε, Scalable Wall Function (St k-ε, Sc-WF)	Liquid Propane: Secondary Phase
Energy	
Radiation: Surface to Surface (S2S)	Steel: Wall Material

Table 6.4: Summary of the Models, Materials and Phases in the present study.

In *Cell zone conditions* are set the operative conditions and the source terms contained in the subroutine (UDF) interpreted for the evaporation/condensation phenomenon. This subroutine is reported in Appendix 1.

Finally, it is necessary the implementation of the *Boundary Conditions* of the problem: in this case it is implemented the value of flux heat incident on the outer wall. A detailed analysis of BC related to the simulations will be carried out in some successive chapter.

Solution of the CFD Model in ANSYS® FLUENT® Software

The task pages accessed under “*Solution*” allow to choose the solution method to solve governing equations and other parameters of simulation. This section is formed by various items, as shown in figure 6.6 [56].

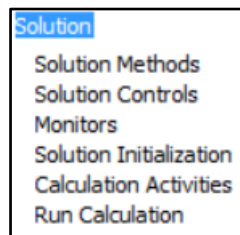


Figure 6.6: Items of Solution in CFD software [56].

In *Solution Method* item is carried out the choice of the method needed to convert the governing equation to algebraic equations set and to solve them. The first thing to choose is the method to solve pressure–velocity coupling: in this work the SIMPLE scheme is chosen. Figure 6.7 shows the SIMPLE algorithm to solve the pressure-velocity coupling.

In this scheme, the real value for each properties can be written as the sum of two terms: the guessed term (indicated with *) and the correction term (indicated with ‘). When the correction term is about zero means that the convergence is reached: the Navier–Stokes Equations, Energy Equation and Continuity Equation are satisfied.

Being a transient problem, the SIMPLE algorithm is solved for each “time step”.

As already mentioned, to pass from differential equations to algebraic equations system, interpolation and approximation technical are needed. In the table 6.5 are reported the choice of technical for the spatial and temporal discretization. More details of this approximation methods are discussed elsewhere [43], [56], [58].

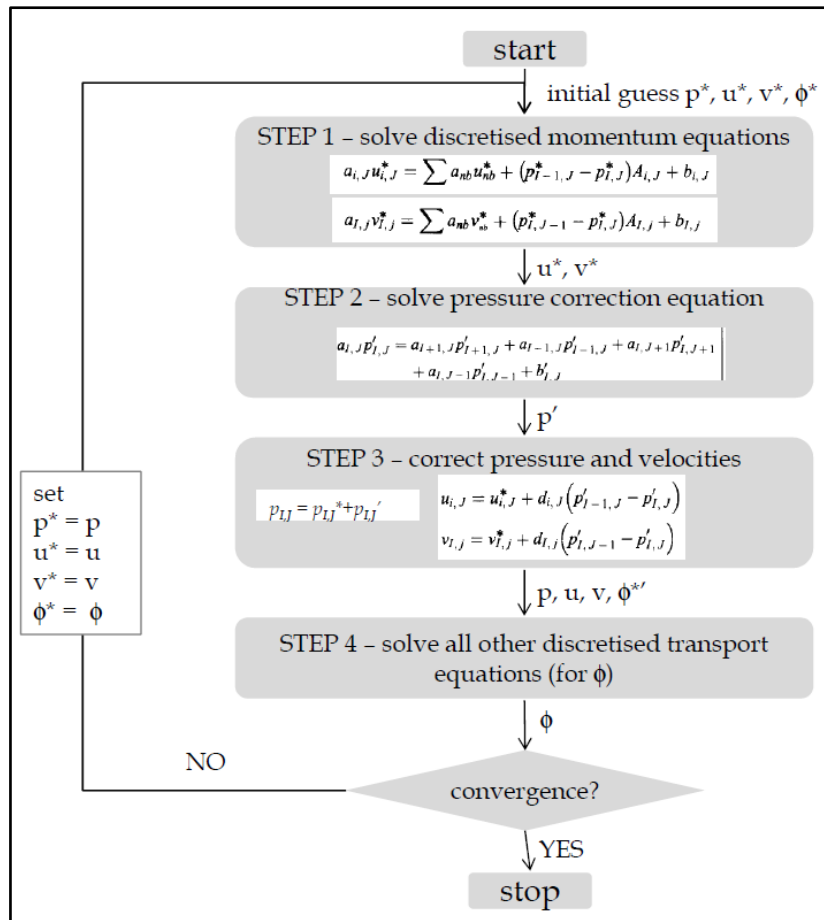


Figure 6.7: SIMPLE algorithm [58].

SOLUTION METHODS

Pressure–Velocity Coupling	Scheme: SIMPLE
	Gradient: Least Squares Cell Based
	Pressure: Body Force Weighted
	Density: First Order Upwind
Spatial Discretization	Momentum: First Order Upwind
	Volume Fraction: Geo-Reconstruct
	Turbulent Kinetic Energy: First Order Upwind
	Turbulent Dissipation Rate: First Order Upwind
	Energy: First Order Upwind
Transient Formulation	First Order Implicit

Table 6.5: Summary of the Solution Methods used in the present work.

In *Solution Controls*, under-relaxation factors are set: these parameters help the simulations to arrive to the convergence. In the present work this values are set between 0.3 and 1, depending on the property of interest.

Monitors are used to set the residual needed for the determination of the convergence criteria. For all equations to solve, the residual values are $1 \cdot 10^{-6}$.

To start the simulation, an *Initialization* is necessary: in this menu are set the initial values of temperature, pressure, X-velocity and Y-velocity. Moreover it is necessary to patch the zone where the liquid is present: it depends on the geometry and the filling level of liquid at the initial time of the simulation.

Finally, the “Time Step Size” and the “number of Time Step” has to be set. The choice of the Time Step Size depends by the velocity and the cell size, since the Curant number has to be less than 10–20 to ensure that the time discretization gives plausible results. For this reason, according to the velocity field and the cell size, for each simulation a different “Time Step Size” will be set.

6.3. Development of advanced computational mesh

The biggest limit of the meshes developed in the previous work [42], it was to have to tighten nearby of the liquid–vapour interface, in order to have not any convergence problems due to the evaporation/condensation phenomena. To apply the CFD Model to any liquid filling level, it was necessary to build a very fine mesh over all the domain. Table 6.6 shows the main features of the mesh used for industrial accidents simulation.

The mesh is extremely uniform over all the domain. However, in the proximity of the vessels wall, a further thickening along vertical direction was carried out, in order to improve the predictions of the velocity profiles.

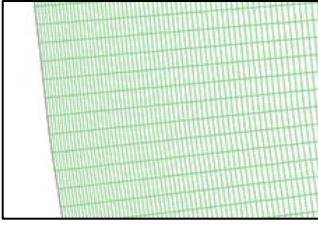
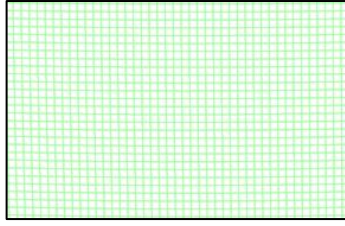
<i>Graphic representation:</i>		
	<i>Detail of a portion of the domain close to the vessel wall.</i>	<i>Detail of a portion of the domain in the liquid bulk and liquid-vapour interface.</i>
<i>Cell number:</i>	267605	
<i>Min. cell size:</i>	0.873 mm	
<i>Max cell size:</i>	8.405 mm	
<i>Orthogonal quality value:</i>	0.972–1 (average: >> 0.99)	
<i>Maximum aspect ratio value:</i>	9.63	

Table 6.6: Main features of the mesh used for industrial accidents simulation.

7. CFD model validation

In this chapter the validation process of the CFD Model will be discussed; the simulation set up and the results of the validation case will be reported. Experimental data obtained in the large scale bonfire test performed by Townsend et al. [22] were taken as a reference data source for model validation. The experimental test was carried out in 1974 in New Mexico (USA). On the official report [22], a lot of information about the pressure, fluid temperature, incident flux heat on the wall and liquid level are reported. Data of interest were reported in Section 4.1.2.

7.1. Simulation set up for the validation case

To simulate the pool fire total engulfment it is necessary set an incident flux heat on the wall of tank as boundary condition. For the validation of the CFD model, an uniform engulfment is assumed and a specific User Define Function is built to implement the results recorded by a radiometer in function of the time. The experimental flux heat is reported in figure 4.7.

The PRV first opening occurred after 132 seconds by the fire exposure: for this reason the UDF considers the trend of incident flux heat up to that time. It was written with the “Visual Studio Software”: this tool allows to write in C++ language in a windows machine. This subroutine, called “flux_time_Townsend”, is reported in appendix 2..

Table 7.1 shows the flux heat values, extracted by a figure 4.7 up to 132 seconds, for some point of time. Moreover, the mathematical function used for time discretization is reported.

For the correct prediction, it is important to record the peaks of heat flux. Calculating the average integral of the flux heat upon 125 seconds, the value is 43407 W m^{-2} . Performing a simulation by setting this value as incident flux heat, the simulation results are more different than experimental test results.

The initial conditions set for validation of the CFD Model are equal to those experimental. Table 7.2 shows the initial conditions implemented in ANSYS® FLUEN® software for the validation case.

Time discretization of incident flux heat on the wall of the tank			
<i>time interval of the simulation (sec)</i>	<i>flux heat at initial of the time interval ($W m^{-2}$)</i>	<i>flux heat at final of the time interval ($W m^{-2}$)</i>	<i>mathematical function</i>
0 ÷ 25	5250	5250	constant
25 ÷ 50	5250	57750	linear increasing
50 ÷ 60	57750	58800	linear increasing
60 ÷ 75	58800	59850	linear increasing
75 ÷ 85	59850	52500	linear decreasing
85 ÷ 90	52500	59850	linear increasing
90 ÷ 105	59850	59850	constant
105 ÷ 120	59850	69300	linear increasing
120 ÷ 125	69300	60900	linear decreasing
> 125	60900	60900	constant

Table 7.1: Time discretization of incident flux heat on the wall of the tank.

INITIAL CONDITIONS		
Absolute Pressure	0.963	MPa
Temperature	294.15	K
X-Velocity	0	$m s^{-1}$
Y-Velocity	0	$m s^{-1}$
Turbulent Kinetic Energy	0.00001	$m^2 s^{-2}$
Turbulent Dissipation Rate	0.00001	$m^2 s^{-3}$
Volume Fraction	0.96	-

Table 7.2: Initial conditions set for validation of the CFD Model.

As regards the calculation information, this simulation was performed on a ASUS series N551J , with INTEL® CORE™ i7-4710HQ, CPU 2.50 GHz, 8 GB RAM and 64 bit operating system type. Parallel calculation was performed with four cores (eight threads), in order to obtain a computational time of about 6 min to simulate 1 sec of real time. The time step was set at value of 0.025 sec, in order to have a reasonable Courant number.

7.2. Validation results

The crucial point to determine the predictive capabilities of a CFD Model are the validation results. The validation is carried out analyzing the following parameters:

1. Lading temperature distribution;

2. Tank absolute pressure vs time;
3. PRV opening time (first opening);
4. Tank filling level vs time.

7.2.1. Lading Temperature Distribution

In the Townsend test two grids of thermocouples were welded to the inner wall of the vessel to measure the lading temperature into the tank. On the official report [22] the measured temperature values for each thermocouple are reported for some time values. The lading temperature distribution predicted by CFD Model is then compared with these measurements. The comparison is made considering four different time values: twice for the rear cross-section and twice for the front cross-section before the PRV opening time. Actually the comparison time values are:

1. Rear cross-section values 1: 52.6 seconds;
2. Rear cross-section values 2: 94.5 seconds;
3. Front cross-section values 1: 71.2 seconds;
4. Front cross-section values 2: 113.5 seconds.

Moreover, on the report, the spatial position (x,y,z) for each thermocouple is indicated: consequently, for each desired point was possible to make a comparison.

Figures 7.1 and 7.2 show the comparison between the temperature values recorded in the Townsend test and the temperature values predicted by the CFD Model, respectively for the Rear cross-section and Frontcross-section.

The red lines reported on the previous figure indicate the uncertainty range due to the instrumentation: as already mentioned, the thermocouples have an accuracy of $\pm 2,2$ °C. According with the figures 7.1 and 7.2, the CFD Model is able to accurately predict the lading temperature distribution, since only a few point do not fall within the uncertainty range.

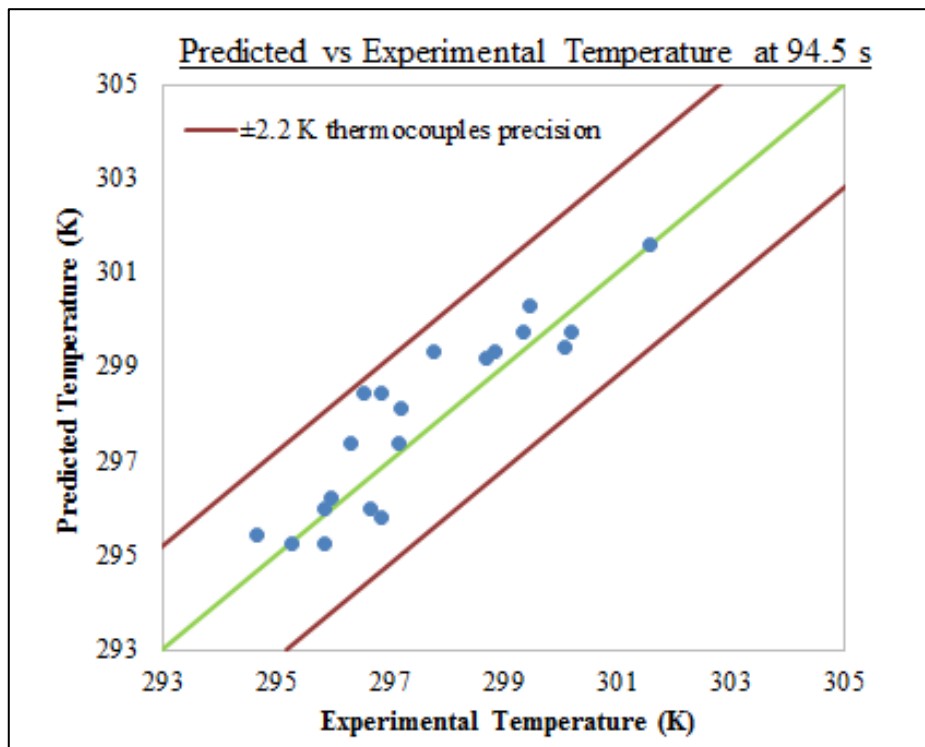
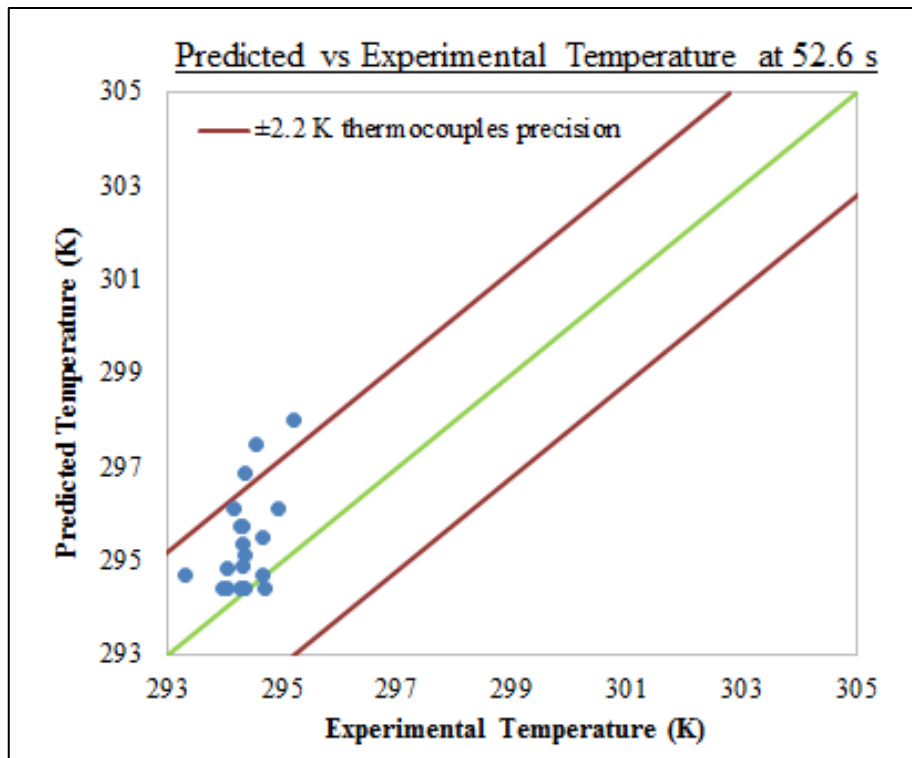


Figure 7.1: Experimental vs CFD Model temperature for the Rear cross-section at two different time values.

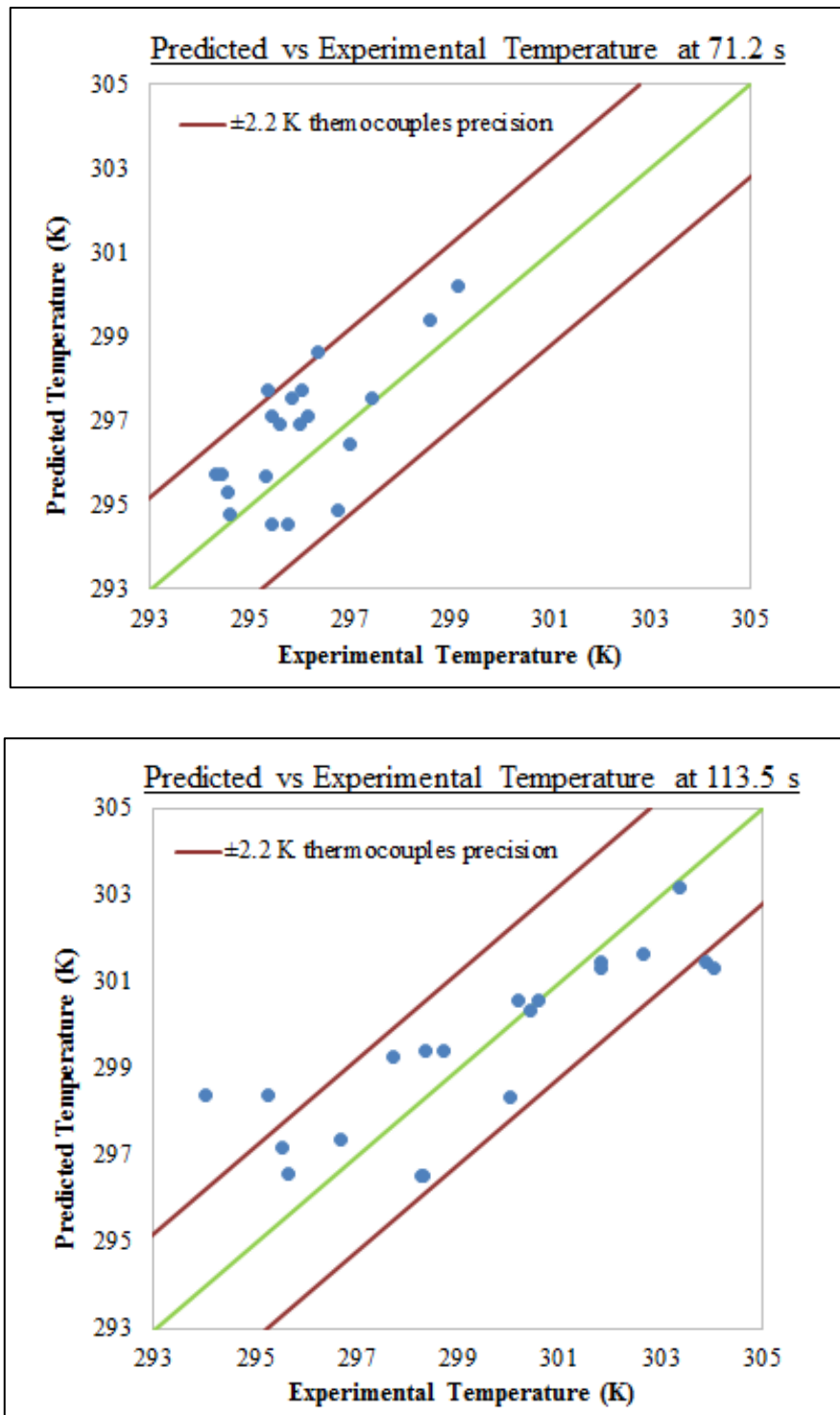


Figure 7.2: Experimental vs CFD Model temperature for the Front cross-section at two different time values.

7.2.2. Tank Pressure vs Time

Another key parameter that needs to be compared to assess the predictive capabilities of the CFD Model is the tank pressure in function of the time. The pressure can be compared up to PRV first opening time. In this case it is 132 seconds and the pressure is 1.816 MPa.

Figure 7.3 shows the comparison between the pressure predicted by the CFD Model and the experimental Pressure.

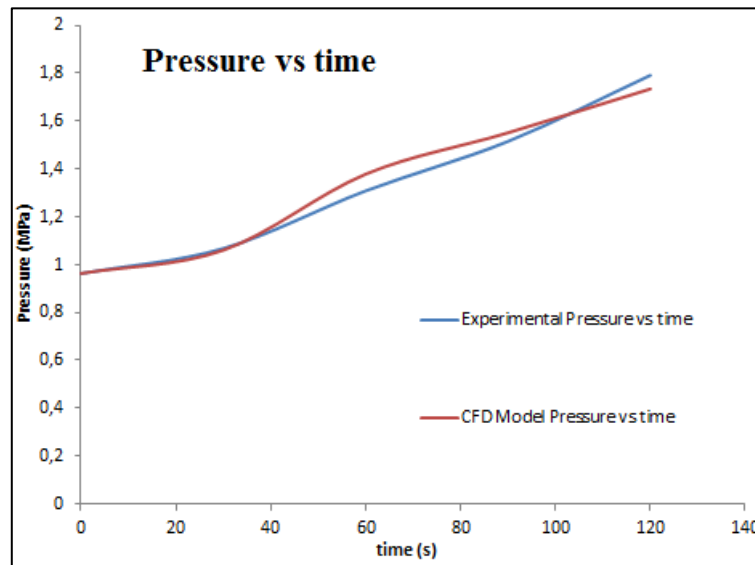


Figure 7.3: Experimental vs CFD Model pressure in function of the time.

In table 7.3 the pressure values for Experimental and CFD Model are reported.

Time (s)	Experiment Pressure (MPa)	CFD Model Pressure (MPa)	Relative Error (%)
0	0.963	0.963	0
30	1.067	1.060	-0.65604
60	1.308	1.378	5.351682
90	1.515	1.551	2.376238
120	1.791	1.734	-3.18258
132	1.816	1.799	-0.93612

Table 7.3: Experimental vs CFD Model Pressure for some time values.

The CFD Model predicts very well the increase of pressure over time and the little difference are essentially due to the discretization time for the implementation of the incident flux heat (sec. 7.1.).

An estimate of the goodness of prediction can be done by evaluating the relative percentage error: this value does not exceed 5%.

7.2.3. PRV Opening Time

One of the main indicators to assess the predictive capabilities of the CFD Model is a comparison of the time at which the pressure reaches the PRV set pressure: for this time, the first opening of PRV occurs. This parameter also provides information about the correct models and equation implemented to describe the behaviour and the physical properties of the fluid.

In the experimental test, the PRV first opening time occurred after 132 seconds from the fire exposure of the tank. In table 7.4 is reported the difference between the Experimental and CFD Model PRV opening time.

PRV Pressure Set (MPa)	Experimental PRV opening time (s)	CFD Model PRV opening time (s)	Relative Error (%)	$\Delta t = t_{\text{exp}} - t_{\text{CFD Model}}$ (s)
1,816	132,0	135,7	2,803	3,7

Table 7.4: Experimental vs CFD Model PRV opening time.

7.2.4. Tank Filling Level vs time

In addition to the temperature gradient vertical, it is observed in the liquid phase also a density gradient vertical, resulting from the mechanism of natural convection into the stored liquid during fire exposure. Density decreases from bottom up to liquid–vapour interface heating also causes an increase of the liquid level in the tank. Last parameter to validate the CFD Model is linked to the comparison of liquid level as a function of time.

Figure 7.4 shows the comparison between the filling level predicted by the CFD Model and the liquid level recorded in the experimental test.

The same comparison is carried out in table 7.5, in which the relative percentage error between experimental test and CFD Model is reported.

Starting from a liquid level height bottom–interface of 2.736 meters, the resulting swelling of the interface is of 0.068 meters with a final height of 2.804 meters at 117.84 seconds.

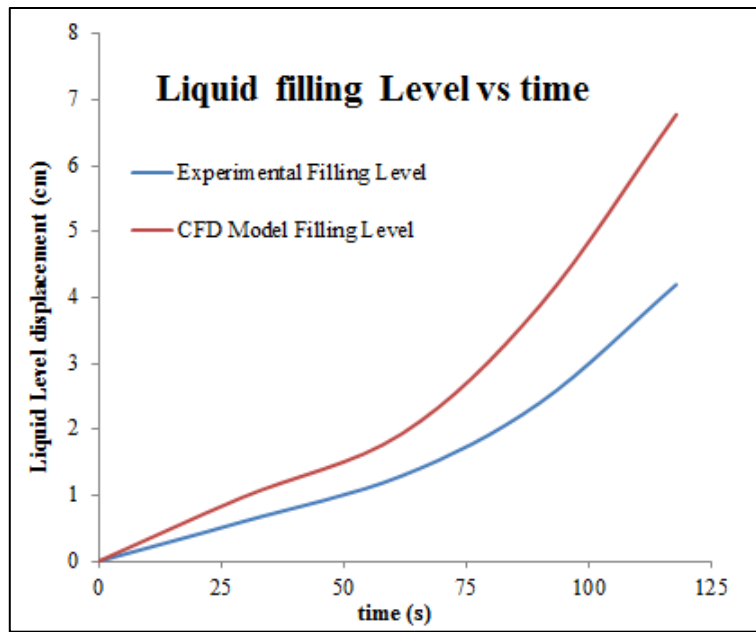


Figure 7.4: Experimental vs CFD Model filling level in function of the time.

<i>Time</i> (s)	<i>Experiment Filling Level</i> (m)	<i>CFD Model Filling Level</i> (m)	<i>Relative Error</i> (%)
0	2.736	2.736	-
29.36	2.742	2.746	0.135
61.96	2.749	2.755	0.233
89.91	2.760	2.775	0.533
117.84	2.778	2.804	0.929

Table 7.5: Experimental vs CFD Model filling level for some time values.

Using a radiation model more suitable to the present problem would likely help to fill the discrepancy between the filling level values of experimental test and CFD Model: however, considering the relative percentage error, the difference are limited.

7.3. Mesh independence

Once established the CFD Model, it is necessary to test the independence of numerical grid by the results. This procedure is carried out using a mesh more fine than that used for the validation model.

The purpose of the grid independence is to use in the simulation a mesh with the minimum number of elements, in order to obtain a reduction of the computational time. However, this mesh have to provide the same results of any other mesh with a higher number of elements.

The features of the two meshes used to assess the grid independence are reported in table 7.6.

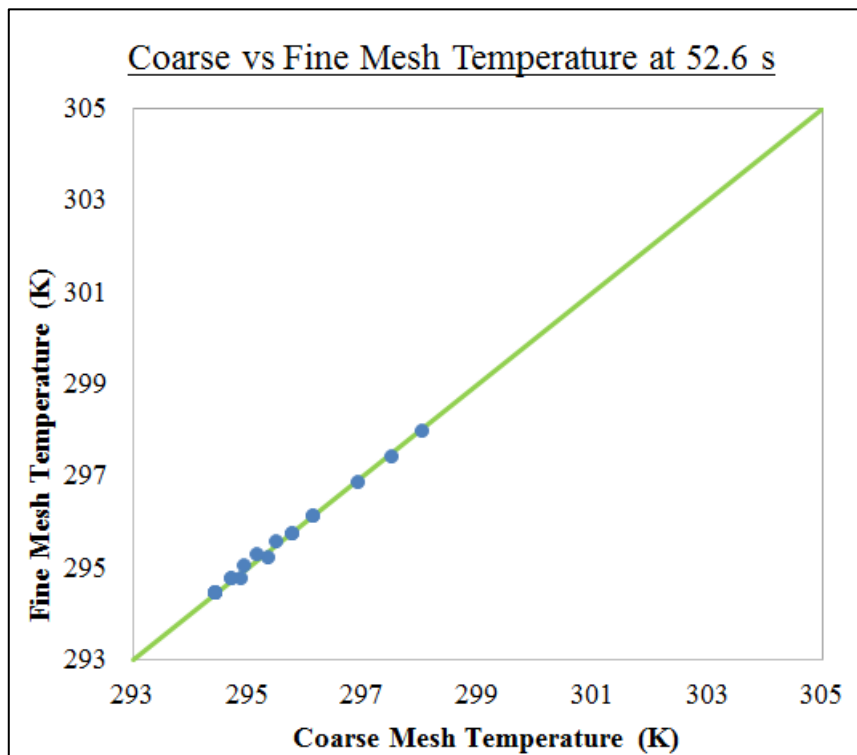
	<i>Coarse Mesh</i>	<i>Fine Mesh</i>
<i>Cell number:</i>	9966	39864
<i>Min. cell size:</i>	1.206 mm	0.225
<i>Max cell size:</i>	32.89 mm	16.44 mm
<i>Orthogonal quality value:</i>	0.558-1 (average: >> 0.95)	0.702-1 (average >> 0.95)
<i>Maximum aspect ratio value:</i>	19.3	51.4

Table 7.6: Coarse vs fine mesh features.

To assess the grid independence were analyzed the same parameters of the previous validation process: lading temperature distribution, tank pressure and tank filling level in function of the time and PRV opening time. In the following figures and tables, the results of the grid independence process are reported.

lading temperature distribution

Figures 7.5 and 7.6 show the comparison between the temperature values predicted by the CFD Model, implementing coarse and fine mesh, respectively for the Rear cross–section and Front cross–section.



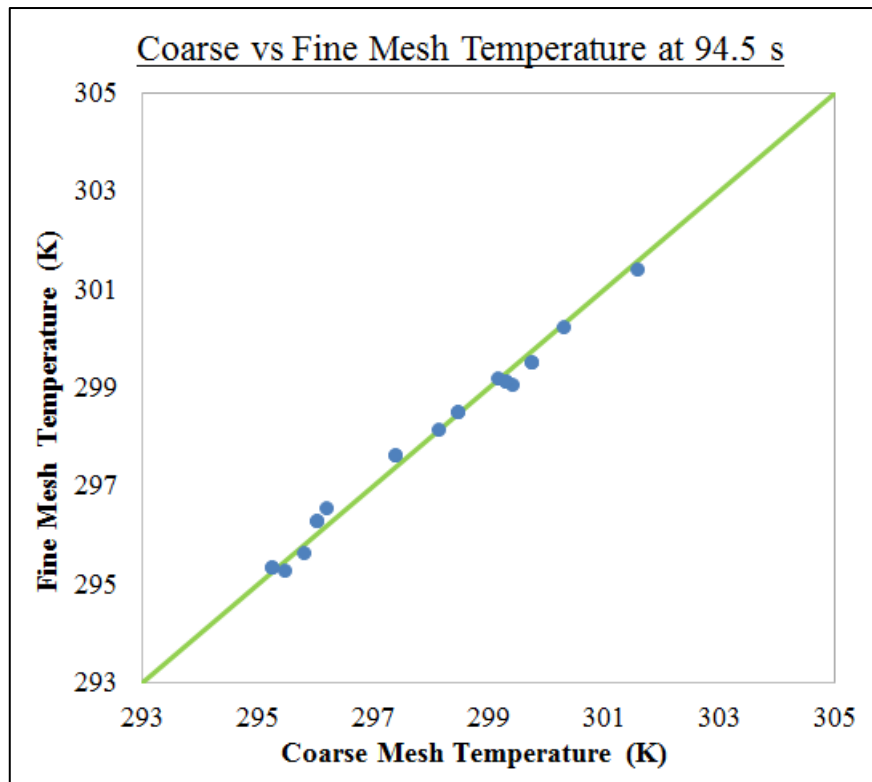
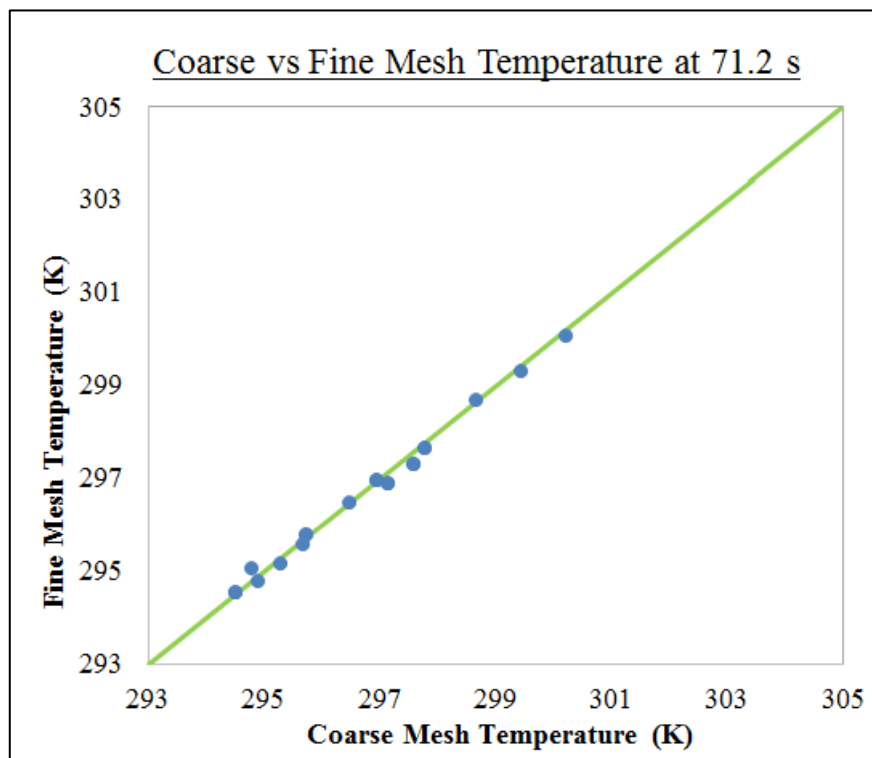


Figure 7.5: Coarse vs Fine Mesh temperature for the Rear cross-section at two different time values.



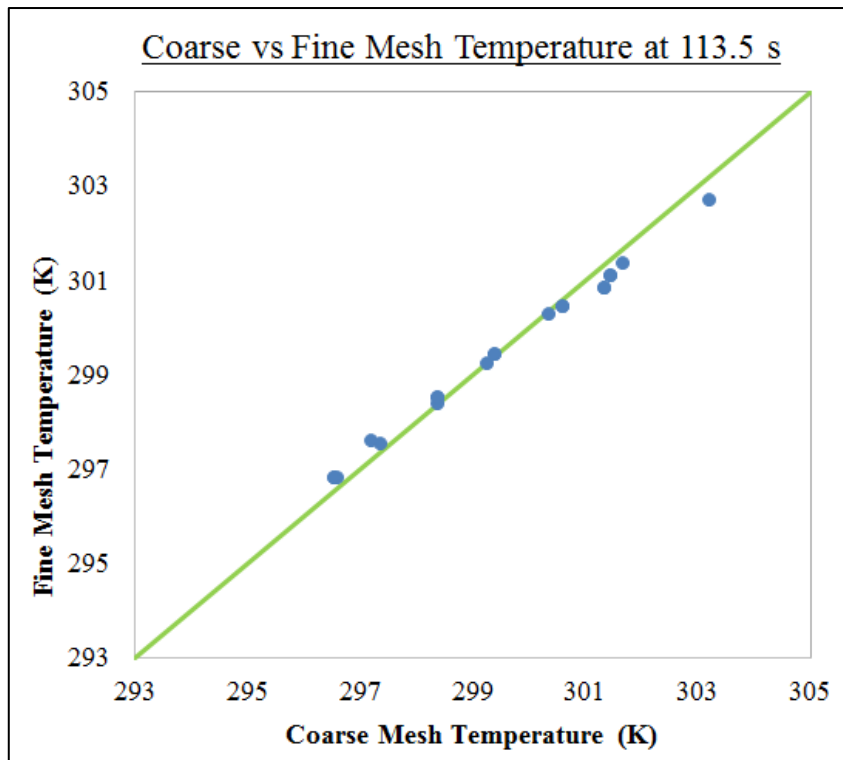


Figure 7.6: Coarse vs Fine Mesh temperature for the Front cross-section at two different time values.

From the figures 7.5 and 7.6, it can be noted that the two grids predict in a similar manner the temperature distribution in the tank: considering the absolute value, the maximum temperature difference between the fine and coarse mesh is about of 0.5 °C.

tank pressure

The comparison between the pressure predict by the CFD Model, implementing fine and coarse mesh is summarized in table 7.7.

Time (s)	Fine Mesh Pressure (MPa)	Coarse Mesh Pressure (MPa)
0	0.963	0.963
30	1.064	1.060
60	1.393	1.378
90	1.573	1.551
120	1.728	1.734

Table 7.7: Coarse vs Fine Mesh Pressure for some time values.

Figure 7.7 shows the trend of the pressure as a function of the time for the experimental test and the CFD Model, implementing coarse and fine mesh.

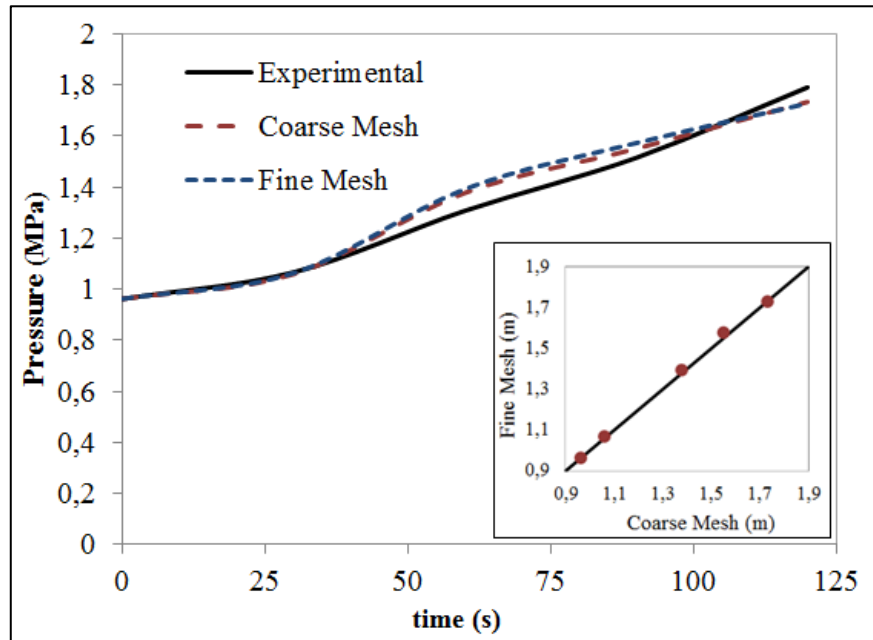


Figure 7.7: Experimental vs CFD Model (for Coarse and Fine mesh) pressure in function of the time.

Analyzing both the table 7.7 and the figure 7.7, it can be noted that the pressure prediction for the CFD Model is not dependent by the numerical grid, since with the two meshes the trend of the pressure is almost identical.

tank filling level

The comparison between the filling level predict by the CFD Model, implementing fine and coarse mesh, is summarized in table 7.8.

Figure 7.8 shows the trend of the filling level as a function of the time for the experimental test and the CFD Model, implementing coarse and fine mesh.

Analyzing both the table 7.8 and the figure 7.8, it can be noted that the filling level prediction for the CFD Model is not dependent by the numerical grid, since with the two meshes the trend of the pressure is almost identical.

Time (s)	Fine Mesh Filling Level (MPa)	Coarse Mesh Filling Level (MPa)
0	2.736	2.736
29.36	2.746	2.746
61.96	2.755	2.755
89.91	2.774	2.775
117.84	2.803	2.804

Table 7.8: Coarse vs Fine Mesh Filling Level for some time values.

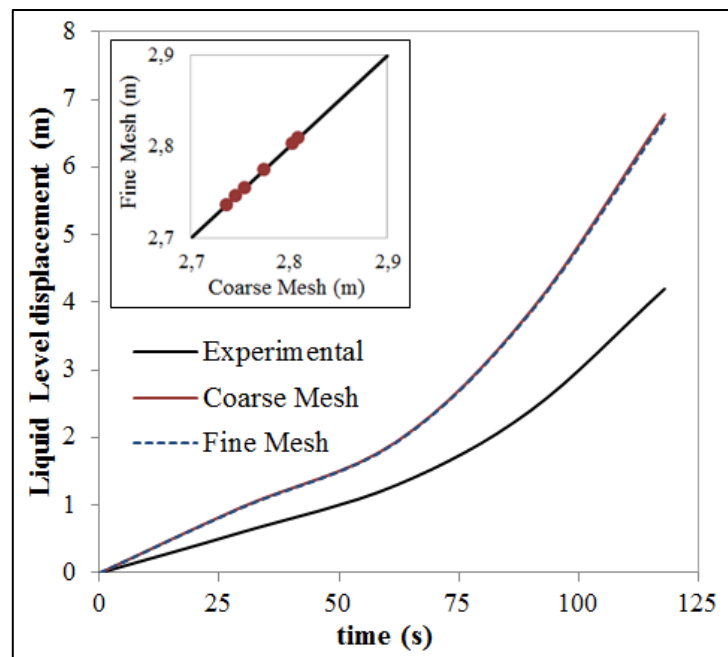


Figure 7.8: Experimental vs CFD Model (for Coarse and Fine mesh) filling level in function of the time.

PRV opening time

	PRV opening time (s)	Relative Error (%)	$\Delta t = t_{exp} - t_{CFD Model}$ (s)
<i>Experimental test</i>	132	-	-
<i>Coarse Mesh</i>	135.7	2.803	3.7
<i>Fine Mesh</i>	136.7	3.561	4.7

Table 7.9: Coarse vs Fine Mesh Pressure for some time values.

Table 7.9 shows the comparison between the PRV opening time predict by the CFD Model, implementing fine and coarse mesh. It is also reported the PRV opening time of the experimental test, highlighting the differences with the prediction of the CFD Model.

Finally, the results of the CFD Model are independent of the numerical grid carrying out a general evaluation of all the parameters involved. For this reason, in the following part of the work, a mesh with a number of elements and structural characteristics (minimum size, maximum size, quality, aspect ratio, etc.) similar to the coarse mesh previously defined will be used.

8. Model application and definition of case studies

In this chapter, model applications will be described. Two principal modelling analyses were carried out:

1. Sensitivity analysis in order to obtain simplified liquid thermal stratification models
2. Case studies for the industrial accidents simulation through the application of “advanced boundary condition”.

All these will be explained in detail in the following paragraphs.

8.1. Sensitivity analysis

In order to provide a sensitivity analysis for the CFD model, a series of case studies were implemented and analyzed. The aim of this part of thesis is to derive a parametric correlation for the determination of altered thermally liquid layer in function of some relevant parameters. These parameters are tank diameter, filling level, relative pressure of the tank with respect to the initial pressure, and incident heat flux on the tank’s walls.

To assess the height of the stratified layer (see figure 4.12) eighteen case studies were implemented by combining:

- 2 values of tank’s diameter: these values were chosen analyzing the size of the vessels used in the experimental tests reported in literature (see section 4.1.1.);
- 3 values of filling level;
- 3 values of flux heat to simulate the complete and uniform engulfment of a tank in a pool fire of low, medium and high intensity.

In all case studies, the equipment exposed to fire is a horizontal cylindrical tank containing pure propane as in a validation case.

As already said, to achieve the aim of the work, it was necessary to implement a large number of case studies. For this reason, the number of cells in the computational domain could not be very high, otherwise the computational time would be resulted very costly. However, to avoid convergence problems, it is necessary that the region near to liquid–vapour interface is very fine

and uniform. According with the previously considerations, for each filling level it was necessary to built a different mesh, with a number of cells and structural features similar to the mesh used in the validation case.

Being the vessel uniformly engulfed in the flames, it was possible to represent the domain as a semicircular 2D region. Table 8.1 shows the main features of the several meshes used: the tank diameter is 1.7 meters.

	Mesh 1 (F.L. = 0.9)	Mesh 2 (F.L.=0.7)	Mesh 3 (F.L.=0.5)
<i>Cell number:</i>	9750	11600	14800
<i>Min. cell size:</i>	1.44 mm	0.66 mm	0.55 mm
<i>Max cell size:</i>	18.61 mm	14.31	12.40 mm
<i>Orthogonal quality value:</i>	0.703–1 (average: >> 0.95)	0.782–1 (average: >> 0.95)	0.788–1 (average: >> 0.95)
<i>Maximum aspect ratio value:</i>	12.7	18.0	14.8

Table 8.1: Main features of the several meshes used for the sensitivity analysis.

Figure 8.1 shows the Mesh 1: its features are reported in table 8.1.

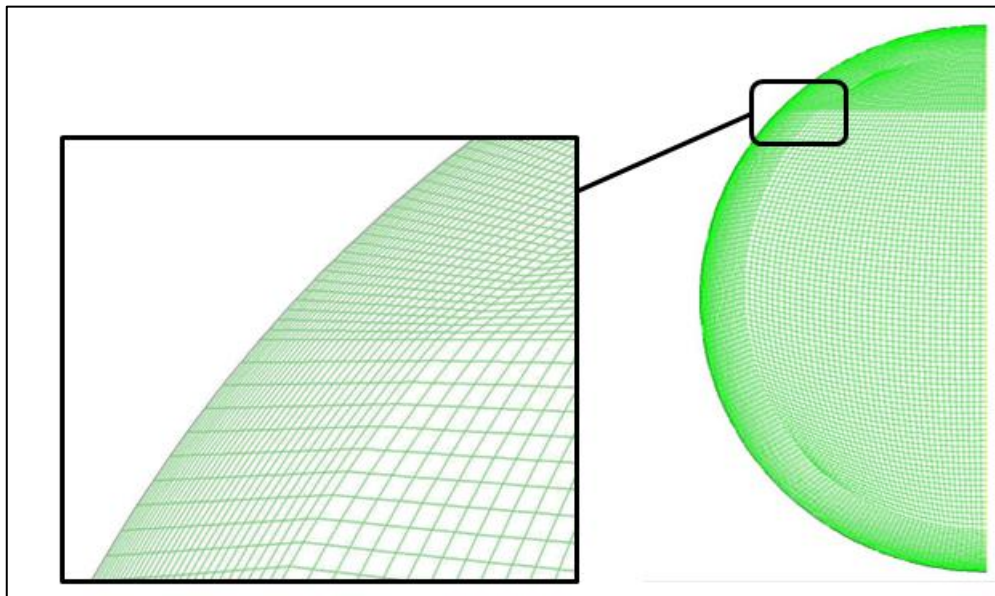


Figure 8.1: Calculation mesh adopted in the case studies for sensitivity analysis and detail of a portion of the domain representing boundary layer and liquid–vapour interface.

To obtain a mesh with a diameter different by 1.7 meters, it is necessary a process of scaling or unscaling into the CFD software. In this way, the mesh features do not change, except for the minimum and maximum cell size.

Table 8.2 shows all case studies implemented in the CFD model, by varying the geometry and the initial and boundary conditions.

CASES STUDIES FOR SENSITIVITY ANALYSYS OF LIQUID THERMAL STRATIFICATION			
<i>Item</i>	<i>Diameter (m)</i>	<i>Filling Level (vol. frac.)</i>	<i>Flux Heat (kW/m²)</i>
1	1.25	0.5	40
2	1.25	0.5	80
3	1.25	0.5	150
4	1.25	0.7	40
5	1.25	0.7	80
6	1.25	0.7	150
7	1.25	0.9	40
8	1.25	0.9	80
9	1.25	0.9	150
10	1.70	0.5	40
11	1.70	0.5	80
12	1.70	0.5	150
13	1.70	0.7	40
14	1.70	0.7	80
15	1.70	0.7	150
16	1.70	0.9	40
17	1.70	0.9	80
18	1.70	0.9	150

Table 8.2: Summary of case studies implemented in CFD Model for the sensitivity analysis.

Taking advantage of the transient nature, an analysis on the achievement of two values of absolute pressure was performed for each case studies. These values are the PRV set pressure in the Townsend's test (18.16 bar) and Droste's test (15.60 bar) [6]. In this way, it is possible to estimate the dependence of the height of the stratified liquid layer by the absolute pressure reached in the tank too.

These simulations were performed on the same windows machine used for the validation case: ASUS series N551J , with INTEL® CORE™ i7-4710HQ, CPU 2.50 GHz, 8 GB RAM and 64 bit operating system type. Parallel calculation was performed with four cores (eight threads), in order to obtain a computational time in the range 5–7 min to simulate 1 sec of real time, depending of the cells number constituting the numerical grid. The time step was set at value of 0.025s, in order to have a reasonable Courant number.

8.2. Case studies for advanced accidents simulation

This part of the work involves the application of CFD model for the simulation of possible “advanced industrial accidents”. In this case, it was analyzed a “domino scenario” that may occur in the storage park of an industrial site, in which both atmospheric and pressurized tanks are present. In particular, we considered a primary pool fire scenario, resulting from loss of containment of an atmospheric vessel, that is able to affect a neighbouring target, e.g. a pressurized vessel containing LPG. We applied integral fire models obtaining the incident flux heat on the wall of the target, placed at a certain distance from the flames. Such heat flow is not uniformly distributed all over the target, since it is affected by the view factor function of the position of the vessel. For this reason, it has been necessary to implement a “advanced boundary condition” through a subroutine.

8.2.1. Characterization of the industrial scenario

Figure 8.2 shows the layout of storage park in which the case study was located.

The primary accident comes from the spillage of the entire inventory stored in the atmospheric tank, that is placed near the pressurized vessel containing LPG, as indicated in Figure 8.2. The fluid releases is accumulated in the cath basin, then an ignition is supposed to occur triggering the pool fire. In table 8.3 are summarized the geometric and operative features of the atmospheric vessel, while table 8.4 shows the physical properties of the released hydrocarbon.

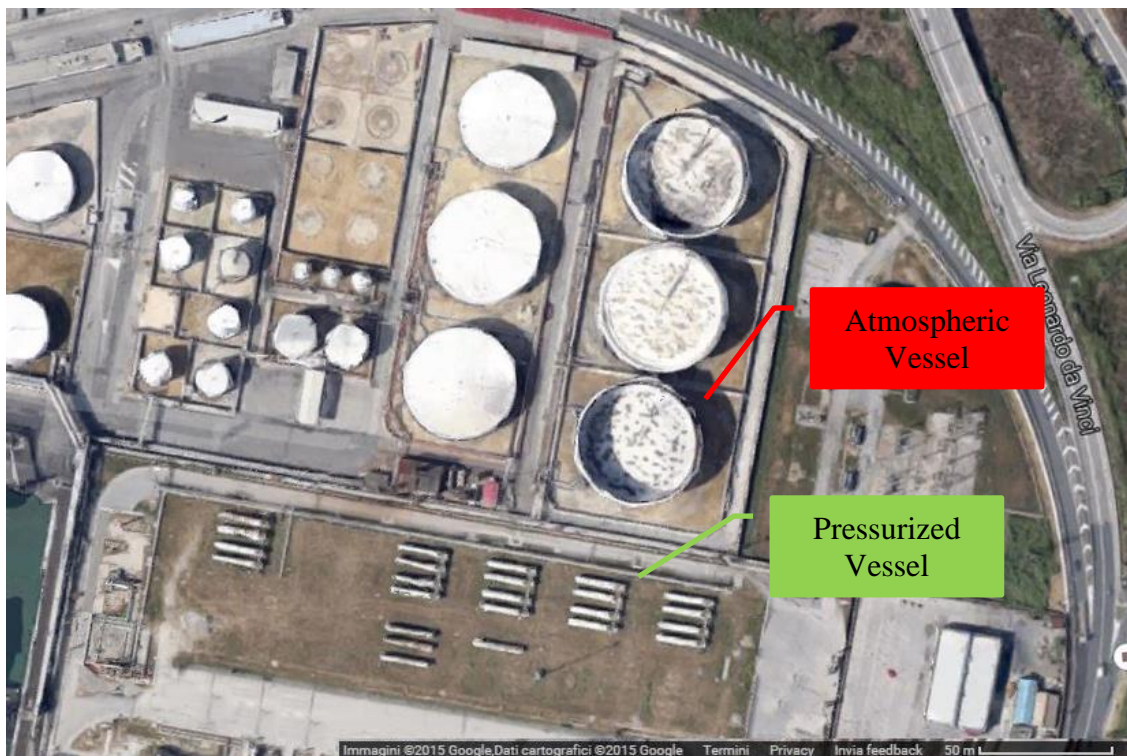


Figure 8.2: Storage park in a industrial site (adopted by source [67]).

Geometric features of the atmospheric vessel		
<i>Nominal diameter</i>	(m)	42
<i>Nominal height</i>	(m)	5.4
<i>Nominal Volume</i>	(m ³)	7500
Operational features of the atmospheric vessel		
<i>Filling Level</i>	(vol. frac.)	0.7
<i>Operational Volume</i>	(m ³)	5250
<i>Stored mass</i>	(ton)	3439
Geometric features of the containment dike		
<i>area</i>	(m ²)	3575
<i>X-size</i>	(m)	55
<i>Y-size</i>	(m)	65
<i>height</i>	(m)	1.5

Table 8.3: general features of the atmospheric vessel.

<i>Fluid</i>	(-)	n-hexane
<i>Liquid density ρ_L</i>	(kg m ⁻³)	655
<i>Heat of vaporization H_V</i>	(kcal kg ⁻¹)	87.5
<i>Heat of combustion H_C</i>	(kcal kg ⁻¹)	10780
<i>Molecular weight M_W</i>	(kg kmol ⁻¹)	86

Table 8.4: Physical properties of stored fluid in the atmospheric vessel.

Since the hexane is thermodynamically stable at the liquid state under atmospheric conditions, and due to the presence of the containment dike, this will form an evaporating confined pool.

The target, which is distant about 20 m from the containment dike, is represented by a horizontal cylindrical tank in which LPG is stored. The physical properties of LPG are approximate to those of pure propane and they are reported in table 6.2 (see sec. 6.1.2). A typical vessel geometry was assumed, based on the information available from the map of the storage park. Table 8.5 summarizes the features of the considered vessel [68].

Geometric features of the Target		
<i>Nominal diameter</i>	(m)	3.2
<i>Nominal length</i>	(m)	19.4
<i>Nominal Volume</i>	(m ³)	150
<i>Maximum thickness</i>	(mm)	27
<i>Distance bottom tank-ground</i>	(m)	0.48
<i>PRV set pressure</i>	(MPa)	1.8

Table 8.5: Geometric features of pressurized vessel [68].

8.2.2. Fire calculations for evaporating confined pools

In this paragraph calculation procedure to estimate flame dimensions and surface emissive power are provided. This procedure is typical of traditional steady state consequence assessment, and is widely known [1], [4]. Figure 8.3 shows various steps needed for fire calculations.

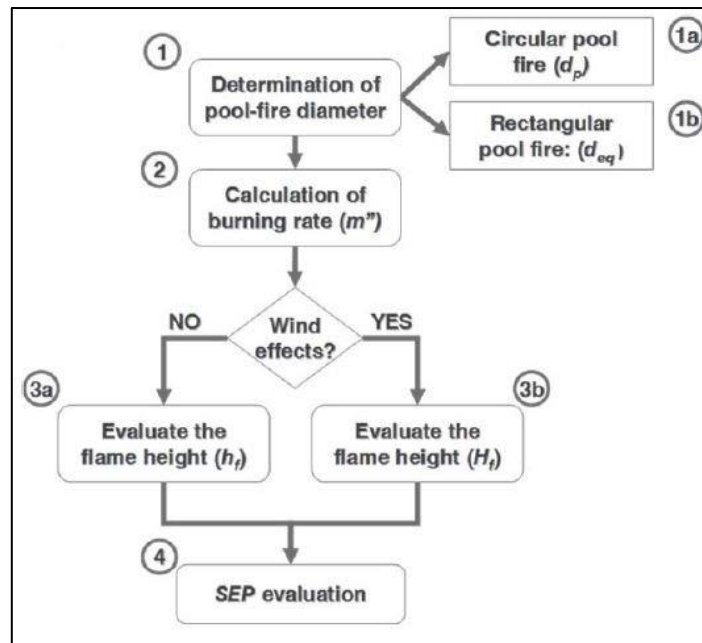


Figure 8.3: Step procedure for SEP evaluation [4].

Step 1: Pool equivalent diameter

First of all, fire dimension must be determined. They will be calculated from pool diameter, then the first thing that must be univocally determined is pool diameter. In case of confined pool, an equivalent diameter is defined as follows:

$$D_{eq} = \sqrt{4 \cdot \frac{A_{pool}}{\pi}} \quad (81)$$

Step 2: Burning rate

The *burning rate* m'' (kg/m² s) is defined as the rate of evaporation of material per unit surface on the pool. Pool diameter influences the burning rate only if it is lower than 1 m. Otherwise the burning rate depends only by the substance and it can be calculated as follows:

$$m'' = \frac{0.001 \cdot H_C}{H_v + c_p(T^0 - T_{atm})} \quad (82)$$

In which H_C and H_v (in J/kg) are respectively the heat of combustion and of vaporization at T_b (boiling temperature at ambient pressure of the liquid, in K); c_p is the average liquid heat capacity and T_{atm} is the ambient temperature (K). It is worth mentioned that, for a evaporating pool, pool temperature is equal to the atmospheric temperature: for this reason the second denominator term is 0.

Step 3: Flame Height and Diameter

Determining the geometry of the flame is crucial for both the evaluation SEP and of the view factor. Wind may strongly affect the pool fire geometry: it is then necessary to determine the scaled wind velocity u^* , defined as follows:

$$u^* = \frac{u_w}{\left(\frac{g \cdot m'' \cdot D_F}{\rho_a}\right)^{0.33}} \quad (83)$$

where u_w is the wind velocity at a height of 10 m, ρ_a is the air density and g is the gravitational acceleration.

In the case of High-wind situations (wind velocity higher than 1 m/s), wind effect must be taken in account, and another experimental correlation is used:

$$\frac{H_f}{D_f} = 55 \cdot \left(\frac{m''}{\rho_a \sqrt{g \cdot D_f}}\right)^{0.67} \cdot (u^*)^{-0.21} \quad (84)$$

In which H_f (m) is the flame height and D_f is the flame diameter, both reported in figure 8.4.

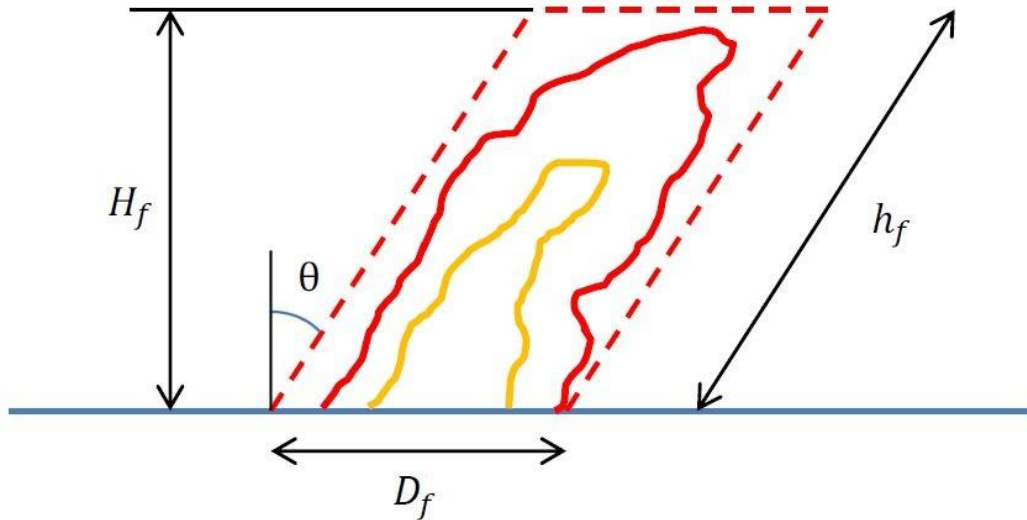


Figure 8.4: Schematization of a tilted pool fire (adopted from [4]).

The flame side length is then associated to the flame height as:

$$h_f = \frac{H_f}{\cos(\theta)} = H_f \cdot \sqrt{u^*} \quad (85)$$

Step 4: SEP evaluation

A rough estimation of SEP (surface emissive power, which indicates the heat radiated outwards per unit surface area of the flame in kW/m²) is given by the following correlations:

$$SEP_{th} = \frac{Q'}{A} \quad (86)$$

$$SEP_{max} = F_s \cdot SEP_{th} = \frac{F_s \cdot m'' \cdot H_c}{1 + 4 \cdot \frac{h_f}{D_f}} \quad (87)$$

in which F_s indicates radiation fraction (the amount of heat generated by the flame which is radiated), generally varying between 0.1 and 0.4 [4], and Q' is the heat generated by the combustion. However, this value does not take into account the presence of soot in smoky flames, which will be included in the following relation:

$$SEP_{act} = SEP_{max} \cdot (1 - \zeta) + SEP_{soot} \cdot \zeta \quad (88)$$

Where the typical value of SEP_{soot} is 20 kW/m² and ζ represents the soot fraction.

8.2.3. Heat flux at a distance from the fire: atmospheric transmissivity and view factor

The heat flux q (W/m²) at a certain distance from the fire, which is experienced by the target per unit area, can be calculated as:

$$q = SEP_{act} \cdot F_{view} \cdot \tau_a \quad (89)$$

in which F_{view} is the view factor and τ_a the atmospheric transmissivity. In this paragraph calculation procedure to estimate these parameters are explained.

Atmospheric transmissivity

The atmospheric transmissivity (τ_a) accounts for the fact that the emitted radiation is partly absorbed by the air between the radiator and the radiated object. The factor is equal to 1 minus the absorption factor, the values of which depends on the absorbing properties of the components of the air in relationship to the emission spectrum of the fire [4]. Since water vapour and carbon dioxide are the main absorbing components within the wave length area radiation, the following approximating expression can be given:

$$\tau_a = 1 - \alpha_w - \alpha_c \quad (90)$$

Where α_w and α_c are respectively the absorption factors for water vapour and carbon dioxide. They depend on the partial vapour pressure, path length X covered by the radiation (m), the radiator temperature and the ambient temperature. The partial vapour pressure of carbon dioxide in the atmosphere is normally 30 N/m^2 , while the partial vapour pressure of water depends always on the temperature and the relative humidity.

An exact calculation of τ is complicated. The absorption factor may be estimated from several figures and correlation. In this work, an approximation correlation is used [4]:

$$\tau_a = c_w \cdot (X \cdot P_w)^{-0.09} \quad (91)$$

in which the combustion of CO_2 is neglected and c_w is a constant ($2.02 \text{ (N/m)}^{0.09}$). this formula should be used only for calculations in the range between:

$$10^4 < X \cdot P_w < 10^6 \text{ N/m} \quad (92)$$

View factor

The geometrical view factor is the ratio between the received and the emitted radiation energy per unit area. The factor is determined by the flame dimensions and shape, and by the relative position and orientation of the receiving object.

Considering the infinitesimal representation in figure 8.4, the geometrical view factor is defined as follows:

$$F_{view_{dA_1, A_2}} = \frac{1}{\pi} \iint \left(\frac{\cos(\beta_1) \cdot \cos(\beta_2)}{x^2} \right) dA_2 \quad (93)$$

where x is the distance between the centers of dA_1 and dA_2 , β_1 is the angle of the normal vector to plane dA_1 and the line connecting dA_1 and dA_2 and β_2 is the angle of the vector to plane dA_2 and the line connecting dA_1 and dA_2 .

In general, simple flame shapes are taken for the calculations such as sphere, cylinder and flat plate. In case of pool fire, the view factor of a cylinder can be used. Since the previous correlation is complex, in this work it was used a simplified approach. This approach was developed by Raj [69] and it is specific for this type of scenario, in which a cylindrical tank is engulfed in a pool fire.

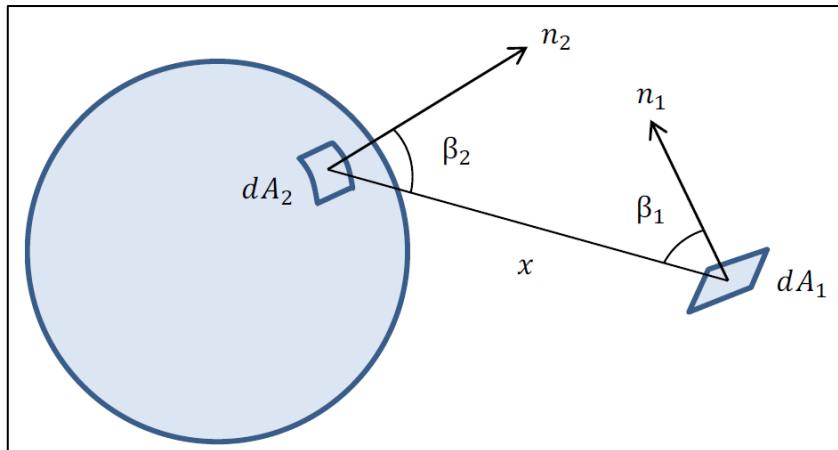


Figure 8.5: Schematization for view factor calculation (adopted from [4]).

Figure 8.6 shows, schematically, the relative geometrical positions and orientations of the pool fire and the cylindrical tank being irradiated. The parameter of interest is the estimation of view factor between the element surface on the tank and the fire. In a following discussion, simbology refers to the relative figure.

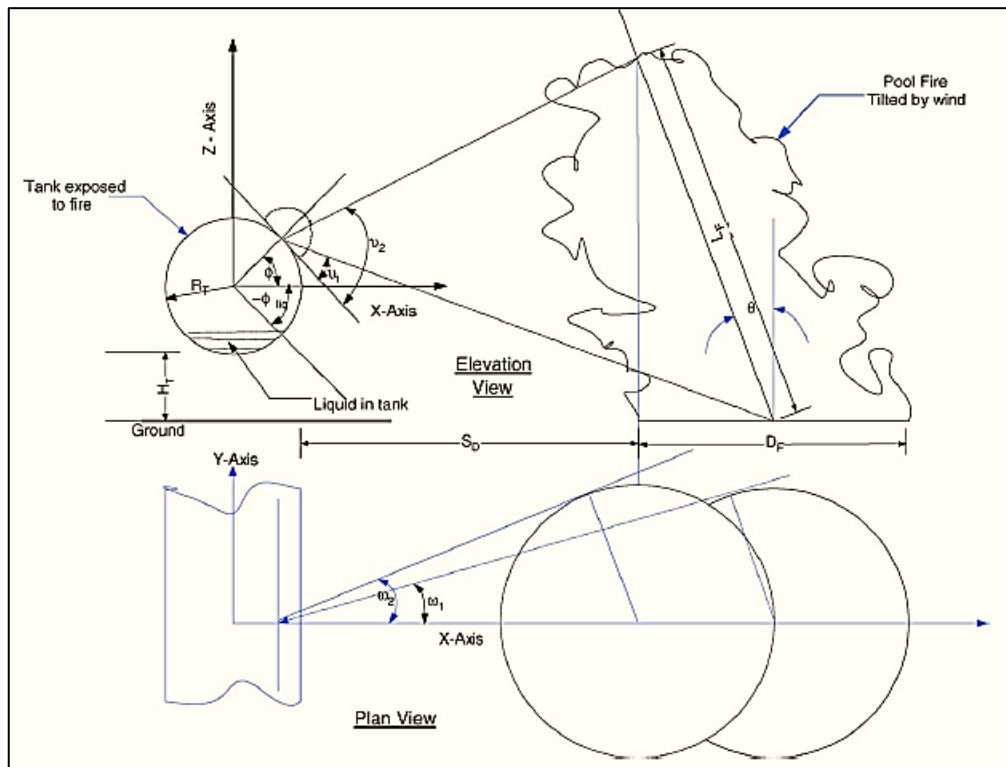


Figure 8.6: Sketch illustrating the relative positions of the fire, tank and the radiation receiving element on the tank surface and the various angles.

Referring to figure 8.5, the horizontal distance between the tank center and the center of the firebase is given by:

$$S = R_T + S_D + \frac{D_f}{2} \quad (94)$$

Assume a Cartesian coordinate system with the origin on the ground directly under the center of the tank. Let the coordinates of any point in space be represented by x-z, where x is the horizontal coordinate, y the coordinate along the axis of the tank and z is the vertical coordinate.

With the above convention, the elementar area at P has the following coordinates:

$$P(x, y, z) = P[R_T \cos(\phi), 0, \{H_T + R_T + R_T \sin(\phi)\}] \quad (95)$$

The coordinate of the center of fire on the base is:

$$M(x, y, z) = M[S, 0, H_F] \quad (96)$$

the coordinate of the top center of fire on the axis is:

$$N(x, y, z) = N[\{S + L_F \sin(\theta_F)\}, 0, \{H_F + L_F \cos(\theta_F)\}] \quad (97)$$

Considering a hemisphere of unit radius drawn at the location of the elementar surface on the wall of the tank. The hemisphere is aligned such that its base plane forms the tangential plane to the tank surface at the location of the elementar area of interest.

The distance PM from the center of the unit hemisphere on the wall element and fire axis at the pool (firebase) is given by:

$$PM = \sqrt{\left[\{S - R_T \cos(\phi)\}^2 + \{H_f - (H_T + R_T + R_T \sin(\phi))\}^2 \right]} \quad (98)$$

The distance PN to the top of the fire is given by:

$$PN = \sqrt{\left[\{S + L_f \sin(\theta_F) - R_T \cos(\phi)\}^2 + \{(H_f + L_f \cos(\theta_F)) - (H_T + R_T + R_T \sin(\phi))\}^2 \right]} \quad (99)$$

Therefore, the angles subtended by the tangent to the fire base circle (ω_1) and the fire top circle (ω_2) at the center of the unit hemisphere are given by:

$$\omega_1 = \tan^{-1} \frac{R_f}{PM} \quad (100a) \quad \& \quad \omega_1 = \tan^{-1} \frac{R_f}{PN} \quad (100b)$$

It can also be shown that:

$$\cos(v_2 - v_1) = \frac{PN^2 + PM^2 - L_f^2}{2 \cdot PM \cdot PN} \quad (101)$$

where

$$v_2 = \left[\frac{\pi}{2} - \phi \right] + \sin^{-1} \left[\frac{\{H_f + L_f \cos(\theta_F)\} - \{H_T + R_T + R_T \sin(\phi)\}}{PN} \right] \quad (102)$$

Note that:

- If $v_1 < 0$, set $v_1 = 0$;
- If $v_2 > \pi$ set $v_2 = \pi$;
- If $v_2 < v_1$, $F_{view} = 0$.

Finally, the overall view factor between the element (dA) and the fire is:

$$F_{dA \rightarrow Fire} = \frac{1}{\pi} [\sin(\omega_1) + \sin(\omega_2)] \cdot [\cos(v_1) + \cos(v_2)] \quad (103)$$

8.2.4 Pool fire results and “Advanced Boundary Condition”

Through a iterative procedure, it is possible to estimate the view factor between the elements on the wall of the tank and fire, and then, flux heat incident on each point of the wall. Before to calculate flux heat incident on the tank wall, it is necessary to estimate SEP and the pool fire dimensions. For this assessment, the following hypothesis are carried out:

- $5D^1$ as weather conditions are assumed;
- The radiation fraction F_s is 0.3 [4];
- The flame is luminous, in order to simulate the most serious scenario. In this case SEP_{act} is equal to SEP_{max} .

¹ Neutral stability class and wind speed at 10 m height of 5 m/s.

Table 8.6 shows the results of pool fire obtained through the step procedure described in figure 8.2. To assess effectiveness of this predictions, results are compared with those obtained through the implementation of previous scenario in a lumped code: DNV® Phast ® 6.4 software.

POOL FIRE RESULTS		
<i>item</i>	<i>Simplified correlations</i>	<i>DNV® Phast ® 6.4</i>
m'' ($kg\ m^{-2}\ s^{-1}$)	0.1232	0.0997
$d_{eq} = D_f$ (m)	67.47	67.47
u^* ($m\ s^{-1}$)	1.26	-
H_f (m)	84.96	-
h_f (m)	95.35	87.34
θ (deg)	27.00	39.85
SEP ($kW\ m^{-2}$)	250.55	249.92

Table 8.6: Pool fire results obtained with simplified correlations and DNV® Phast® 6.4.

The difference between two types of results are mainly due to the difference value of “burning rate” used, but the order of magnitude is the same: for this reasons, the application of both pool fire results will provide the same effects on the target.

The value of atmospheric transmissivity is approximately considered the same for each element on the wall of the vessel. Through the application of the correlation reported in eqs. 9 and considering a relative humidity of 50%, it is about of 0.795.

The aim of this part of thesis is to implement a flux heat boundary condition, in order to simulate a real scenario, limiting the approximations. Consequently, for the calculation of view factor, the correlation reported in eqs. 103 was used. In this way, ranging angle ϕ (angle between the normal to the generic element P and axis-x) between 0° and 360° , it is possible to estimate view factor and then flux heat incident in each point of the wall of the tank.

Table 8.7 shows view factor and flux heat results for a large number of angle ϕ values. It is 0 if the normal to the generic element P is along axis-x, 90 is the normal to P is along axis-z and 180 when the normal to P is in the opposite direction with respect to axis-x.

Analyzing results, it is observed that, for angle ϕ ranging between 180° and 270° , the flux heat incident on the walls is zero. In fact, that part of tank does not view the flame.

To evidence that the estimation of the heat flux, carried out through the above correlations, is reasonable, the fire scenario was simulated also through DNV® Phast® 6.4 software. In figure 8.7

is shown the distance at which a certain level of intensity radiation intensity may impact. It is observed that, in zona where the pressurized vessels is placed, this can be up to 100 kW/m^2 .

<i>angle</i> ϕ (deg)	<i>view factor</i> F_w	<i>flux heat incident on the univocal element</i> q (kW/m ²)
0	0.291	57.91
30	0.381	75.90
45	0.386	76.87
60	0.363	72.33
90	0.244	48.57
120	0.105	21.01
135	0.054	10.70
150	0.018	3.65
180	0	0
210	0	0
225	0	0
240	0	0
270	0	0
300	0.037	7.41
315	0.083	16.57
330	0.144	28.72

Table 8.7: Effects of primary pool fire on the target equipment.

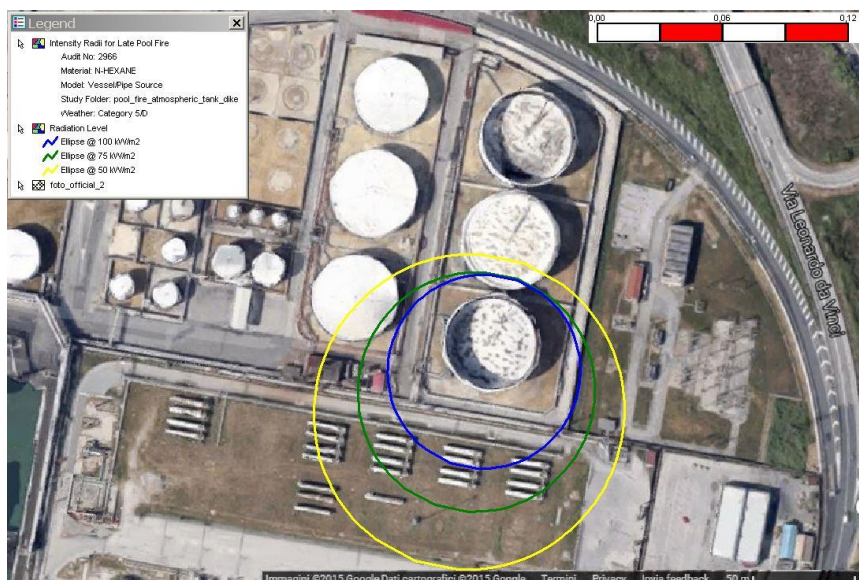


Figure 8.7: Radiation intensity for pool fire obtained through DNV® Phast® 6.4 software.

Once analyzed the industrial accident scenario, it is necessary to implement the resulting flux heat to the pressurized vessel containing LPG, object of the CFD simulation. To provide a different flux heat (in kW/m²) values for each spatial coordinate of the wall of the tank, a subroutine was built. For the construction of this UDF, the heat flux values, reported in table 8.7 and shown in figure 8.8 were used. In figure 8.8 the pool fire is positioned on the right side of the tank.

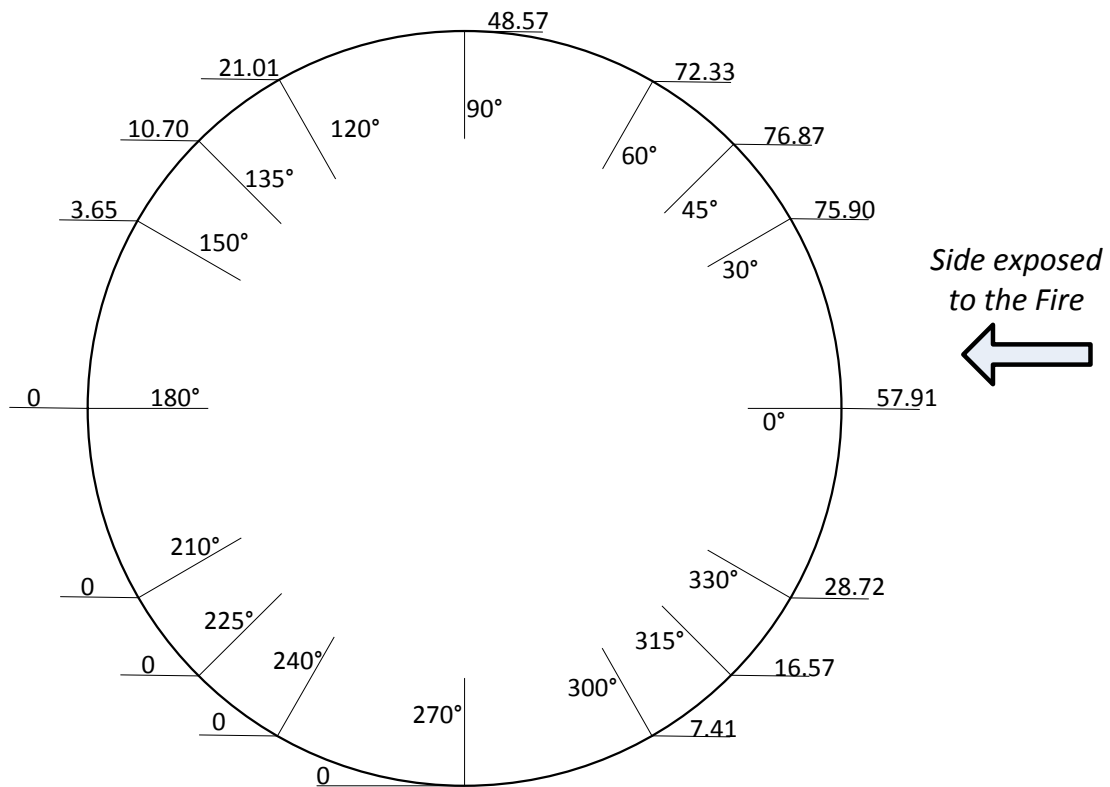


Figure 8.8: Schematization of flux heat incident on the wall of the tank.

Since the calculation of flux heat per unit degree would have been too heavy for the compilation in the CFD model, a flux heat linearization was carried out. Subroutine built to provide these “advanced and specific boundary conditions” is reported in appendix 3.

8.2.5. CFD model simulations to reproduce the industrial accident

This type of analysis differs from the previous one focused on sensitivity analysis mainly for two aspect:

- Implementation of “advanced fire conditions”, widely argument in the previous paragraphs.

- Aspect related to the development of advanced computational mesh, as described in Chapter 6.

In this case, the engulfment conditions are not total and homogeneous over all the target. The numerical grid can be maintained 2D, but the geometric representation have to be circular, since the heat flow incident on the walls depends by exposure to the flames. The advanced grid described in Section 6.3 as adopted.

The model set up, both theoretichal and numerical aspects, it was described in chapter 6 of present work. The geometric features of target are reported in table 8.5 (see sec. 8.2.1), while the operational conditions (pressure and temperature) are the same of sensitivity analysis.

Two situations were considered, in order to assess the different behaviour of tank as a function of liquid filling level. Case–studies are so identified:

- case study “a”: high liquid filling level (set up 90%);
- case study “b”: medium liquid filling level (set up 75%).

It was decided to not consider a lower filling level because, the stratification effects would have been less marked.

Parallel calculation was performed with thirty–two threads, in order to obtain a computational time about of 60 min to simulate 1 sec of real time. The time step was set at value of 0.005 sec, in order to have a reasonable Courant number. This restriction is due to the small cell size.

9. Results and discussion

9.1. Sensitivity analysis and simplified stratification model

In this section, the results of the sensitivity analysis on the CFD model are reported in order to provide a deeper understanding of the liquid thermal stratification, obtaining a simplified correlation.

9.1.1. CFD simulation results

The case studies defined in Section 8.1 (see Table 8.2) allowed to perform a sensitivity analysis on the CFD model. For the sake of brevity, only the results showing relevant thermal stratification effects are discussed in detail.

The reference case–study is identified through the item “16”, where a high filling level (90%), an engulfment in a pool fire of low intensity (40 kW m^{-2}) and a diameter of 1.7m were considered. In order to assess the evolution of liquid stratification as a function of the relevant parameters, it is necessary to report the results of several simulations, where, compared to the reference case–study, the filling level, the heat flow and the diameter varies. For this reason, the results of case studies, identified through the item “7”, “10”, “16” and “17”, will be shown.

Figure 9.1 shows the results obtained in the analysis of case–study “16”, which it is a reference case–study.

Figure 9.1a shows the liquid temperature distribution at the beginning of the fire exposure (after 30 s). For the sake of clarity, the temperature of the vapour phase is not reported, in order to show the contours of liquid thermal stratification. As expected, the liquid stratification only occurs in a thin layer, in the proximity of the vapour–liquid interface. The thickness of the altered layer is of about 4 cm, with temperatures ranging between 303 and 325 K, while more than half of the liquid in the vessel is almost at its initial temperature (between 296 and 298 K). In this figure is also visible the thermal boundary layer that is formed near to the vessel wall exposed to fire, which results in the liquid recirculation to the hot upper layer.

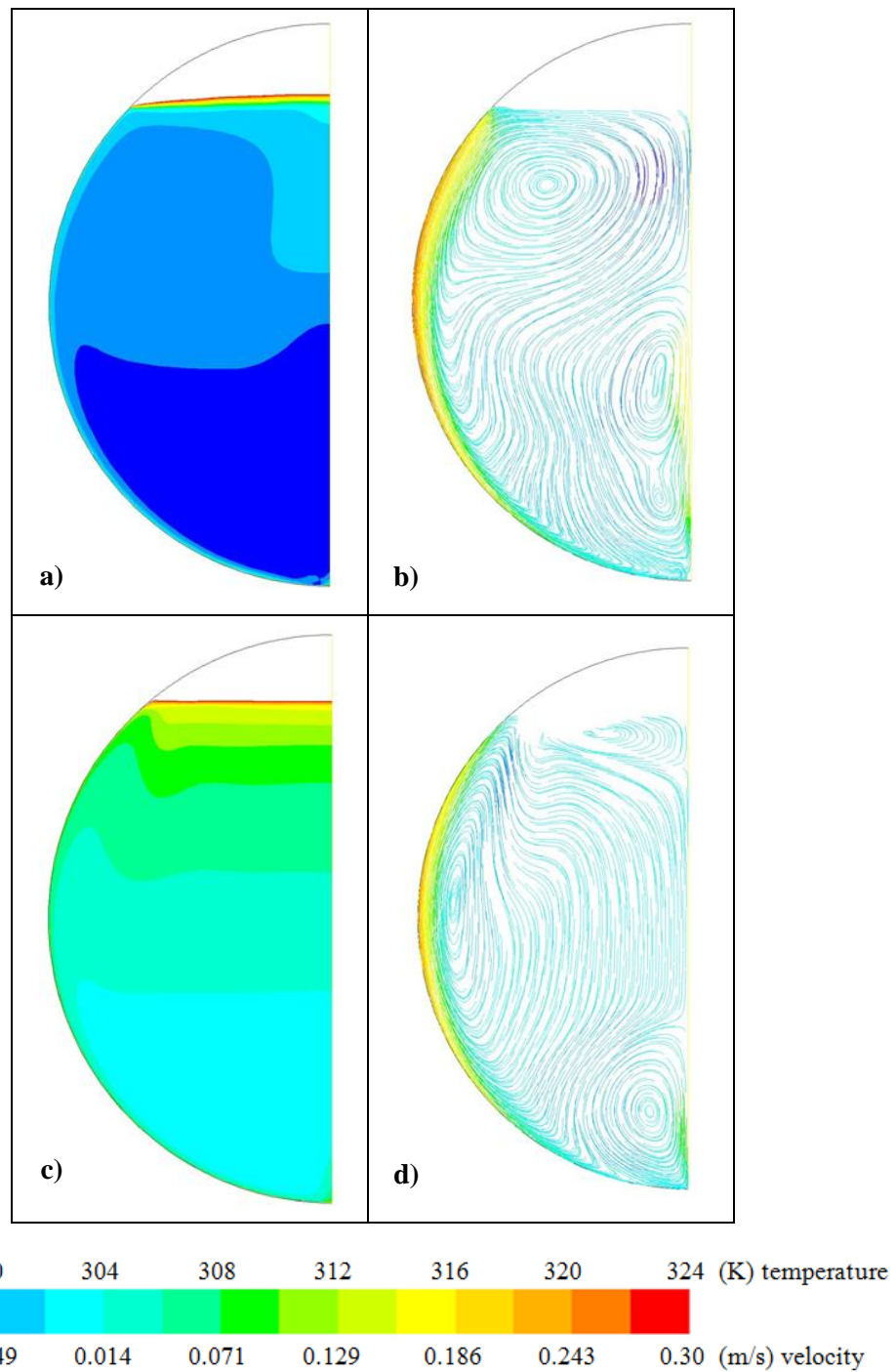


Figure 9.1: Results for case study “16”: temperature profile (K) at 30 s (a) and 120 s (c); axial velocity profile (m/s) at 30 s (b) and 120 s (d). PRV opening time is 131.7 s.

In figure 9.1b is shown the axial velocity profile, which confirms the previously assertion. It is clearly visible that, while the liquid in contact with the wall reaches the upper hot layer, the cooler liquid moves downward, accumulating in the sub-cooler bulk, in which the temperature ranges

between 296 and 302 K. Thus, an extremely low temperature gradient is present in the bulk: it is of about 3–4 K/m along the vessel vertical axis. The analysis of the figures 9.1a and 9.1b highlights

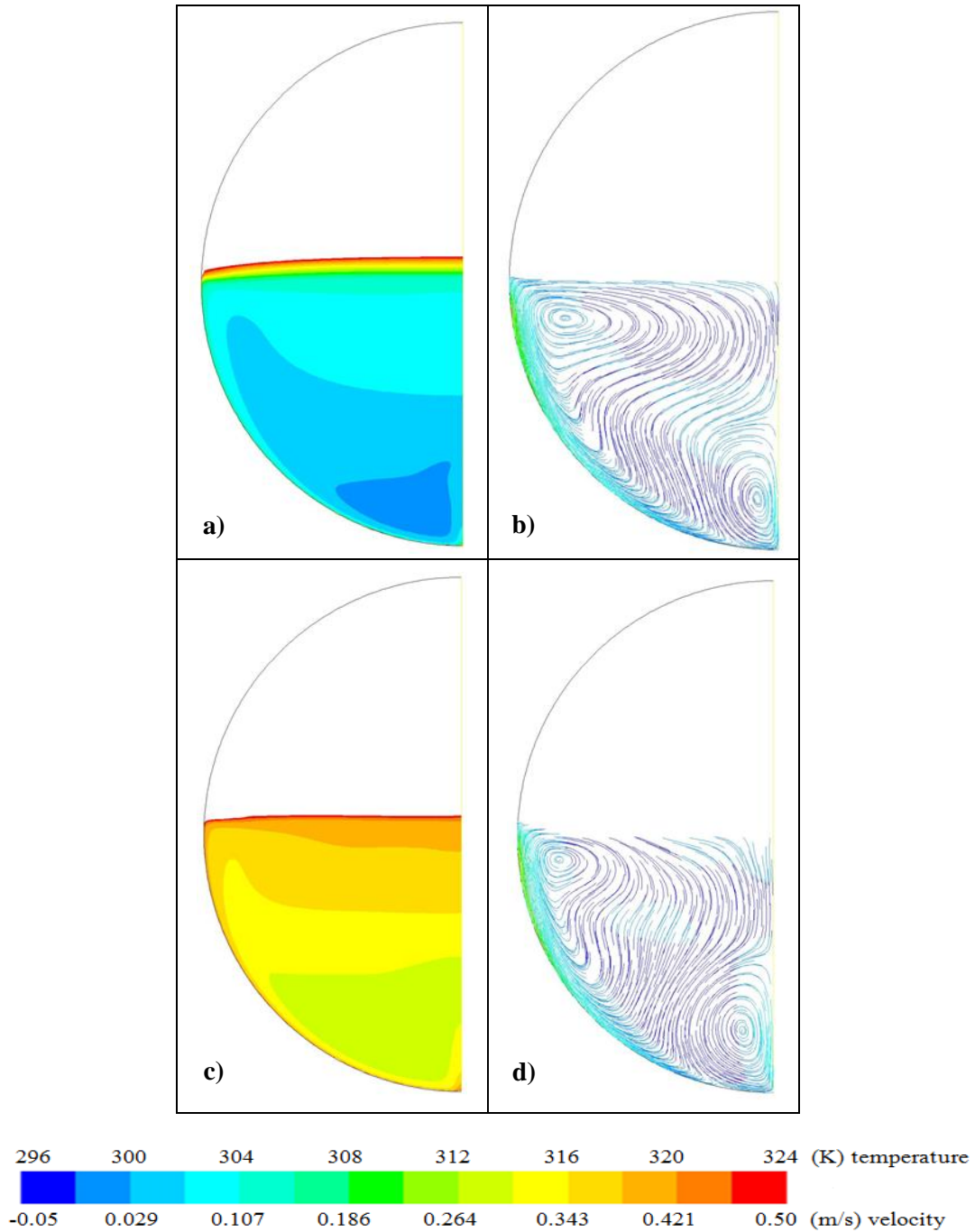


Figure 9.2: Results for case study “10”: temperature profile (K) at 60 s (a) and 180 s (c); axial velocity profile (m/s) at 60 s (b) and 180 s (d). PRV opening time is 184.5 s.

The liquid stratification appears in a bigger portion of the liquid with respect to case–study “16”. In fact, after 60 s of fire exposure (see figure 9.2a), the thickness of the altered layer is of about 10

cm, with temperatures ranging between 305 and 325 K: this corresponds to a average temperature gradient of about 200 K/m along the vessel vertical axis. Figure 9.2b shown that that upper part of the vessel is characterized by the formation of the same type of recirculation phenomena obtained in case–study “16”, but with higher velocities due to the small volume of the liquid phase. This also leads to a hotter bulk, in which the temperatures ranging between 299 and 305 K. Moreover, with respect to previously case–study, an higher temperature gradient is present in the bulk: it is of about 10 K/m along the vessel vertical axis. Figure 9.2c shows that, after 180 s of fire exposure, a homogeneous temperature distribution is present all over the liquid phase. The overall temperature gradient is as low as 15 K/m and the temperature ranging between 313 and 320 K. Only a very thin layer of about 4-5 cm is placed in the proximity of the liquid–vapour interface. Figure 9.2d shows the decreasing of liquid velocity in bulk, due to the lower temperature and density difference. Then, for a low filling level, the liquid thermal stratification is less significant with time. Finally, case–study “10” demonstrates the increasing the pressure is strongly affected by the filling level. In this case, PRV set pressure is reached after 184.5 s since fire exposure: in case–study “16”, in which more filling level were considered, this time is of 131.7 s.

Figure 9.3 shows the results obtained in the analysis of case–study “17”, where more severe fire conditions, resuting in a higher heat flow (80 kW m^{-2}) with respect to the reference case–study, are considered. The other relevant parameters were the same of the case–study “16”.

Figure 9.3a shows that, in a few seconds (after 15 s), a thin altered thermally layer is formed in the proximity of vapour–liquid interface. The thickness is approximately equal to that of the reference case–study, but the temperature gradient is higher (about 300 K/m), due to the high amount of heat flow absorbed by the liquid. Also in this case, the liquid bulk remains sub–cooler in a temperatures ranging between 296 and 302 K. Figure 9.3b shows, with respect to the case–study “16”, an increasing of the axial velocity on both along the hot walls and in the central region. This occurs because the heat flux causes an acceleration of natural convection mechanism: consequently, the thermal stratification is achieved after a much shorter time. This last assertion is confirmed by figure 9.3c, since, after 45 s, a pronounced liquid stratification is present. The thickness of the altered layer is approximately equal to that of the reference case–study (about 20 cm) but the liquid bulk is more hotter (between 300 and 308 K), since the liquid absorbs a higher heat flux than to the reference case–study. Figure 9.3d shows that the recirculation velocities are important up to the achievement of the PRV set pressure. This occurs after 51.5 s since fire start: less than half of the time required in case–study “16”, in which less severe fire conditions were considered.

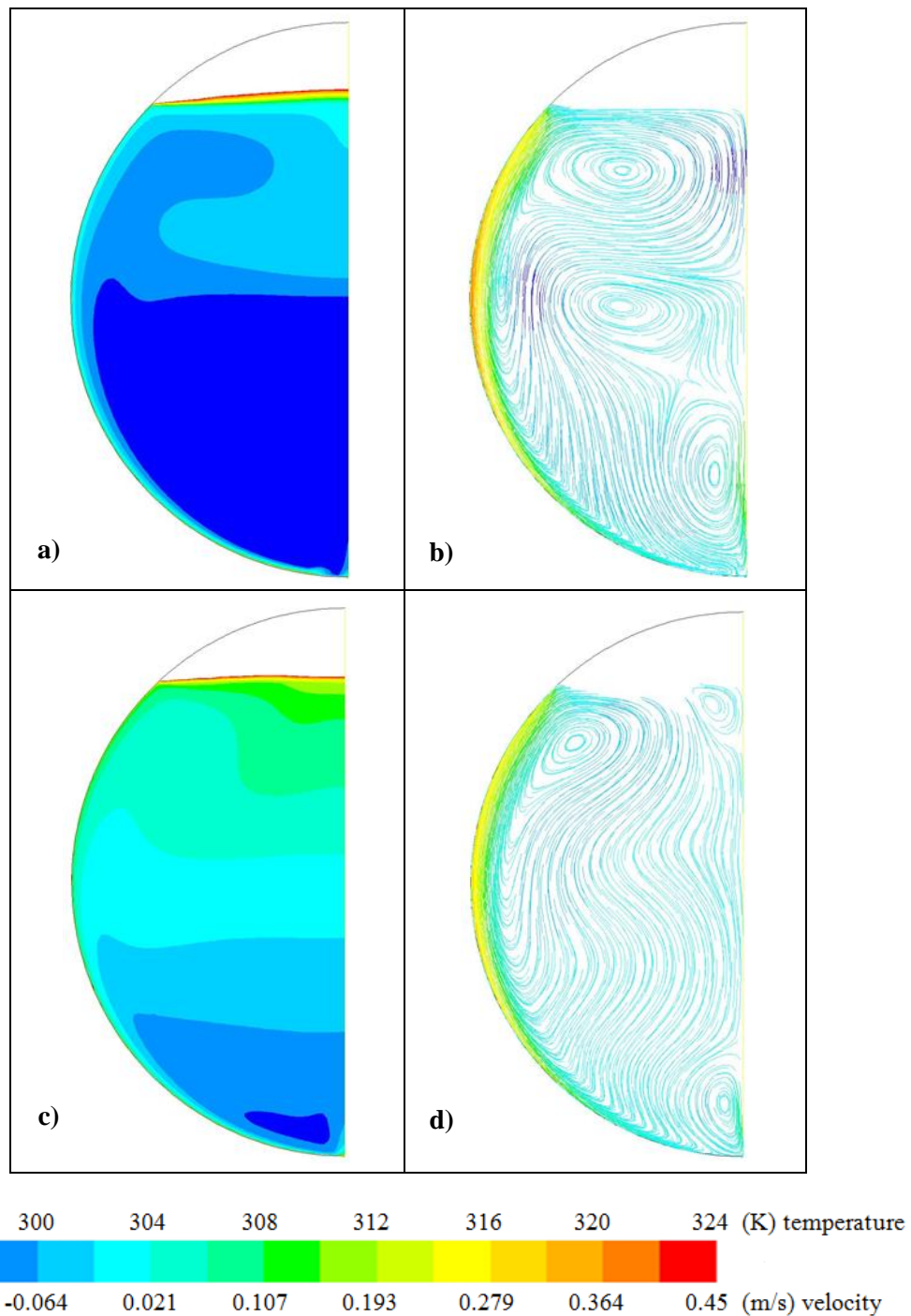


Figure 9.3: Results for case study “17”: temperature profile (K) at 15 s (a) and 45 s (c); axial velocity profile (m/s) at 15 s (b) and 45 s (d). PRV opening time is 51.5 s.

Finally, figure 9.4 shows the results obtained in the analysis of case–study “7”, where a small diameter (1.25 m) with respect to the reference case–study, are considered. The other relevant parameters were the same of the case–study “16”.

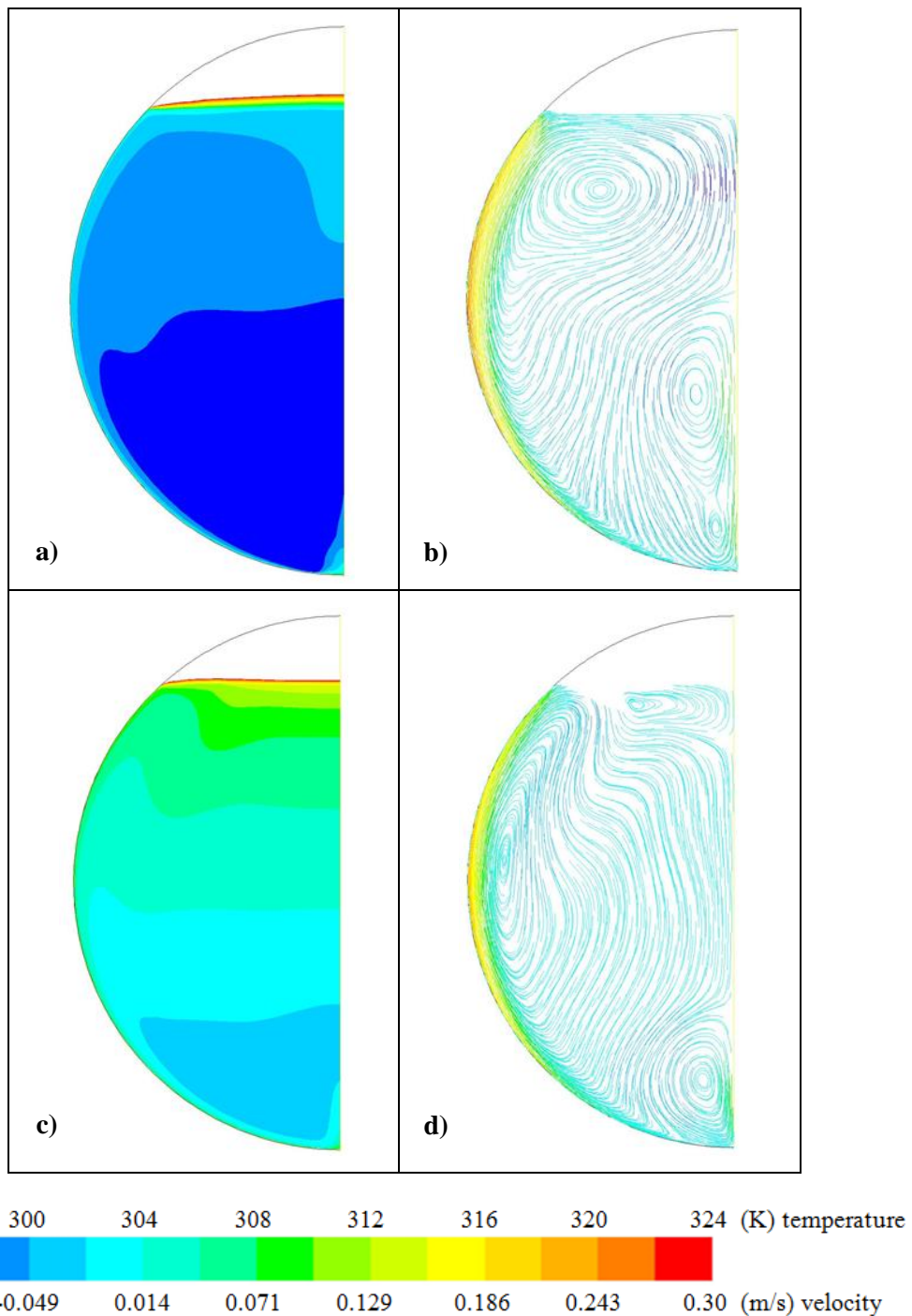


Figure 9.4: Results for case study “7”: temperature profile (K) at 20 s (a) and 80 s (c); axial velocity profile (m/s) at 20 s (b) and 80 s (d). PRV opening time is 90.0 s.

By carrying out a comparison between the figures 9.4 and 9.1, it can be noted that the trends of the temperature profile and axial velocity profile are identical. The only difference is the temperature range in the bulk. The ratio between the tank surface area and the stored liquid in the vessel for the case–study “7” is greater than that of the reference case–study: consequently, amount

of heat received by a unit volume of the liquid is also greater. This causes an increase of the bulk average temperature and a more pronounced liquid stratification. Furthermore, with respect to the response of the tank, the effect of a diameter reduction is the same of a increase of heat flow, as for the case–study “17”. This implies that the achievement of the PRV set pressure occurs more rapidly by reducing the tank size. In this case, the PRV set pressure is reached after 90 s since fire exposure.

9.1.2 Discussion

The results obtained show the importance of the dynamic liquid temperature profiles in a vessel exposed to fire and their influence on the internal pressure build–up. To highlight this issue, the stratification index, Π , defined by Birk et al. [13], was evaluated post–processing the CFD results. The stratification index can be defined as follows:

$$\Pi = \frac{P_{vessel}}{P^0(T_{liq,aver.})} \quad (104)$$

Where P_{vessel} is the vessel internal pressure at a given fire exposure time and P^0 is the saturation pressure calculated at the average liquid temperature.

In presence of stratification, the Π value is always major than 1, since pressure in the vessel is controlled by the warmest liquid layer. The saturation pressure at the average lading liquid phase temperature is greatly less than the saturation pressure at the temperature of the warmest liquid layer.

Figure 9.5 shows the comparison among Π , internal pressure (P) and average liquid temperature ($T_{L,av}$) calculated, respectively, for the case–study “16” (figure 9.5a), case–study “10” (figure 9.5b), case–study “17” (figure 9.5c) and case–study “7” (figure 9.5d).

As shown in figure 9.5, the dynamic pressure behaviour is characterized by an irregular growth. This is due to the transient effect associated to the different thermal inertia of liquid and vapour phases. In fact, the liquid at the interface needs time to heat up and to reach saturation conditions, thus delaying the pressure growth inside the vessel.

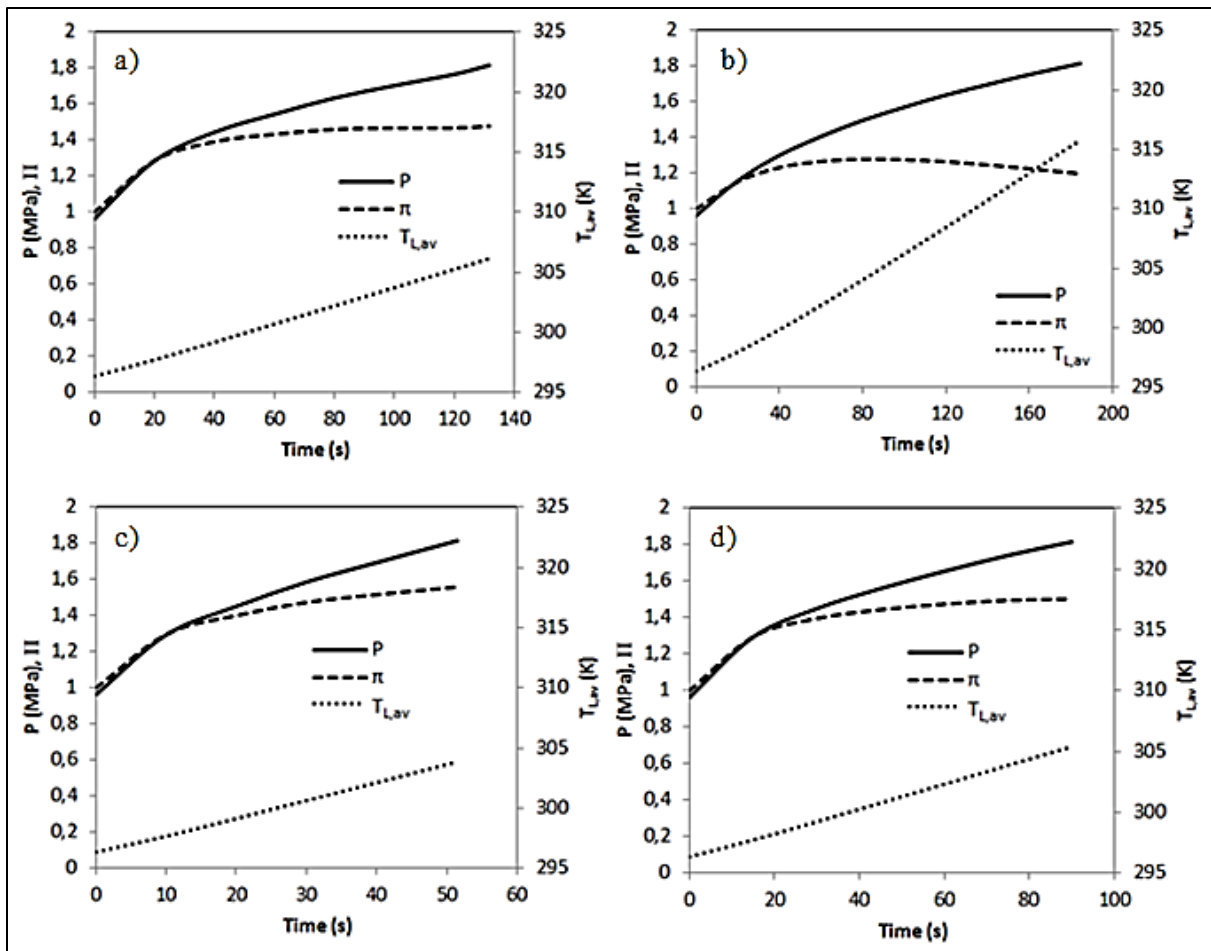


Figure 9.5: Average liquid temperature ($T_{L,av}$), pressure (P) and dynamic stratification index (II) for: (a) reference case; (b) case-study “10”; (c) case-study “17”; (d) case-study “7”.

Figure 9.1b shows as, by reducing the volumetric liquid filling level from 90 to 50%, a significant difference in the stratification behaviour is predicted. After a little time, the stratification index is reduced significantly, due to the gradual and slower vessel pressurization. For this reason, after reaching a maximum point, II index tends to decrease. Hence, in the latter case, stratification is less pronounced and the liquid is more homogeneous due to the lower thermal inertia of the system, characterized by a lower liquid hold up with respect to the reference case. Finally, the gradual pressurization causes also PRV opening time much higher than in the other cases considered and an increase more marked of the average liquid temperature.

Therefore, for higher liquid filling levels, the stratification has a more relevant effect on internal pressure increase. The results show that for high hold up values, the internal pressure is related to the temperature of the upper warm liquid layer rather than to the average bulk temperature. In

case–study “17”, this effect is more pronounced, since the fire heat load is double with respect to the reference case.

By comparing figure 9.5a and 9.5c, it is possible to see that, while in the reference case in the final part of the simulation, the stratification index decreases to a constant plateau, in the case–study “17”, where more severe fire conditions are considered, the index increase up to PRV opening time.

Figure 9.5d shows that the tank diameter does not affect on the liquid stratification, but the tank size reduction influences the dynamic pressure behaviour. In fact, for the reasons mentioned in the presentation of results, a reduction of diameter causes a faster achievement of the PRV opening time.

Finally, it is worth mentioned that the simulations allowed investigating the behaviour of the liquid in the vessel until the PRV opens. After the PRV opening, strong recirculation and mixing phenomena take place, associated to vessel depressurization and to the vent of the fluid through the PRV.

9.1.3. Parametric correlation

To estimate as accurately as possible the height of altered thermally liquid layer was necessary to choose a criterion through which the liquid domain is splitted into two nodes: the bulk and the stratified layer (as reported in figure 4.11). The choice was based on the parameter that describes the thermal stratification phenomenon: the dimensionless parameter Π (defined in section 9.1.2).

In a generic instant, the CFD code can provide the value of the average liquid temperature. By correlating the temperature with the saturation pressure through a polynomial function and setting the value of the Π , it is possible to derive the value of the liquid temperature at which to carry out the splitting of the liquid domain.

In the present work the parameter Π was set at 1,05: this entails that the splitting temperature of the liquid domain into two nodes is approximately 2°C–2,5°C higher than the average liquid temperature.

In table 9.1 the results obtained implementing the case studies in the CFD Model are summarized. In the representation, with A and B they are indicated the results of the case studies respectively for pressure in the vessel of 18.16 bar and 15.60 bar.

<i>Item</i>	$T_{liq. aver.}$ (K)	$T_{liq. strat}$ (K)	$h_{CFD Model}$ (m)
1-A	315.05	317.41	0.1298
1-B	305.66	307.79	0.1073
2-A	312.93	315.25	0.202
2-B	304.9	307.01	0.1947
3-A	313.03	315.55	0.2575
3-B	305.92	308.06	0.3012
4-A	311.31	313.59	0.1787
4-B	303.72	305.79	0.1709
5-A	309.35	311.58	0.2806
5-B	303.08	305.13	0.259
6-A	308.81	311.03	0.3599
6-B	303.02	305.07	0.3648
7-A	305.42	307.54	0.2568
7-B	300.93	302.92	0.2619
8-A	303.7	305.77	0.3511
8-B	300.43	302.4	0.3471
9-A	303.57	305.64	0.4665
9-B	300.53	302.51	0.4198
10-A	315.72	318.11	0.1556
10-B	306.23	308.38	0.1354
11-A	313.29	315.61	0.2515
11-B	305.37	307.49	0.2416
12-A	312.51	314.82	0.3204
12-B	305.51	307.64	0.3587
13-A	312.32	314.62	0.2215
13-B	306.06	306.14	0.2257
14-A	309.73	311.97	0.3511
14-B	303.23	305.29	0.382
15-A	308.95	311.17	0.4546
15-B	303.22	305.28	0.4491
16-A	306.11	308.25	0.3377
16-B	301.07	303.06	0.3187
17-A	303.88	305.96	0.4429
17-B	300.5	302.47	0.45
18-A	303.42	305.48	0.5649
18-B	300.48	302.45	0.6005

Table 9.1: Summary of the case studies results for the liquid stratification analysis.

Once the results of the case studies implemented in the CFD Model were obtained, the focus was shifted on the development of the relationship to estimate the height of the stratified liquid layer.

The aim was to formulate a dimensionless correlation with which the parameter h_1/D can be derived, where h_1 and D represent respectively the thickness of altered thermally liquid layer and the tank's diameter. To choose the type of correlation has been preliminary necessary to evaluate the trend of parameter h_1/D as a function of the variables involved.

Figures 9.6 and 9.7 show the trend of this parameter as a function respectively of the filling level and the heat flux incident on the wall, obtained by fixing the other parameters in play. It can be seen that the h_1/D increases about linearly with increasing filling level and heat flux.

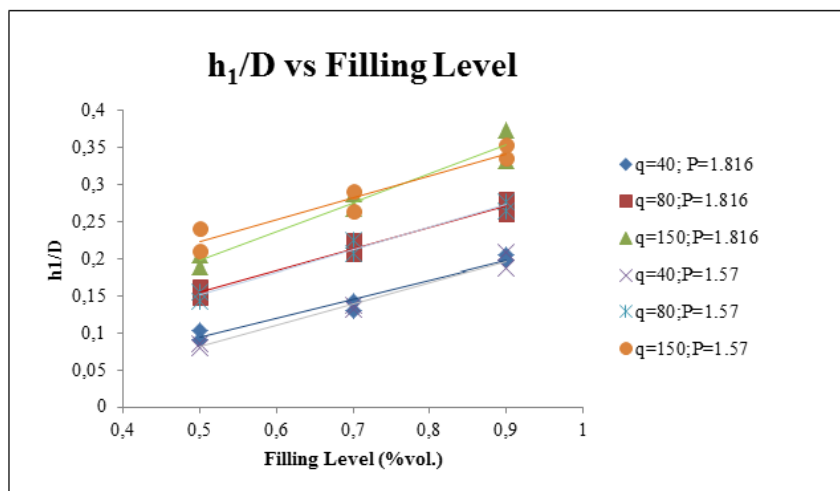


Figure 9.6: Trend of the parameter h_1/D as a function of Filling Level.

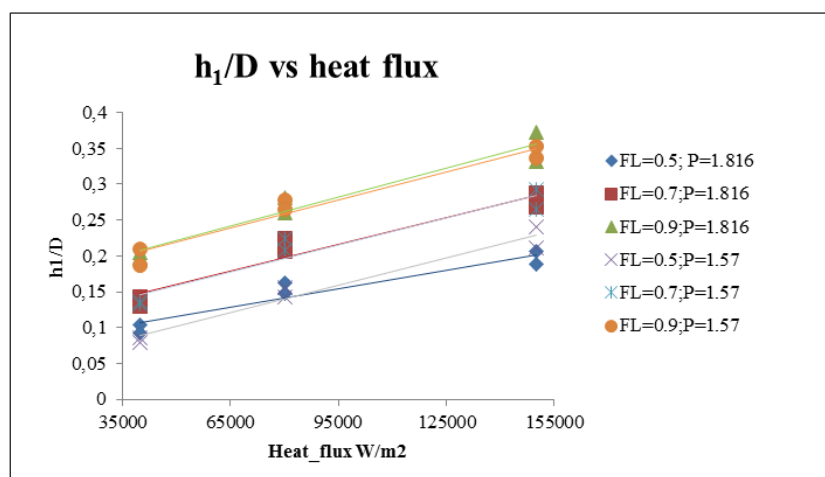


Figure 9.7: Trend of the parameter h_1/D as a function of the Flux Heat.

For this reason, a linear regression was performed obtaining a correlation in the following form:

$$\frac{h_1}{D} = a_0 + a_1 \cdot FL + a_2 \cdot \text{heat flux} + a_3 \cdot (P - P_{in}) \quad (105)$$

where heat flux is expressed in W/m^2 , pressure in Pa and Filling Level in volumetric fraction.

To perform the linear regression, MATLAB R2014 software was used. This calculation code provides the values of the coefficient a_i . In table 9.2 this constant values are reported:

<i>coefficient</i>	<i>value</i>
<i>a0</i>	-0.1042
<i>a1</i>	0.3027
<i>a2</i>	$1.2 \cdot 10^{-6}$
<i>a3</i>	$-8 \cdot 10^{-9}$

Table 9.2: Coefficient values obtained through the linear regression.

In figure 9.8, a comparison between the dimensionless parameter h_1/D obtained with the CFD Model and with the parametric correlation is reported.

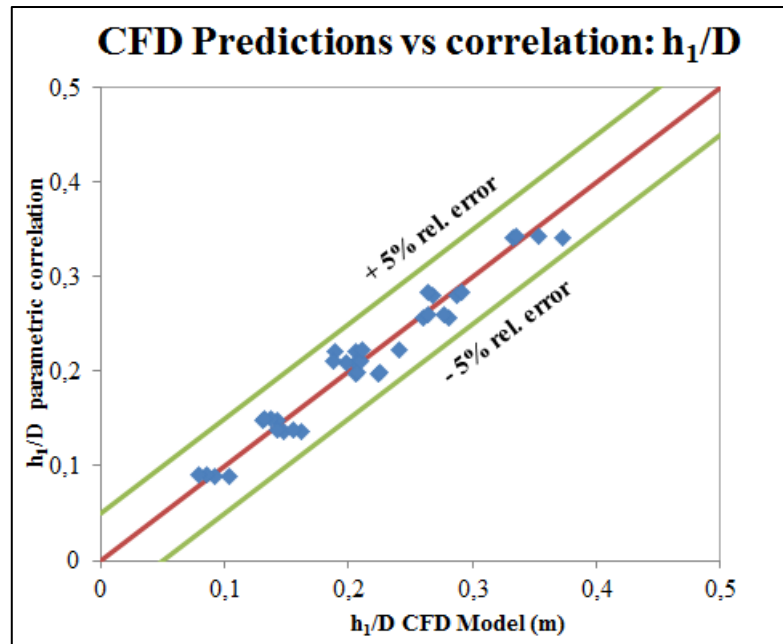


Figure 9.8: Comparison between the values of h_1/D predicted by the CFD Model and calculated with the parametric correlation.

9.2. Results and discussion of industrial accidents simulation

In this section, results of industrial accident obtained through the implementation of “advanced Fire Conditions” will be reported and discussed.

9.2.1 Results

Figure 9.9 shows the results obtained in the analysis of case-study “a”, where a high filling level (90%) was considered.

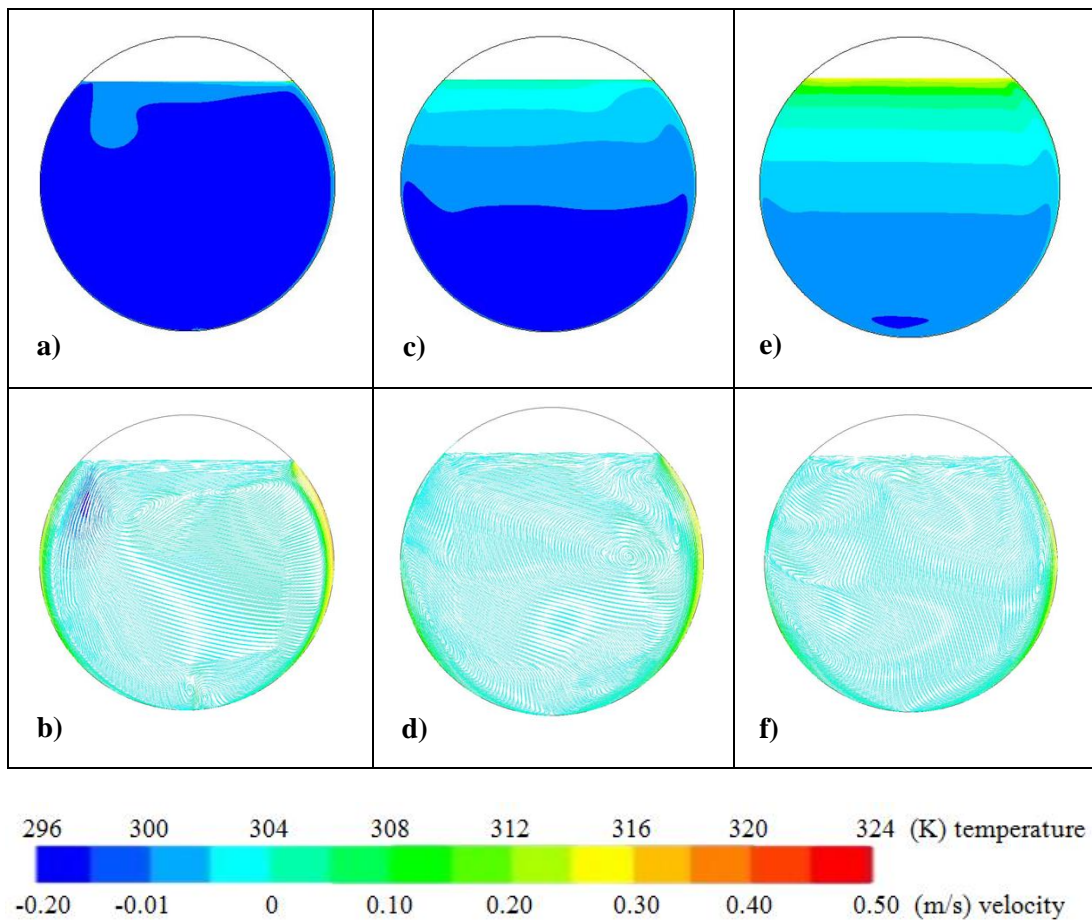


Figure 9.9: Results for case-study “a”: temperature profile (K) at 20 s (a), 100 s (c) and 200 s (e); axial velocity profile (m/s) at 20 s (b), 100 s (d) and 200 s (f). PRV opening time is 229.5 s.

Figure 9.9a shows the liquid temperature distribution at the beginning of the fire exposure. As expected, phenomena related to the natural convection are relevant only on the face of the shell exposed to flames. The liquid particles near the hot wall go up along it until liquid–vapour interface. Upon reaching the liquid surface, these particles spread towards the opposite face and fall back into the bulk. The particles liquid path is confirmed by the figure 9.9b, in which the axial

velocity profile is shown. At the beginning of the fire exposure is not present a altered thermally liquid layer, but the lading temperature is relatively homogeneous over all the liquid region. It ranges between 296 and 300 K while the ascent velocity is about of 0.5 m/s. The liquid thermal stratification begins to be evident after 100 s since fire start. Figure 9.9c shows the formation of a thin layer of about 4 cm near to the liquid–vapour interface. The convective motion and recirculation phenomena are also significant. The stratification is pronounced in the proximity of the reaching of the PRV set pressure (see figure 9.9e). the thickness if stratified layer is about 25 cm, while the liquid bulk temperature ranges between 298 and 305 K. the axial velocity begins to be less marked with respect the the initial time (see figure 9.9f). after 200 s the fluid is stable from the thermodynamic point of view: only after the PRV opening time (reached after 229.5 s) occurs the dissipation of the thermal stratification.

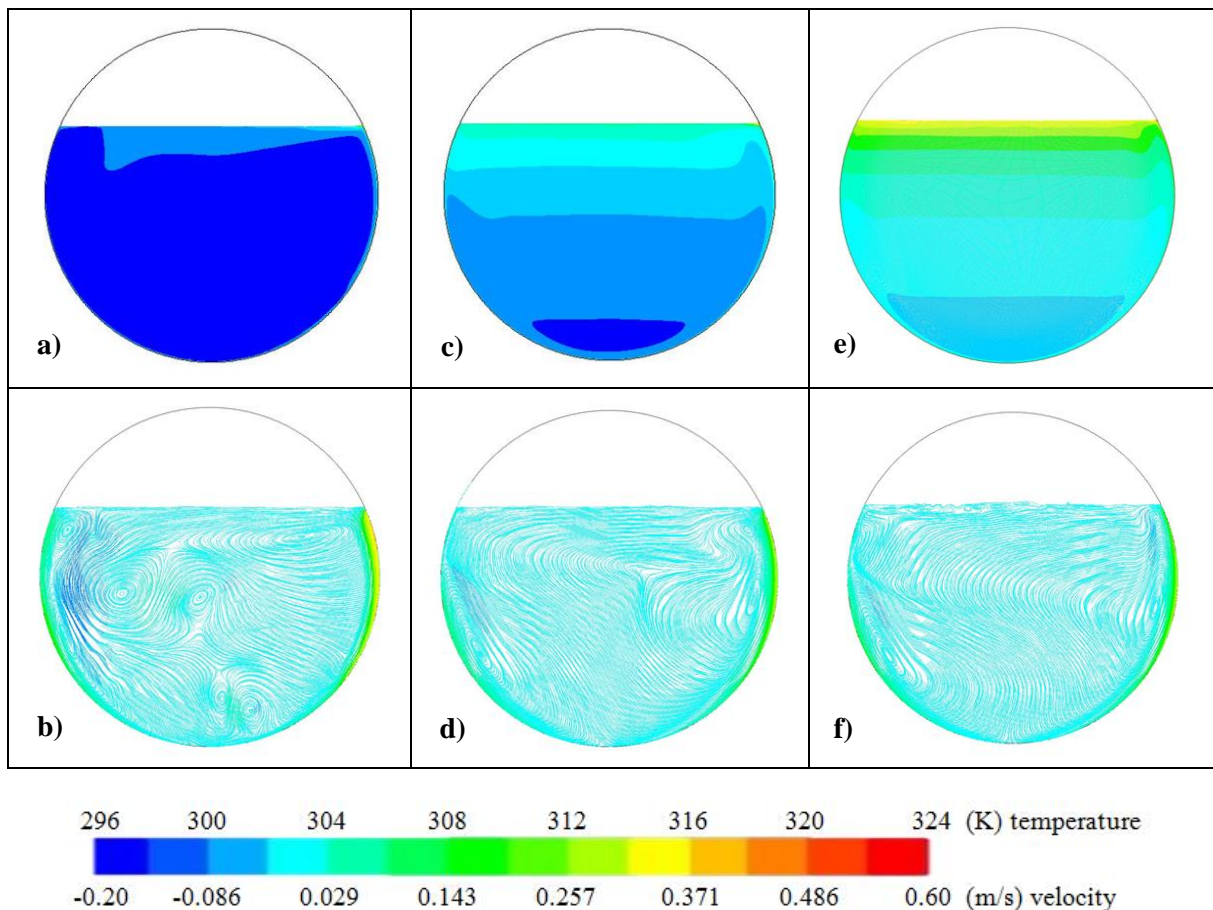


Figure 9.10: Results for case–study “b”: temperature profile (K) at 30 s (a), 150 s (c) and 300 s (e); axial velocity profile (m/s) at 30 s (b), 150 s (d) and 300 s (f). PRV opening time is 336.5 s.

Figure 9.10 shows the results obtained for case–study “b”, where a lower filling level are considered.

At the initial phase of the exposure, results are the same of the case–study “a”. the stratified layer is absent and the axial velocity are the same (ascent velocity is about of 0.5 m/s). liquid stratification is more pronounced after 150 s since fire exposure. Figure 9.10c shows the presence of a hot layer of about 15 cm. The layer temperature ranges between 305 and 310 K and the temperature gradient is about 60 K/m. The liquid bulk is cold (temperature ranging between 296 and 300 K) and an extremely lower temperature gradient is present with respect to the upper part of the tank (about 4 K/m). As shown in figure 9.10e, a more homogeneous temperature distribution is present all over the liquid phase (overall temperature gradient is ranging between 5 and 20 K/m). Then, the liquid stratification is less pronounced with respect to the case–study “a”. Moreover, in this case, due the lower filling level, the PRV opening time is reached after 336.5 s: more than 30% of the time required in case–study “a”.

9.2.2 Discussion

To assess the influence of filling level on the results, a comparison between case–studies was carried out. In particular, the dynamic liquid temperature profile (for three different spatial positions) and the internal pressure profile were analyzed.

Figure 9.11 shows this comparison respectively for case study “a” and case–study “b”.

As shown in Figure 9.11a, the dynamic pressure behaviour is characterized by a non regular growth, with significant change in the slope of the pressure curve. This is due to the stratification effect: for time higher than 150 s, the pressure gradient is more marked (curve leaning more), since the liquid thermal stratification, as established by the figure 9.9, is more pronounced. Moreover, the stratification layer, adjusting pressure in the vessel, significantly lowers the PRV opening time, which is reached after 229.5 s since fire exposure.

In case–study “b”, a gradual and slower vessels pressurization is obtained and then PRV opening time is much higher than in the other case (336.5 s). In fact, as shown in figure 9.10, the stratification is less prominent than in the case–study “a” and the temperature gradient is more homogeneous.

This is also confirmed by the temperature values in three different positions for time a little lower than PRV opening time. In case–study “b”, temperatures on the bottom vessel and in the liquid bulk are higher than temperatures obtained in the other case (of about 4 K), while in the proximity of the liquid–vapour interface, two values are almost equal.

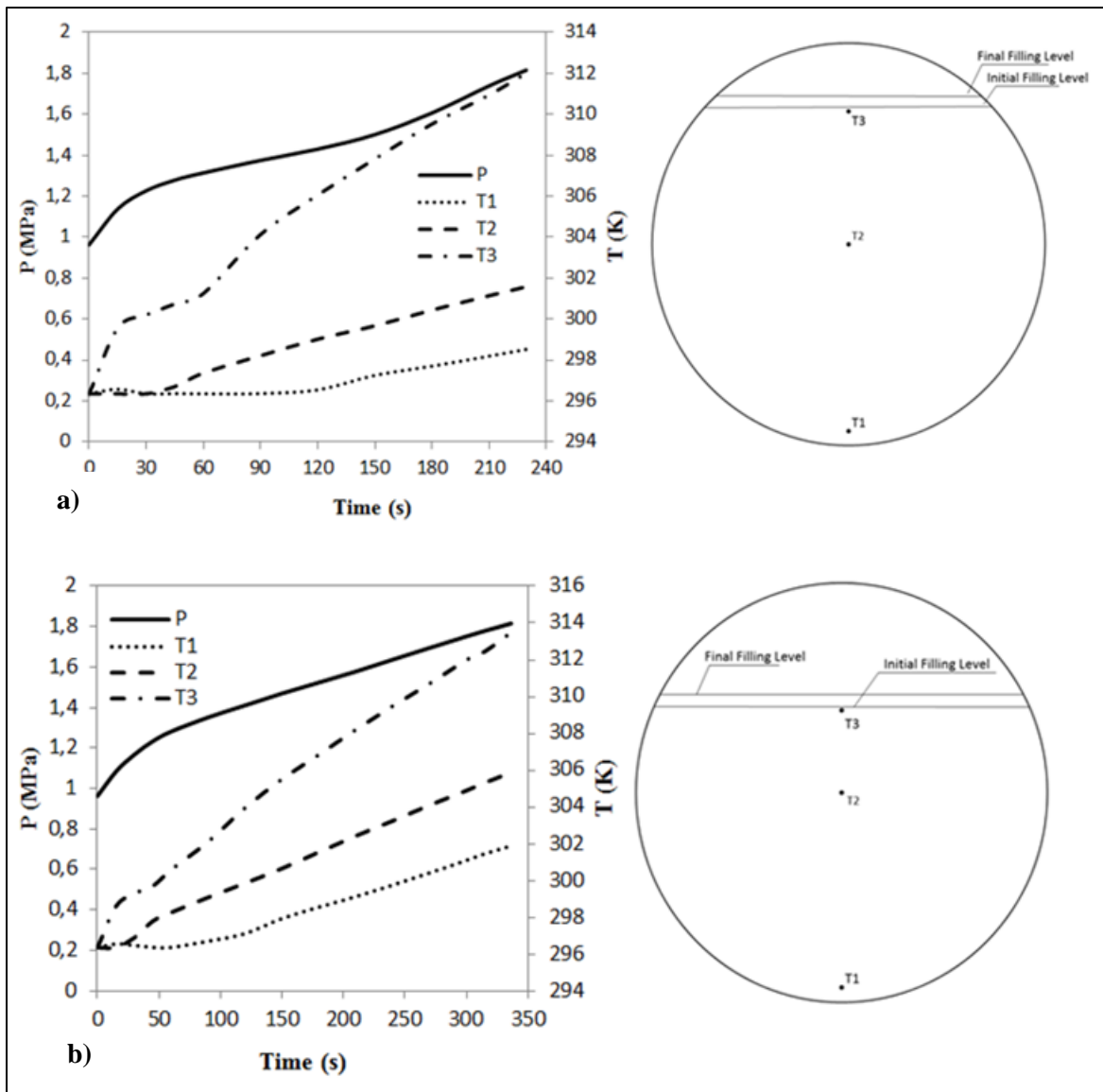


Figure 9.11: Pressure profile and liquid Temperature profile (1. near to bottom vessel, 2. in the liquid bulk, 3. near to liquid–vapour interface) for: a) case–study “a”; b) case–study “b”.

In addition, the transient effects that were found in the in the pressure build up in the vessel (see fig. 9.11) also affect the temperature rise in the liquid and, thus, the thermal expansion behaviour. As clearly shown in figure 9.12, thermal expansion is more pronounced in case–study “b”. The difference would have been more marked if the filling level of case–study “b” was considered less too.

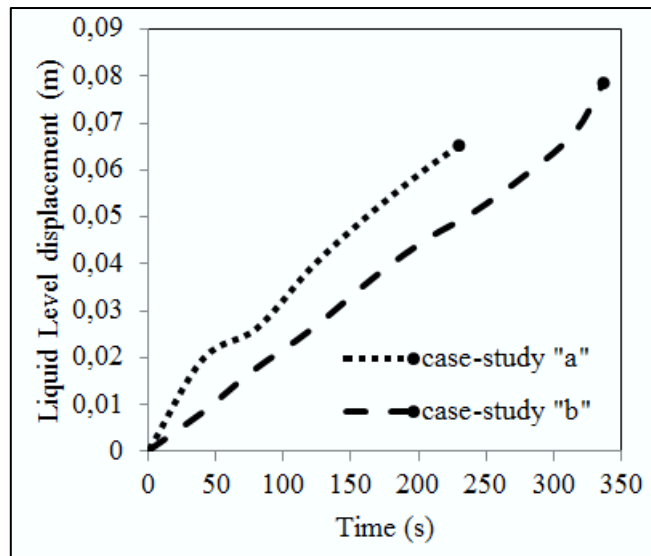


Figure 9.12: Comparison between the liquid thermal expansion predicted in case-studies, in terms of liquid level displacement (m).

Actually, top vapour space is reduced with respect to the initial value by 20% in case-study “a”, while in case-study “b” only by 11%.

The construction of fine and uniform mesh provides further advantages since the condensation/evaporation phenomena are considered overall domain. This mesh can be implemented for any liquid filling level without a thickening in the proximity of liquid-vapour interface. In addition, distortions cell are absent and then, considering the single cell, the calculation is lighter than to other types of meshes [42], without any convergence problem. However, the high number of cells leads to an higher computational time.

The interaction between integral models and distributed parameters models allows a more precise assessment of PRV opening time and then of time to failure of process and transport equipment. In other words, the use of advanced tools (CFD code) for the analysis of complex or critical escalation scenario may support the assessment of domino effect. To avoid the occurrence of domino scenarios, it is important an immediate intervention, since the available time is very low. The approach of study carried out in this part of work can provide useful indications for the installation of prevention and/or mitigation systems, in order to increase the time of a possible escalation accident and for the preparation of detailed emergency procedures.

10. Conclusions and further developments

Starting from a literature analysis about modeling the behaviour of pressurized vessels exposed to fires, a CFD model was improved with respect to a previous work [42]. The improvements are related to the numerical mesh and to the boundary conditions. After its validation, obtained through a comparison with results of a large-scale experimental test [22], CFD model was applied to two types of analysis:

- sensitivity analysis to assess the influence of liquid thermal stratification on the tank behaviour. Results obtained from this analysis can support the improvement of lumped parameters model, in order to consider stratification effects on the internal pressure rise of a vessel exposed to external fire. Moreover, the influence of all relevant parameter (size tank, filling level, heat flow, pressure) on the liquid thermal stratification was analyzed.
- Simulation of industrial accidental scenarios through the implementation of “advanced fire conditions” on the walls of the vessel. Results highlight the hazard related to “domino scenarios” that can take place in an industrial site. In particular, a tank containing LPG, although it not engulfed in a pool fire (but place at a certain distance), may represent a relevant hazard source, since the heating of the fluid may lead in a very serious scenario in a brief time.

Another important aspect is the improvement related to the numerical grid implemented for the simulation of industrial scenarios. Through the construction of a very fine and uniform mesh overall the domain, it is possible to predict very well the condensation/evaporation phenomena which may occur in the proximity of hot wall and/or to the liquid–vapour interface. In addition, this mesh can be used for any liquid filling level, due to the high quality and low skewness, without distortion cell problems.

In prospective, some simplification adopted for the development of the model may be dropped. In particular, the assumptions concerning a 2D domain, considering the vapour as a transparent medium in the calculation of the radiative heat transfer in the tip vapour space removed.

However, the main future developments can be summarized as follows:

- Assessment of the vessel behaviour after the opening of the PRV, in which complication mixing phenomena take place.
- Application of the parametric correlation, obtained by sensitivity analysis about liquid thermal stratification, to Lumped code.
- Extension of this approach for the simulation of accidents in industrial sites to other types of scenarios.
- Implementation of an insulating layer, so as to provide support to other tools (FEM, Lumped Models).

Reference

- [1] Lees F. (1996). *Loss Prevention in the process industries-Hazard Identification, Assessment and Control*. Oxford: Elsevier-Butterworth-Heinemann.
- [2] Landucci G., Tugnoli A., & Basini V. (2011, April). The Viareggio LPG accident: Lessons Learnt. *Journal of Loss Prevention in the Process Industries*, pp. 466-476.
- [3] Uijt de Haag P. & Ale B. (2005). *Guidelines for quantitative risk assessment "Purple Book"*.
- [4] Landucci G. & Tugnoli A. (2013). *Industrial Safety an Risk Assessment*.
- [5] Schuller J. (1997). *Methods for determining and processing probabilities "Red Book"*.
- [6] Landucci G., Cozzani V. & Birk A.M. (2013). *Domino Effects in the Process Industries*. Elsevier.
- [7] Paltrinieri N. & Landucci G. (2009). Risk reduction in road and rail LPG transportation by passive fire protection. *Journal of Hazardous Materials*, pp. 332-344.
- [8] CCPS (1999). *Guidelines for Consequence Analysis of Chemical Releases*. New York: American Institute of Chemical Engineers.
- [9] Abbasi T. & Abbasi S. (2006, September 27). The boiling liquid expanding vapour explosion (BLEVE): Mechanism, consequence assessment, management. *Journal of Hazardous Materials*, pp. 489-519.
- [10] Leslie M. & Birk A.M. (1991). State of the art of pressure liquefied gas container failure modes and associated projectile hazard. *Journal of Hazardous Materials*, pp. 329-265.
- [11] Reid T. (1980). Some theories on boiling liquid expanding vapour explosions. *Fire*, pp. 525-529.
- [12] McDevitt C.A. & Chan C. (1990). Initiation step of BLEVEs. *Journal of Hazardous Materials*, pp. 169-180.

- [13] Birk A.M. & Cunningham M. (1996). Liquid temperature stratification and its effect on BLEVEs and their hazards. *Journal of Hazardous Materials*, p. 219-237.
- [14] Birk A.M. et al. (1993). *Hot and Cold BLEVEs: Observation of two Different kinds of BLEVEs*. Atlanta: AIChE Symposium Series.
- [15] Salla J., Demichela M. & Casal J. (2006). BLEVE: A new approach to the superheat limit temperature. *Journal of Loss Prevention in the Process Industries*, pp. 690-700.
- [16] Sandler S. (1999). *Chemical and Engineering Thermodynamics*. Wiley and Sons.
- [17] Katz D. et al. (1971). LNG/Water explosions: Cause & Effect. *Hydrocarbon Process*, p. 50:240.
- [18] Prugh R. (1997). Quantitative evaluation of "BLEVE" hazards. *Journal of fire protection engineering*, pp. 9-24.
- [19] Venart J. (2000). *Boiling liquid expanding vapour explosions (BLEVE), possible failure mechanism and their consequences*. IChemE.
- [20] Raghavan V. (2006). *Material Science and Engineering*. Prentice Hall.
- [21] Keltner N. et al. (1990). Test unit effects on heat transfer in large fires. *Journal of Hazardous Materials*, pp. 33-47.
- [22] Townsend W. et al. (1974). *The effects of a fire environment on a rail tank car filled with LPG*. Washington: Department of Transportation U.S.A.
- [23] Birk A.M. (1989). Modeling the Effects of a Torch-type Fire Impingement on a Rail or Highway Tanker. *Fire Safety Journal*, pp. 277-296.
- [24] Roberts T. et al. (2004). *Design and Protection of Pressure Systems to Withstand Severe Fires*. IChemE.
- [25] Beattie J. et al. (1935). The critical constant of Propane. *The Journal of Chemical Physics*.
- [26] Shaluf I. (2007). An overview on BLEVE: Disaster Prevention and Management. *International Journal*, pp. 740-754.

- [27] Aydemir N. et al. (1988). Thermal Response Analysis of LPG tanks exposed to fire. *Journal of Hazardous Materials*, pp. 239-262.
- [28] Gong Y. et al. (2004, January 23). A simplified model to predict the thermal response of PLG and its influence on BLEVE. *Journal of Hazardous Materials*, pp. 21-26.
- [29] Lin W. et al. (2010, March 9). Experimental studies on the thermal stratification and its influence on BLEVEs. *Experimental Thermal and Fluid Science*, p. 972-978.
- [30] Yu C. et al. (1992). Transient Free Convection and Thermal Stratification in Uniformly-Heated Partially-Filled Horizontal Cylindrical and Spherical Vessels. *Journal of Thermal Science*.
- [31] Hadjisophocleous G. et al. (1990). A study of the effect of the tank diameter on the thermal stratification in LPG tanks subjected to fire engulfment. *Journal of Hazardous Materials*, pp. 19-31.
- [32] Gursu S. et al. (1993, September). Analysis and Optimization of Thermal Stratification and Self-Pressurization Effects in Liquid Hydrogen storage Systems. *Journal of Energy Resources Technology*.
- [33] Landucci G. et al. (2009). The Assessment of the damage probability of storage tanks in domino events triggered by fire. *Accident Analysis and Prevention*, pp. 1206-12015.
- [34] Graves K. et al. (1973). *Development of a computer model for modeling the heat effects on a tank car*. Washington DC: US Department of Transportation, Federal Railroad Administration.
- [35] Beynon G. et al. (1988). Fire engulfment of LPG tanks: HEATUP, a predictive model. *Journal of Hazardous Materials*, pp. 227-238.
- [36] Ramskill P. (1988). A description of the engulf computer codes - Codes to model the thermal response of an LPG tank either fully or partially engulfed by fire. *Journal of Hazardous Materials*, pp. 177-196.
- [37] Ramskill P. (1989). *ENGULF II - A computer code to model the thermal response of a tank partially or totally engulfed in fire*. Culcheth: Safety and Reliability Directorate.

- [38] Dancer D. et al. (1990). Pressure and temperature response of liquefied gases in containers and pressure vessels which are subjected to accidental heat input. *Journal of Hazardous Materials*, pp. 3-18.
- [39] Shebeko Y. et al. (1995). Some aspects of fire and explosion hazards of large LPF storage vessels. *Journal of Loss Prevention in the Process Industries*, pp. 163-168.
- [40] Salzano E. et al. (2003). Hazard of Pressurized Tanks Involved in Fires. *Industrial & Engineering Chemistry Research*, pp. 1804-1812.
- [41] Heymes F. et al. (2013). An experimental study of an LPG tank at low filling level heated by a remote wall fire. *Journal of Loss Prevention in the Process Industries*, pp. 1484-1491.
- [42] D'Aulisa A., Tugnoli A., Cozzani V., Landucci G. & Birk A. (2014). CFD Modeling of LPG vessels Under Fire Exposure Conditions. *AIChE Journal*, pp. 4292-4305.
- [43] Ferziger J., & Peric M. (2002). *Computational methods for fluid dynamics*. Berlino: Springer.
- [44] Ansys INC (2010). *ANSYS FLUENT Theory Guide v. 13.0*. Canonsburg (USA).
- [45] Hirt C. & Nichols B. (1981). Volume of fluid (VOF) method for the dynamics of free boundaries. *Journal of Computational Physics*, pp. 201-225.
- [46] Lee W. (1979). *A Pressure Iteration Scheme for two-phase Modeling*. New Mexico: Los Alamos Scientific Laboratory.
- [47] Knudsen M. (1934). *The Kinetic Theory of Gases: Some Modern Aspects*. London: Methuen & Co.
- [48] Smith J., Van Ness H. & Abbott M. (2005). *Introduction to Chemical Engineering Thermodynamics*. New York: McGraw-Hill.
- [49] Crowe C., Schwarzkopf J., Sommerfeld M. & Tsuji Y. (2012). *Multiphase Flows with Droplets and Particles*. Boca Raton: CRC Press.
- [50] Wu H., Peng X., Ye P. & Gong E. (2007). Simulation of refrigerant flow boiling in serpentine tubes. *Journal of Heat and Mass Transfer*, pp. 1186-1195.

- [51] Clift R., Grace J. & Weber M. (1978). *Bubbles Drops and Particles*. Academic Press.
- [52] Hiroharu K. et al. (1968, July 7). On the turbulent heat transfer by free convection from a vertical plate. *International Journal of Heat and Mass Transfer*, pp. 1117-1125.
- [53] Launder B. & Spalding D. (1972). *Lectures in Mathematical Models of Turbulence*. London: Academic Press.
- [54] Green D.W. & Perry R.H. (1997). *Perry's Chemical Engineers' Handbook 7th edition*. McGraw - Hill.
- [55] Green D.W. & Perry R.H. (2008). *Perry's Chemical Engineers' Handbook 8th edition*. McGraw - Hill.
- [56] Ansys INC (2014). *ANSYS FLUENT Theory guide v. 14.5*. Canonsburg (USA).
- [57] Reddy K. & Kumar N. (2008). Combined laminar natural convection and surface radiation heat transfer in a modified cavity receiver of solar parabolic dish. *International Journal of Thermal Science*, pp. 1647-1657.
- [58] Versteeg H. & Malalasekera W. (2007). *An Introduction to Computational Fluid Dynamics: The Finite Volume Method*. PEARSON Education.
- [59] Administration: National Archives and Records (2013). *Code of Federal Regulations Title 49, Transportation*. Los Angeles: Claitor's Publishing Division.
- [60] Bazzocchi M., Landucci G. & Cozzani V. (2014). *Evaluation of the pressure build up in pressurized tankers exposed to fire*. Bologna.
- [61] Birk A.M. et al. (2013). Analysis of a Propane Sphere BLEVE. *AIDIC*, pp. 481-486.
- [62] Technology AEA. (2003). *Major Hazards Assessment Unit*. MHIDAS. London, UK: Health and Safety Executive.
- [63] CECAR (1982). *Risk Analysis of six potentially industries objects in the Rijnmond Area, a pilot study*. Dordrecht (NL).

- [64] Egidi D., Foraboschi F., Spadoni G., & Amendola A. (1995). The ARIPAT project: analysis of the major accident connected with industrial and transportation activities in the Ravenna area. *Reliability Engineering and Systems Safety*, pp. 75-89.
- [65] HSE. (1982). *Canvey: summary of an investigation of a potential hazards from operations in the Canvey Island*. London: Health and Safety Executive - HM Stationary Office.
- [66] Droste B. et al. (1999). Impact of an exploding LPG rail tank car onto a castor spent fuel cask. *Nuclear Technology Publishing*, pp. 231-240.
- [67] Google Maps. Retrieved 2015 September 23, from <https://www.google.it/maps>
- [68] Landucci G. et al. (2014, August 1). Release of hazardous substances in flood events: Damage model for horizontal cylindrical vessels. *Reliability Engineering and System Safety*, pp. 125-145.
- [69] Raj P. (2005, May 23). Exposure of a liquefied gas container to an external fire. *Journal of Hazardous Material*, pp. 37-49.

Appendix

Appendix 1: Subroutine for Evaporation -Condensation Phenomena

```
#include "udf.h"
#include "sg_mphase.h"

DEFINE_SOURCE(liq_src, cell, sec_th, dS, eqn)
{
  Thread *mix_th, *pri_th;
  real m_dot_l;
  real press;
  real T_SAT;
  mix_th = THREAD_SUPER_THREAD(sec_th);
  pri_th = THREAD_SUB_THREAD(mix_th, 0);
  press=C_P(cell,mix_th)+963000;
  T_SAT=(-6e-12)*press*press+(5e-05)*press+253.76;

  if(C_T(cell, mix_th)>=T_SAT)
  {
    m_dot_l = -0.1*C_VOF(cell, sec_th)*C_R(cell, sec_th)*fabs(C_T(cell, mix_th) -
      T_SAT)/T_SAT;
    dS[eqn] = -0.1*C_R(cell, sec_th)*fabs(C_T(cell, mix_th) - T_SAT)/T_SAT;
  }
  else
  {
    m_dot_l = 0.1*C_VOF(cell, pri_th)*C_R(cell, pri_th)* fabs(T_SAT-
      C_T(cell,mix_th))/T_SAT;
    dS[eqn] = 0.;
  }
  return m_dot_l;
}

DEFINE_SOURCE(vap_src, cell, pri_th, dS, eqn)
```

```
{
  Thread * mix_th, *sec_th;
  real m_dot_v;
  real press;
  real T_SAT;
  mix_th = THREAD_SUPER_THREAD(pri_th);
  sec_th = THREAD_SUB_THREAD(mix_th, 1);
  press=C_P(cell,mix_th)+963000;
  T_SAT=(-6e-12)*press*press+(5e-05)*press+253.76;

  if(C_T(cell, mix_th)>=T_SAT)
  {
    m_dot_v = 0.1*C_VOF(cell, sec_th)*C_R(cell, sec_th)*fabs(C_T(cell, mix_th) -
      T_SAT)/T_SAT;
    dS[eqn] = 0.;
  }
  {
  else
  {
    m_dot_v = -0.1*C_VOF(cell, pri_th)*C_R(cell, pri_th)*fabs(T_SAT-
      C_T(cell,mix_th))/T_SAT;
    dS[eqn] = -0.1*C_R(cell, pri_th)* fabs(C_T(cell, mix_th) - T_SAT)/T_SAT;
  }
  return m_dot_v;
}
```

```
DEFINE_SOURCE(enrg_src, cell, mix_th, dS, eqn)
```

```
{
  Thread *pri_th, *sec_th;
  real m_dot;
  real press;
  real T_SAT;
  real LAT_HT;
  pri_th = THREAD_SUB_THREAD(mix_th, 0);
  sec_th = THREAD_SUB_THREAD(mix_th, 1);
  press=C_P(cell,mix_th)+963000;
```

```
T_SAT=(-6e-12)*press*press+(5e-05)*press+253.76;
LAT_HT=-0.0682*press+403262;

if(C_T(cell, mix_th)>=T_SAT)
{
  m_dot = -0.1*C_VOF(cell, sec_th)*C_R(cell, sec_th)*fabs(C_T(cell, mix_th) -
  T_SAT)/T_SAT;
  dS[eqn] = -0.1*C_VOF(cell, sec_th)*C_R(cell, sec_th)/T_SAT;
}
else
{
  m_dot = 0.1*C_VOF(cell, pri_th)*C_R(cell, pri_th)*fabs(T_SAT-
  C_T(cell,mix_th))/T_SAT;
  dS[eqn] = 0.1*C_VOF(cell, pri_th)*C_R(cell, pri_th)/T_SAT;
}
return LAT_HT*m_dot;
}
```

Appendix 2: subroutine for Boundary Conditions in the Validation Case

```
DEFINE_PROFILE(flux_time, thread, position)
{
  face_t f;
  real t = CURRENT_TIME;
  begin_f_loop(f, thread)
  {
    if (t < 25.)
    { F_PROFILE(f, thread, position) = 5250; }
    else if (t >= 25 && t < 50.)
    { F_PROFILE(f, thread, position) = 2100 * t - 47250; }
    else if (t >= 50 && t < 60.)
    { F_PROFILE(f, thread, position) = 105 * t + 52500; }
    else if (t >= 60 && t < 75.)
    { F_PROFILE(f, thread, position) = 70 * t + 54600; }
    else if (t >= 75 && t < 85.)
    { F_PROFILE(f, thread, position) = -735 * t + 114975; }
    else if (t >= 85 && t < 90.)
```

```
    { F_PROFILE(f, thread, position) = 1470 * t - 72450; }
    else if (t >= 90 && t < 105.)
    { F_PROFILE(f, thread, position) = 59850; }
    else if (t >= 105 && t < 120.)
    { F_PROFILE(f, thread, position) = 630 * t - 6300; }
    else if (t >= 120 && t < 125.)
    { F_PROFILE(f, thread, position) = -1680 * t + 270900; }
    else
    {      F_PROFILE(f, thread, position) = 60900; }
  }
end_f_loop(f,thread)
}
```

Appendix 3: subroutine for “Advanced Boundary Conditions”

```
DEFINE_PROFILE(flux_heat_space, thread, position)
{
  face_t f;
  real x[ND_ND];
  real y;
  real a;
  begin_f_loop(f, thread)
  {
    F_CENTROID(x, f, thread);
    y = x[1];
    a = 1.6;
    if (x[0] <= -0.866*a && y <= 0.)
    {F_PROFILE(f, thread, position) = 0.;}
    else if (x[0] <= -0.866*a && y > 0.)
    {F_PROFILE(f, thread, position) = 4625*y;}
    else if (x[0] <= -0.7071*a && x[0] > -0.866*a && y <= 0.)
    {F_PROFILE(f, thread, position) = 0.;}
    else if (x[0] <= -0.7071*a && x[0] > -0.866*a && y > 0.)
    {F_PROFILE(f, thread, position) = 21125.06*y - 13200.05;}
    else if (x[0] <= -0.5*a && x[0] > -0.7071*a && y <= 0.)
    {F_PROFILE(f, thread, position) = 0.;}
  }
}
```



```
else if (x[0] <= -0.5*a && x[0] > -0.7071*a && y > 0.)
{F_PROFILE(f, thread, position) = 40512.9*y - 35134.67;
else if (x[0] <= 0.*a && x[0] > -0.5*a && y <= 0.)
{F_PROFILE(f, thread, position) = 0.;}
else if (x[0] <= 0.*a && x[0] > -0.5*a && y > 0.)
{F_PROFILE(f, thread, position) = 128731.34*y - 157370.15;}
else if (x[0] <= 0.5*a && x[0] > 0.*a && y <= 0.)
{F_PROFILE(f, thread, position) = 34514.92*y + 55223.88;}
else if (x[0] <= 0.5*a && x[0] > 0.*a && y > 0.)
{F_PROFILE(f, thread, position) = -110541.04*y + 225465.67;}
else if (x[0] <= 0.7071*a && x[0] > 0.5*a && y <= 0.)
{F_PROFILE(f, thread, position) = 36186.28*y + 57539.71;}
else if (x[0] <= 0.7071*a && x[0] > 0.5*a && y > 0.)
{F_PROFILE(f, thread, position) = -18093.14*y + 97369.85;}
else if (x[0] <= 0.866*a && x[0] > 0.7071*a && y <= 0.)
{F_PROFILE(f, thread, position) = 36576.53*y + 57981.22;}
else if (x[0] <= 0.866*a && x[0] > 0.7071*a && y > 0.)
{F_PROFILE(f, thread, position) = 3017.87*y + 73485.71;}
else if (x[0] > 0.866*a && y <= 0.)
{F_PROFILE(f, thread, position) = 36475*y + 57900;}
else
{F_PROFILE(f, thread, position) = 22500*y + 57900;}
}
end_f_loop(f,thread)
}
```

List of symbols

Symbols	Description
a	Droplet volumetric interfacial area
a_{PR}	First peng-robinson equation coefficient
A	surface
b_{PR}	Second Peng-Robinson equation coefficient
$C_{1\varepsilon}, C_{2\varepsilon}, C_{\mu}$	Constant of K- ε Model
c_p	Specific heat at constant pressure
D	diameter
D_{SM}	Mean Sauter Diameter
E	Fluid energy per unit mass
E	Young Module
\vec{E}	Emissive power vector
Eo	Eotvos Number
F	External force
F_{jk}	View factor between surface j and k
g	Gravitational acceleration
G_b	Generation of turbulent kinetic energy due to buoyancy
G_K	Generation of turbulent kinetic energy due to mean velocity gradient
Gr	Groshof number
h_f	Flame lenght
\hat{H}	Fluid enthalpy per unit mass
H_C	Heat of combustion
H_F	Flame height
H_V	Heat of vaporization
\vec{I}	Identity matrix
J	Evaporation/condensation mass flux
J_K	Radiosity of the k surface
k	Thermal conductivity
K	Turbulent kinetic energy
l_0	Original length of the steel frame
l	Final length of the steel frame
m''	Pool burning rate
M_w	Molecular weight
\dot{m}	Mass source term dur to evaporation/condensation phenomena
P	pressure
P_r	Prandtl number
q	Heat flux
Q	heat
r	reflectivity
R	Universal gas constant

r_{jk}	Distance between j and k surface
Ra	Rayleigh number
S	Energy source term
S_{aL}	Liquid volume fraction source term
T	temperature
$T_{L,av}$	Average liquid temperature
\mathbf{u}	Velocity vector
$\bar{\mathbf{u}}$	Time averaged two-phase velocity
$\tilde{\mathbf{u}}$	Time fluctuating two-phase velocity
u_w	Wind velocity
\mathbf{u}_w^*	Scaled wind velocity
V	Cell volume
v_m	Molar volume
W	Energy released during BLEVE
X	Mass source term generic expression
Y_M	Generation of turbulen kinetic energy due to compressibility effects
Y^+	Dimensionless length for turbulence model

List of Greek Symbols

Greek Symbols	Description
α_{bs}	absorbivity
α_i	Phase volumetric fraction
β	Thermal expansion coefficient
β_c, β_E	Accommodation coefficient for condensation/evaporation
β'	Mass transfer time relaxation parameter
γ	Specific heat ratio
δ_S (or h_1)	Stratification layer thickness
δ_{jk}	Visibility between the surface j and k
$\tilde{\epsilon}$	strain
ϵ	Turbulent kinetic energy dissipation
λ	Latent heat
μ	Dynamic viscosity
Π	Dynamic stratification index
ρ	density
σ	Stefan-Boltzmann constant
σ	Surface tension
$\bar{\sigma}$	stress
σ_{adm}	Admissible stress
σ_{eq}	Equivalent stress
σ_Y	Yield stress
$\sigma_K, \sigma_\epsilon$	Standard K- ϵ turbulence model constant
τ_w	Shear viscous stress
Ψ	Peng-Robinson equation parameter
ω	Acentric factor

List of acronyms

ACRONYMS	Description
BLEVE	Boiling liquid expanding vapour explosion
CFD	Computational fluid dynamics
CP	Critical point
CV	Control volume
FF	Flash fire
HazOp	HAZard and OPerability analysis
LPG	Liquefied petroleum gas
PFP	Passive fire protection
PRV	Pressure relief valve
QRA	Quantitative risk assessment
SEP	Surface emission power
SLT	Superheat limit temperature
S2S	Surface to surface radiation model
TFA	Tree fault analysis
TLOC	Total loss of containment
te	Time to empty
tff	Time to failure
UDF	User defined function
VOF	Volume of fluid model
VCE	Vapour cloud explosion

List of subscript and superscript

Subscript	Description
atm	Atmospheric
BULK	Vessel lading
c	Critical
C	condensation
CL	Condensation effect on liquid phase
CV	Condensation effect on vapour phase
E	Evaporation
eff	Effective: sum of molecular property and turbulent property
f	flame
L	Liquid
SL	Superheat limit
t	Turbulence quantity
T	tank
V	Vapour
WALL	Vessel wall
0	Reference condition

Superscript	Description
T	transposed
0	Saturation condition

Acknowledgements

First of all, I would like to express my gratitude to my supervisor Eng. Gabriele Landucci: this work would not have been possible without his help, guidance and support.

Furthermore I would like to thank to the Eng. Chiara Galletti for the attention paid to my work.

This thesis is the conclusion of my formation which has started about 20 years ago. A particular thought goes to my grandparents: i know that they would have been proud about me.

I am very grateful to all my family: my parents Tonino and Gabriella, my brother Alessandro and my sister Francesca for the support they have given me from every points of view and to be always the first to believe in me. They have transmitted to me peace of mind without which I would not have reached this goal.

I would like to thank especially my girlfriend Marta. In the last years we have shared everything and this is just the beginning for us. I am conscious of the fact that I have been through a difficult period which has not always made the things easier to Marta. Anyway she has always been patient with me and I have always felt her support, help and love.

I would like to thank Tatiana for the support and encouragements in last part of my university path.

Finally, I would also thank my friends Gabriele, Lorenzo and Erica for their proximity in the more hard periods.